

UNIVERSITY OF BIRMINGHAM



Department of Metallurgy & Materials

Irradiation Damage Simulations of Platinum Group Metal Modified Austenitic Stainless Steels for Reactor Core Components

by Ben Palmer

A thesis submitted to the University of Birmingham for the degree of Doctor of Philosophy
Supervised by Dr Brian J Connolly, Dr Mark S D Read and Prof Alessandro Mottura

Abstract

Austenitic stainless steels have been used since the early days of nuclear power and they will play an important role in the construction of Generation III+ (Gen III+) and Generation IV (Gen IV) plant designs. Irradiation of components by neutrons is expensive with relatively few high flux reactors available. The experiments to represent 30-40 years within a reactor core are time consuming and produce radioactive waste as a by-product. Two alternatives to testing by irradiating with a neutron source are either irradiating with a proton beam or by modelling damage events with a computer.

The efficiency and computational power of computers continues to improve. First principles Density Functional Theory (DFT) and molecular dynamics (MD) are computational methods that are now able to give insights into why materials behave the way they do.

1. Proton sources are more widespread, they are relatively cheap and may be focused into a much smaller beam to concentrate the amount of damage per time unit. The radioactive waste may be significant but by carefully selecting the ion energy the electromagnetic repulsion between ions and nuclei reduces transmutation of target atoms whilst maintaining the amount and depth of damage into the material required for testing purposes.

A modified Bateman equation is derived to calculate the radioactivity of a proton irradiated target and a computer program (Activity) is created to implement the calculation using evaluated nuclear reaction cross section data. The program is compared to data measured from the irradiation of an iron sample using the University of Birmingham cyclotron. It is also used to model the radioactivity of a target irradiated to 100 displacements per atom (DPA) at a range of beam energies in order to minimise both the irradiation time and radioactive waste. The results show an increase in target activity of 3 orders of magnitude for a 25MeV proton beam when compared to a 10MeV proton beam.

2. Sensitisation of austenitic steels, by processes such as welding, depletes Cr from grain boundaries removing the corrosion resistant Cr_2O_3 passive layer. Previous (experimental) work has shown that these steels, when doped with Pd or Ru, retain corrosion resistance at the grain boundary[scrstainless]. This work takes a step towards investigating whether or not these platinum group metal (PGM)s deplete or saturate at the grain boundary while under irradiation and this may be studied with MD simulations. A computer program is developed to fit interatomic potentials to experimental data and DFT generated data. The properties of face centered cubic (FCC) Fe are computed using DFT. These data along with other properties and DFT generated data are used to derive interatomic potentials (with a dominant ZBL pair for close range collision interactions) for Fe-Pd. These potentials are a step towards MD simulations of the irradiated grain boundaries.

Contents

List of Figures

List of Tables

Chapter 1

Introduction

Several Gen III+ nuclear reactors have been proposed for construction in the UK (with Hinckley Point C now under construction) and Gen IV nuclear reactors are being researched and developed. New materials are required to withstand the extreme conditions in and around the core of these reactors. Austenitic stainless steels have been an important structural material in the industry, and may continue to be so, providing the problem of inter granular stress corrosion cracking (IGSCC) can be addressed. Doping these steels with platinum group metal (PGM)s has been seen to reduce IGSCC, but the effects on corrosion resistance are unknown for these steels when irradiated by a radiation field.

1.1 Motivation

I have often questioned the motivation behind this work, and at times it has been a challenge to see the wood through the trees. To help me focus throughout I would restate the motivation and objectives to myself.

Mass produced steels are not perfect repeating crystals, but are made up of small grains. Cr is added to steel to make stainless steel, and this is more resistant to corroding than steel. When steel is in a nuclear reactor, it will have to perform under extreme conditions, such as:

- high temperatures
- strain cause by high pressures and radiation induced swelling
- radiation damage and strains resulting from this damage
- a changing environment, for example radiolysis of water and transmutation of isotope due to radiation
- corrosive environments while in the reactor
- corrosive environments out of the reactor (e.g. fuel cladding in storage)

Radiation damages the steel in a number of ways, including directly knocking atoms out of their place within the lattice structure of the crystalline grains that make up the steel as well as changing the isotopes that make up the steel into new isotopes. An example of the latter is a neutron reacting with an Fe atom, transmuting it into a Co atom.

In time, the radiation damage causes the percentage of Cr at the surface of the grains to drop, and as it falls the steel loses its protection from corrosion at the boundary between the grains it is made of.

This work is divided into two parts.

1.1.1 Part 1: Activity Computer Program

The materials must be tested before being used in a nuclear reactor. One way to do this would be to place samples of the steel into a test reactor. This is expensive and, as a by-product, the steel sample becomes radioactive. It is difficult to create a large number of neutrons, but it is much easier, and cheaper, to create a beam of protons. Protons can be accelerated in a machine such as the Cyclotron at the University of Birmingham.

The damage that protons cause to a sample is not precisely the same as that caused by neutrons, but it is a cheaper alternative and is a trade-off between the cost and results. One side effect that proton irradiation shares with neutron irradiation is the creation of radioactive waste.

The first part of this work investigates exactly how radioactive a sample becomes when irradiated with a proton beam. An existing set of equations, named after Mathematician Harry Bateman, were modified, and a computer program was created to perform the calculation. The user inputs the constituent elements that make up the material, the ratio of these elements, and the irradiation settings. The program then estimates how radioactive the sample will be and the predicted gamma energies.

1.1.2 Part 2: Palladium-Iron Potential

Adding Cr to make stainless steel is not the only way to make a steel resistant to corrosion. Adding metals such as Mo and Pd to steel can increase the resistance to corrosion, but Mo is several hundred times the cost of Fe ore, and Pd is thousands of times as expensive.

Simulating radiation damage using a computer is now a feasible and sensible way to investigate how these materials will be affected by radiation damage, and the simulations may reveal insights that experiments are not able to show, either because they happen on too small a timescale or within the material at too small a length scale.

Key to the simulations success is being able to accurately calculate how the atoms interact with one another. The second part of this work concentrates on deriving a mathematical description of how Pd and Fe atoms interact with one another, which would then allow future simulations of steel with small amounts of Pd added to it.

Radiation causes Cr to be depleted at the grain boundary. If these simulations show that Pd is not depleted, it would suggest that the corrosion resistance is maintained, despite the decrease in the amount of Cr at the grain boundary due to radiation damage.

1.2 Nuclear Power in the UK

1.2.1 Nuclear Fuel

The primary fuel of commercial nuclear power stations since those first built in the 1950s has been U. U-235 is fissile and fissions with a high probability when thermal neutrons are captured, due to its very high thermal neutron fission cross section (fig. ??).

Natural U contains a small percentage of fissile U-235 (0.7%) with the rest being its heavier isotope, U-238. U-238 is fissionable, but its fission cross section is much lower than U-235 (fig. ??). Many of the design considerations for reactors in operation revolve around the amount of U-235 there is in the fuel and having a sufficient flux of thermal neutrons passing through the fuel to sustain a reaction.

A number of Gen IV designs use the fast neutron spectrum to fission U-238 and other fuels such as Th-232 to generate energy and breed other fissile isotopes. By moving away from U-235, this increases the potential fuel stockpile, but also brings its own set of challenges.

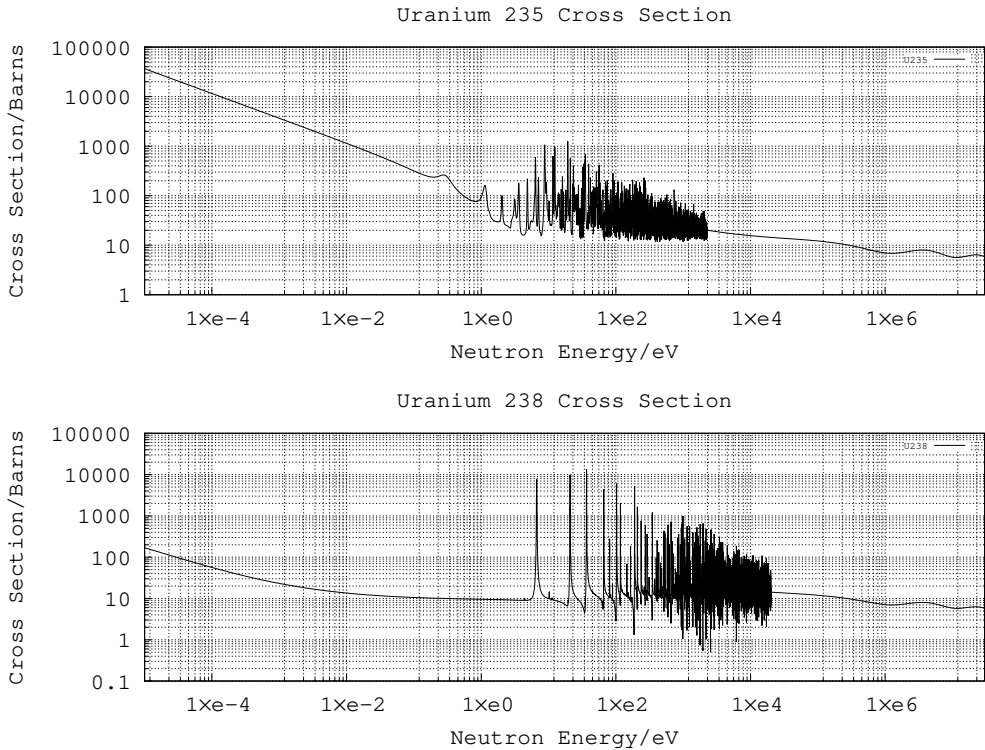


Figure 1.1: U-235 and U-238 Fission Cross Sections

1.2.2 Generation I Reactors

The first generation reactors were primarily prototype reactors. They included graphite moderated reactors, light water and heavy water reactors. Early reactors were designed to produce electricity, but also fissile material for nuclear weapons. With a power output of less than 2MW, the Gen I power station Calder Hall generated much less electricity than a modern nuclear power plant which may produce 1GW per reactor. It did, however, produce Pu for the UK's nuclear weapon programme.

Magnox type reactors were the first used in the United Kingdom. These reactors used natural U as a fuel and were carefully designed to produce energy despite using an un-enriched fuel. Graphite was used as a moderator, and the low neutron capture cross section of the Magnox Mn alloy cladding allowed a nuclear reaction to occur despite the fuel not being enriched.

In all there were 11 Magnox power stations built in the UK with 26 reactors in total. Construction of the first commercial reactor in the UK, Calder Hall, started in 1953 and it operated from 1956 to 2003. All have now shut down with the last, Wylfa in Anglesey, closing in 2015.

1.2.3 Generation II Reactors

Gen II marked the transition from prototype reactors to higher powered commercial reactors. There were a number of designs including the AGR, a graphite core CO_2 cooled reactor, that was implemented in the UK. Light water reactors included the PWR and BWR in the west and the VVER in the USSR. The RBMK was a graphite moderated reactor used in the USSR and the CANDU a heavy water reactor designed and used in Canada.

There are many of these reactors from this period still in operation around the world, and there have been recent implementations of these designs. There are 15 reactors currently operating in the UK, and they are all Gen II reactors. Of these, 14 are AGR and 1, Sizewell B, is a PWR (fig. ??).

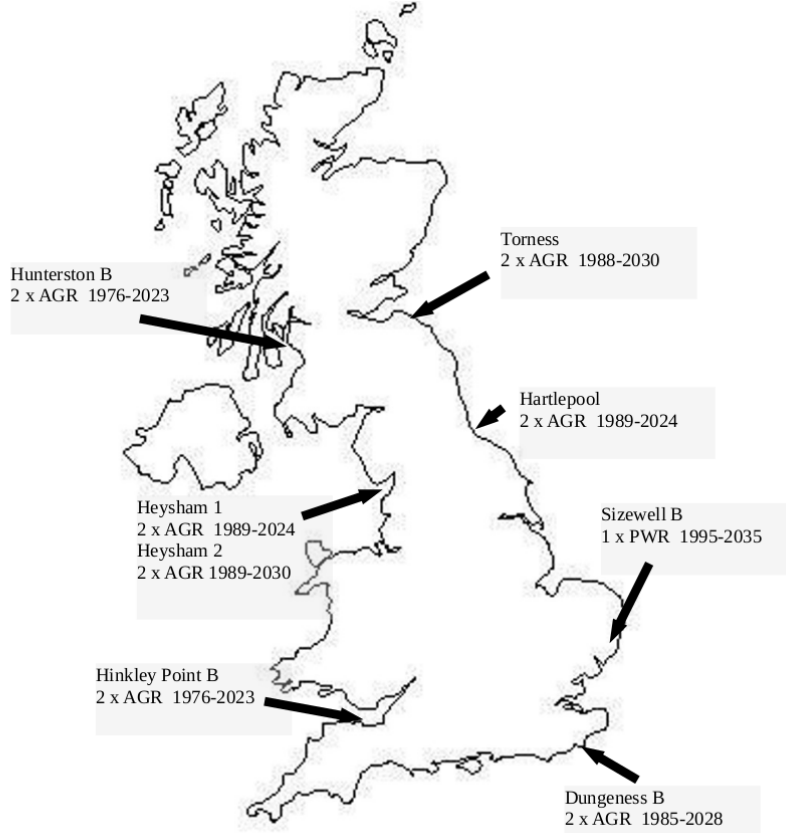


Figure 1.2: Remaining reactor locations in the UK

The planned life span for this generation of reactor was 30-40 years, although this has now been extended to 50-60 years in some cases. The AGR reactors in the UK have been operational for over 40 years, and by the time Hunterston B and Hinkley Point B are planned to be decommissioned, they will have been operational for 46 years. Designed with safety improvements in mind over Gen I reactors, they were also intended to produce more power with less of a focus on producing fissile material for weapons. Unfortunately, this generation of reactors had the worst track record of any with safety, with Three Mile Island, Fukushima and Chernobyl all being Gen II designs.

Gen II+ reactors have been built recently with 18 CPR-1000s being constructed over the last decade in China. The UK is currently looking towards Gen III+ reactors while Gen IV proposals are being researched.

1.2.4 Generation III Reactors

There are no Gen III reactors operating in the UK. The first was built in Japan in 1996 and the type of reactor installed was an Advanced Boiling Water Reactor (ABWR). Bradwell B is a proposed site for the Gen III Hualong One type PWR power plant (HPR1000), and if this goes ahead it would have an expected opening date between 2030-2035.

This generation of reactor was designed to exceed the service life of the previous generation, and generate power for at least 60 years. The safety features have been improved and include increased resilience to external factors, including accidental or intentional aircraft collision into the plant [[genIIIimprovements](#)].

Gen III+ reactors go further in adding passive safety features, such as natural circulation and gravity coolant feed [[geniiiplussafety](#)]. Other aims of future generations are to standardise and simplify designs whilst improve the economy over Gen II+ and Gen III.

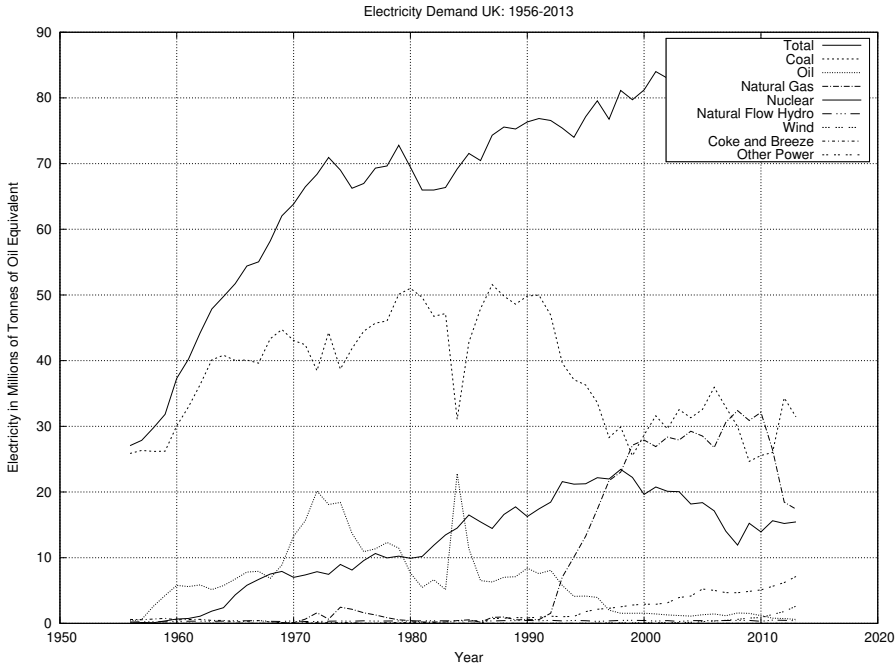


Figure 1.3: Electricity in Millions of Tonnes of Oil Equivalent

1.3 An Approaching Energy Gap for the UK

Since Calder Hall, the first commercial nuclear power plant, opened in 1956, the demand on electrical power generation in the UK has tripled (fig ??). There is now a reliance on cheap and clean power from nuclear reactors as these provide a quarter of our electricity. There are sixteen reactors operational in the UK: the Magnox reactor at Wylfa and the fourteen AGR reactors are due to be decommissioned by 2023[gen4], and the remaining PWR reactor, Sizewell B, is expected to remain operational until 2035[gen4].

There is an obvious concern that within the next ten years the UK will lose a sizeable proportion of its electricity generation capabilities. There are increasing pressures on countries to reduce their carbon dioxide output, so the gap created by ageing nuclear plants and coal power needs to be filled.

1.3.1 Why choose Nuclear Power?

As a civilization we need energy, whether it's in the form of electricity or stored chemically, and whilst we are becoming more efficient at using that energy, the demand for it will remain (unless something drastically changes our society). There is a choice between burning fossil fuels or bio fuels, using energy from the Sun, wind, ground, oceans or rivers and finally using the energy of the nucleus, whether by fission or fusion.

Each has its drawbacks and advantages. Renewable energies are unreliable; wind power only provides energy when there is a wind, and if the wind is too strong, they must be shut down or risk damage. The Sun is only available for a portion of the day, and the duration and intensity change with the seasons, not to mention the impact of clouds on solar power. Renewable sources are not very good at responding to demand; there isn't a button to turn up the power of the Sun, or increase the velocity of the wind when the national grid demands it. If we were completely reliant on renewable energies, there would either need to be an efficient way to store energy on a large scale, or many more solar, wind, tidal and hydroelectric power stations than would be needed to produce excess energy. Whilst the energy source may be free, turbines, solar panels, dams and so on require maintenance, so an excess of these would be wasteful and costly.

What are the safest and cleanest sources of energy?

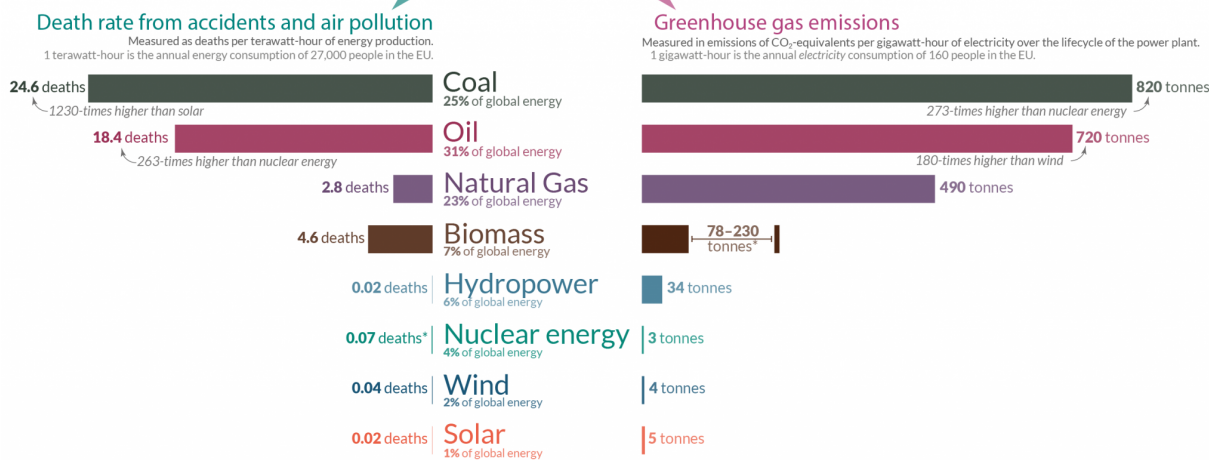


Figure 1.4: Safest and cleanest sources of energy [deathsfromenergysource] - deaths per terawatt hour and tonnes of CO₂ per gigawatt hour

Fossil fuels release carbon dioxide, sulphur dioxide, naturally occurring trace radioactive elements and other pollutants into the atmosphere. These power plants are useful because the fuel is cheap, but the waste is put back into the environment without much processing and the energy produced may be varied to meet the demand of the national grid.

Nuclear power has a bad reputation with the public, in part caused by accidents such as the Windscale fire, Three Mile Island, Chernobyl, and Fukushima. There have been examples of poor handling of nuclear waste in the past, such as the legacy storage ponds at Sellafield, and long term storage in geologically stable areas is something that hasn't been achieved to store the existing waste, let alone waste created in the future.

Modern nuclear power plants are very expensive to build, with the proposed 3.2GWe Sizewell C power plant expected to cost 20 billion or more [ftnppcost]. When compared to £0.5 billion for the 0.884GWe Carrington CCGT Power Station [efgccgtcost], the initial costs are £0.57 billion per GWe for CCGT compared to £6.25 billion per GWe for Nuclear.

There is an effort around the world of countries aiming to reduce the production of carbon dioxide as a result of burning fossil fuels. When a power plant is operational, the carbon dioxide produced by nuclear power is negligible when compared with gas, oil and coal power plants.

Despite its reputation amongst the public, nuclear is much safer than fossil fuels and is on par with renewable energies. The pollution caused by fossil fuels affects us all and is responsible for many deaths each year, causing more misery than nuclear power ever has (fig. ??). Coal and oil are responsible for 350 and 260 times as many deaths as nuclear.

As a species, we have used combustion of chemicals to generate heat for thousands of years, culminating in high efficiency CCGT power stations, with efficiencies above 60%. We are at the beginning of our journey with nuclear power, with many new and innovative designs proposed, where safety to plant workers and the general public are a priority.

Future designs may help to tackle the problematic waste generated in the past, and by using fertile material to produce fissionable elements other than U²³⁵, the amount of fuel available to reactors will increase.

1.3.2 Planned and Under Construction in the UK

Several sites have been acquired with the aim of building new nuclear power stations in the UK. There are five sites and three reactor designs[[ocw01](#)]:

- Hinkley Point: two Areva EPRs (EDF Energy), Hinkley Point C under construction
- Sizewell: two Areva EPRs (EDF Energy)
- Wylfa: 2-3 Hitachi ABWRs (Horizon Nuclear Power)
- Oldbury: 2-3 Hitachi ABWRs (Horizon Nuclear Power)
- Sellafield: 3 Westinghouse AP1000s (NuGeneration) ...

Two Gen III+ reactors are under construction in the UK: Hinkley Point C 1 and C 2. These reactors are Areva NP designed Gen III+ EPRs, which are PWRs, and the proposed opening years are 2025 and 2026 respectively.

There are also plans to construct a third plant at Sizewell that, if accepted, will be an EPR reactor. Sizewell C will join the decommissioned Sizewell A and operational Sizewell B, that may operate until 2055.

1.3.3 Proposed Generation III+ Nuclear Power Plant Designs

Areva EPR

The 1.6GW Areva EPR design has four primary loops transferring heat by pressurised water from the reactor to heat exchangers. It requires U enriched to 5% 235U in the form of U Oxide Pellets. The inlet temperature is 568.75K and the outlet temperature is 602.95K.

There are 241 fuels assemblies, each containing 265 fuel rods giving a total of 63865 rods. The fuel rod cladding is made from 316 stainless steel and has an inner diameter of 7.72mm and an outer diameter of 9.68mm. The materials used to construct the control rod drive mechanisms includes 410 stainless steel and 304 stainless steel.

There are two EPR reactors planned for the proposed Sizewell C power plant.

Westinghouse AP1000

The 1.1GW Westinghouse AP1000 design is a pressurised water reactor with two primary loops transferring heat from the reactors to heat exchangers. An enriched UO_2 fuel, up to 5% 235U, is clad in Zirlo (a proprietary Zr alloy).

Zirlo is an alternative cladding material to 316 stainless steel, and as a cladding material is absorbs fewer neutrons than steel cladding.

Property	316SS Fe 20Cr 8Ni 1Mo	Zirlo (Hill Approximation)
Bulk Modulus (GPa)	164.9 [elasticprofecr]	98.5 [crystengcommzirlo]
Shear Modulus (GPa)	74.6 [elasticprofecr]	33.2 [crystengcommzirlo]
Young's Modulus (GPa)	194.3 [elasticprofecr]	89.7 [crystengcommzirlo]
Poisson's Ratio	0.30 [elasticprofecr]	0.35 [crystengcommzirlo]

Table 1.1: Bulk, shear, Young's modulus comparison: Zirlo and austenitic stainless steel

The inlet temperature is 552.55K and the outlet temperature is 597.85K which is close to the temperature range of the EPR. The composition of the control rod absorber material includes 304 stainless steel.

1.3.4 Generation IV

Goals of Generation IV Reactors

The GenIV International Forum has put forward four main goals for this next generation of nuclear power[genivgif]:

- sustainability
- safety and reliability
- economics
- proliferation resistance and physical protection

The selection of known materials, and the development of new materials, will play a key part in all four of these goals.

Carnot's Theorem

Whatever the motivation, whether it is to increase profits or to supply energy at greater amounts and for less cost to the consumer, increasing the efficiency of usefully using energy is critical. Solar panels are continually being improved to edge closer to their theoretical limit and wind turbines are being constructed larger and with more advanced materials to extract as much energy from the wind as possible.

In the same way, power plants that use heat are constantly being developed to improve efficiency. In the nineteenth century Carnot showed that the maximum possible efficiency of a heat engine is determined by the difference in temperature between the heat reservoirs.[carnottheorem]

$$\eta_{max} = 1 - \frac{T_c}{T_h} \quad (1.1)$$

To increase maximum efficiency, the temperature difference should be increased, and this leads to higher temperature reactors. There will be a trade off between the increased temperature, the ability of the materials to withstand the temperature, health and safety considerations, the lifetime of components, the effect on the coolant and more.

The first generation of reactors in the UK were the gas cooled Magnox reactors. With core temperatures of approximately $620K$ [magnoxtemp], the thermodynamic efficiency was relatively poor. This was limited by the MgO cladding, which was in turn selected due to the fuel. Combined cycle gas turbines have much higher temperatures within their turbines, and the temperature of the steam within the secondary steam turbine can reach $850K$ [ccppwiki], significantly higher than in a Magnox reactor.

The second generation of power plants, particularly in the UK, included the advanced gas reactor that used C_2 as a coolant. This reactor design increased temperatures to over $870K$, and thus the maximum possible thermodynamic efficiency was increased.

Several Gen IV reactors have designed operating temperatures that exceed those of the AGR, and this brings a new set of challenges to overcome.

Fast Reactors

Examples of thermal neutron reactors include Magnox, AGR, LWR and Candu reactors. These reactors contain moderators, designed to slow neutrons, decreasing their energy to thermal temperatures and leveraging the large neutron fission cross section of U-235. The cross section for fast neutrons and U-235 is in the region of 1 barn, but thermal neutrons and U-235 have a fission cross section of over 1,000 barns.

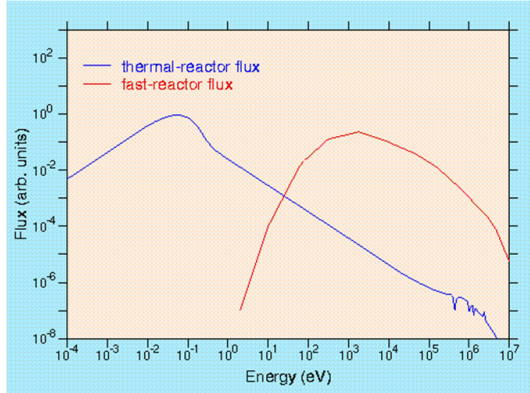


Figure 1.5: Typical Reactor Flux - Thermal and Fast Spectra

Natural U contains 0.7% U-235 and 99.3% U-238[[uranium enrichment](#)]. The thermal fission cross section for U-238 is small for thermal neutrons, and can be measured in the microbarn to millibarn range, but it has a much higher fission cross section with fast neutrons with a cross section closer to 1 barn for neutrons with an energy of 1MeV or more. The neutron flux in a fast reactor is spread over a higher energy band than that of a thermal neutron reactor (fig. ??).

Fast neutron reactors have been tested and used since the 1950s, and there are several Gen IV reactor designs based on this approach. Given the much larger percentage of U238 in natural U, Fast Neutron Reactors have a larger stockpile of fuel. They also breed fissile isotopes, Pu 239 and 241. This has its advantages and disadvantages. The advantage is clear, as it produces fissile fuel as it runs, but the creation of fissile materials is a concern as these isotopes could be used in nuclear weapons.

Lead-cooled Fast Reactors

Light elements such as the hydrogen in water molecules, or carbon in a graphite stack, allow neutrons to efficiently lose energy. When neutrons scatter inelastically with heavier elements, such as lead, they lose a much smaller percentage of their energy.

The Lead-Cooled Fast Reactor (LFR) uses lead as the coolant. Lead has a low reaction cross section and, because of its mass relative to a neutron, the kinetic energy lost in collisions is low, keeping more neutrons in the fast energy group. As the coolant is a liquid, and the boiling point of lead is over 1,970K, the system will run at atmospheric pressures and any problems associated with void formation due to boiling is removed. The molten lead will act as a gamma shield and it will be chemically less reactive than the coolant in a Sodium-Cooled Fast Reactor (SFR) or Supercritical-Water-Cooled Reactor (SCWR).

There are several disadvantages to using lead as a coolant. The melting point of lead is 600K, so the reactor would need to be heated first for the coolant to become a liquid. This also restricts the lowest temperature and thus the maximum efficiency possible that may be extracted from the system without the coolant forming a solid. The density of lead also poses a problem for the structure needed to support the reactor.

European Lead Fast Reactor (ELSY) is a 600MWe Lead-Bismuth eutectic cooled fast neutron reactor. It has a lower melting point than lead, but there are concerns for the transmutation of Bismuth to Polonium. The

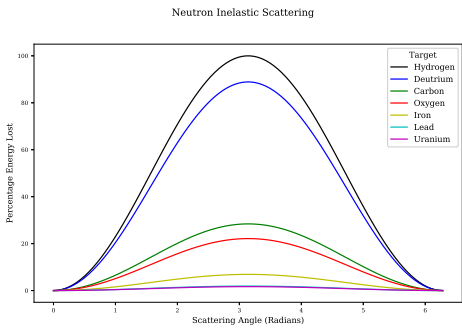


Figure 1.6: Inelastic scattering - scattering angle vs energy loss for a range of target atoms

9,000 tonne molten lead coolant and the high flux of fast neutrons[[lanltour](#)] will be challenging conditions to overcome.

VHTR

Traditional nuclear power plants, as well as coal and the secondary cycle of CCGT plants, boil water to drive turbines. Very-High-Temperature Reactor (VHTR) designs use thermal neutrons and a fissile fuel. Designs plan to have outlet temperatures of up to 1,270K[[genivgifuvhtr](#)]. With a helium coolant, there are several options.

- directly drive turbines
- heat water to create steam and drive turbines
- use the high temperature to help create hydrogen, and combine with steam driven turbine

Hydrogen may be extracted from high temperature water either by a thermo-chemical, high temperature electrolysis or hybrid process[[hydrogenhtr](#)], and they all benefit from the very high temperatures provided by the predicted outlet temperatures (fig ??).

The Pebble-Bed Reactor (PBR) is a type of VHTR where spherical fuel pellets are held in a hopper shaped reactor. Temperatures within the core may reach 1,770K, and this will pose a challenge for materials scientists.

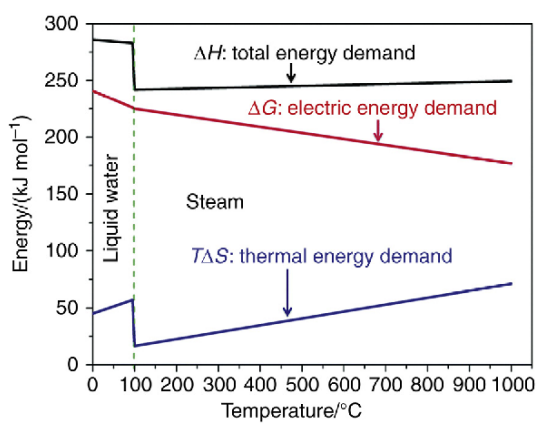


Figure 1.7: Energy demand to produce hydrogen by electrolysis as temperature changes

GFR

The Gas-Cooled Fast Reactor (GFR) design is similar to the VHTR, but rather than use thermal neutrons, it will use fast neutrons. The design will use a ceramic core and have outlet temperatures up to $1120K$. This will give similar options to the VHTR where high temperatures would be used to assist in the production of hydrogen, or it would be used to power a turbine with a secondary steam powered circuit similar to that of a CCGT.

There are challenges ahead, including the development and testing of advanced materials that can withstand these temperatures while under high energy neutron flux. However, unlike LFRs, SFRs and SCWRs, the coolant is chemically inert and isn't transmuted by neutrons removing the risk of the coolant becoming radioactive.

SFR

Memories of small amounts of sodium, kept under oil in school chemistry labs, being carefully cut and prepared ahead of a violent reaction with water, probably come to mind at the first mention of an Sodium-Cooled Fast Reactor (SFR). It may not be the first choice of an element to use as a coolant, but it does have advantages.

Sodium has a low melting point, of just under $370K$, and a boiling point of $1,150$. With an operating temperature of up to $820K$, the reactor would be able to run at atmospheric pressure and without the issues associated with the coolant boiling. Its density is $0.971gcm^{-3}$. Comparing this to the LFR the coolant would be 12 times less dense and this would have advantages when designing the structure.

There have been several SFRs built and operated using this technology, such as the Russian BN-600 reactor. This particular reactor has a sodium primary loop which heats a secondary sodium loop which in turn heats a third loop for water and steam.

SCWR

At $647K$ and a pressure of $22.1MPa$ (approximately 218 atmospheres), water becomes supercritical (fig. ??) which is neither a liquid or a gas[advancedbiomass]. The current generation PWR and BWR operate at approximately $501 - 598K$ at $15.2MPa$ [ocw01] and $551 - 560K$ at $7.1MPa$ [ocw02] respectively.

Supercritical water exists above $647K$ and $22.1MPa$, and in this state water has a higher thermodynamic efficiency. The design of the nuclear power plant is also simplified as there is no phase change of the water, so a condenser is not needed. The Supercritical-Water-Cooled Reactor (SCWR) is the only Gen IV reactor design that uses water as the coolant[gen4]. The economic benefits have already been seen in SCW fossil fuel power stations, and it is incorporated in Gen IV water cooled fast and thermal reactors.

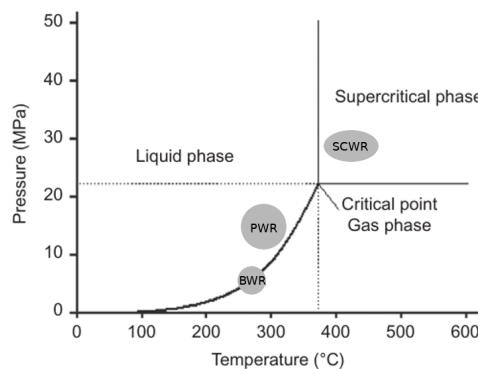


Figure 1.8: Phases of Water: Pressure vs Temperature

There are side effects to using supercritical water. It is an oxidant and is now being considered to “burn” organic waste in future waste processing plants. The combination of supercritical water chemistry and irradiation damage must be considered, as well as higher temperature and pressure, when considering the materials used by a SCWR.

Molten Salt Reactor

MSRs have been operated for over 50 years. Chemically, salts are very stable, and this has obvious safety benefits over reactors like the SFR. The coolants are fluoride salts that have high boiling points which gives the added safety protection of being able to operate at atmospheric pressure, unlike a PWR where a pressure vessel is needed.

The fuel is dissolved into the molten salt. There are no solid fuel rods to place into the core, remove or reprocess. The molten salt is processed on the site to remove poisons, waste and add new fuel.

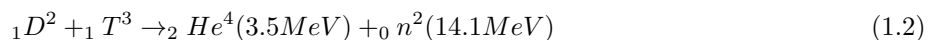
MSRs may use either thermal or fast neutrons and a range of fuels including Th. This is particularly interesting as Th is three times as abundant as U and would increase the fuel available to us to use to generate nuclear power.

A safety feature that takes advantage of the fuel being dissolved in the molten salt are large drain tanks under the reactor. A plug is designed to melt if it reaches a certain temperature and this would quickly drain the molten salt from the reactor into large and cold drainage tanks. The reactivity would drop and the fuel would cool reverting it to a solid salt.

Salts considered in various designs are chlorides, nitrates and fluorides. Corrosion of the reactor due to the molten salts is a concern. Elements that provide protection to corrosion, such as Cr, are prone to dissolution into the molten salt[msrcorrosion]. Where the fuel is suspended in the molten salt as Tristructural Isotropic (TRISO) fuel particles, formation of chromium-carbide precipitates may be an issue.

Experimental Fusion Reactors

Nuclear Fusion is a very attractive technology and could be the answer to all of our energy problems. Much work is being invested in developing this technology and the International Thermonuclear Experimental Reactor (ITER) has been designed to output more energy than is required to start the fusion reaction. The process of fusion combines two isotopes of hydrogen and leaves helium and fast neutrons (eq. ??). As neutrons have no charge, they can penetrate shielding causing damage as they lose energy through nuclear interactions. Any atoms they interact with have a chance to capture the neutron and become unstable.



The fast neutron spectrum for fission reactors ranges from a few eV to a few MeV, whereas the neutrons in a fusion reaction have 2-3 times more energy than the most energetic neutrons from fast fission. Engineers must develop materials to construct components that will be resilient to this damage, while having a low reaction cross section and being able to withstand other extreme conditions within the reactor.

Unfortunately, nuclear fusion as a commercial method of creating energy, is often said to be 30 years away, and this has been the case for some time now. It is a lot to ask, recreating a process that occurs within a star, in a safe and steady manner. Once this problem is solved, it could mark a turning point for human civilization.

1.4 Damage to Nuclear Core Components by Neutrons

Radiation damage in a reactor is caused by several projectiles. Fission fragments are heavy, contain charged particles and lose energy close to their source. Gamma rays excite electrons, promoting them to higher energy levels, or ionise the atoms where there is enough energy to eject electrons completely from atoms. They do not have the momentum to knock atoms out of place. Fast neutrons, however, may impart a great deal of momentum to a target atom and, as they are neutral, travel much further into a material than fission fragments. With enough energy, neutrons cause large damage cascades within the material.

One fuel source for many of the Gen III+ and Gen IV reactors is U-235, whether as enriched U or otherwise. The neutron(s) released by the fission of U-235 atoms have a spectra of energy (fig. ??) which may roughly be split into four categories: cold (below 0.025eV), thermal (0.025eV), slow and intermediate (above 0.025eV and below 1MeV) and fast (1MeV and above).

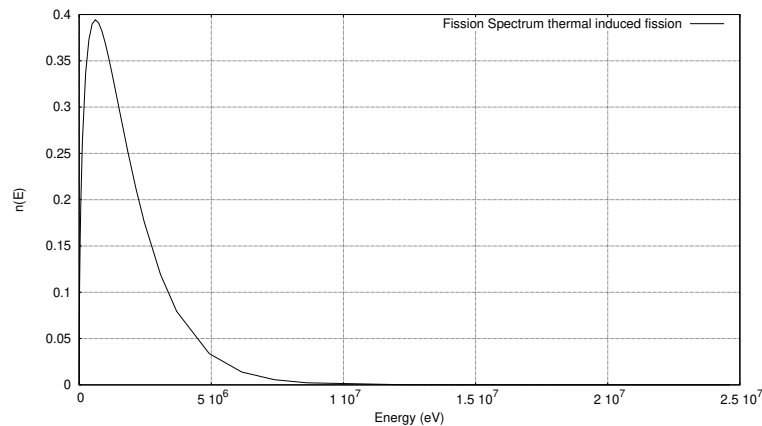


Figure 1.9: Neutron Energy Spectrum from Fission [jeff311]

Thermal and slow/intermediate neutrons cause damage in their own particular way, as they are captured by and transmute the atoms within the target material. Fast neutrons have enough energy to create a great deal of damage, whereby they transfer kinetic energy to an atom in the material that become the primary knock-on atom (PKA) in a cascade of atoms through the material. Neutrons can travel deep into a material, creating many damage cascades through the material until they lose enough energy or pass through the material completely.

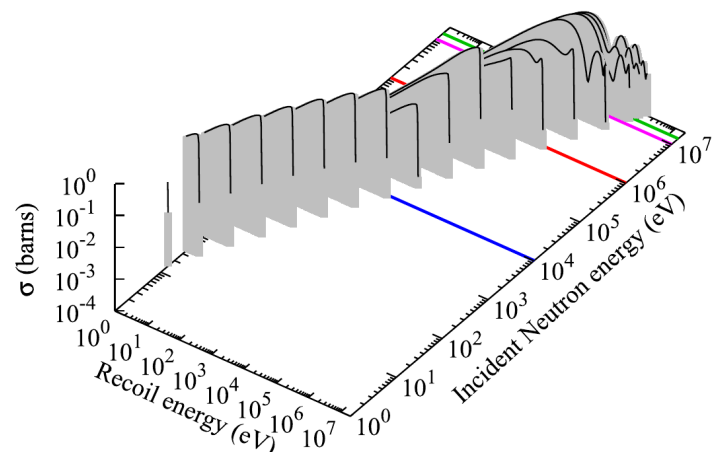


Figure 1.10: PKA energy as a function of neutron energy in Fe [pkaenergyspectra]

The intensity of neutron energies from the fission of U235 peaks around 1MeV (fig. ??). The energy transferred

to PKAs will vary depending on the mass of the target nucleus and scattering angle but, in Fe at least, 1MeV neutrons will create the majority of its Fe PKAs with energies ranging from 1keV to 100keV (fig. ??).

1.5 Radiation Damage: Replacing Neutrons with Protons

It is difficult to generate large fluxes of neutrons. When we pick up a cup, press keys on a keyboard, they react because of the electromagnetic force. Neutrons have no net charge, so they cannot be controlled in a similar way. Nuclear reactors are the most common way to create large fluxes of neutrons.

This is an expensive method, and one that may be inconvenient as the sample being tested would need to be placed inside a reactor. Rather than do this, ions may be used to replicate the damage caused by neutrons, but in a more controlled and accessible way.

A major side effect from the process of nuclear fission is the creation of both radioactive fission fragments and radioactive isotopes within the components and structural material of the reactor. Low energy protons are not captured as low energy neutrons would be, due to the opposing electromagnetic force between the proton and nucleus of the target atom. Once the proton energies exceed a few MeV, they have sufficient energy to transmute target nuclei.

Thanks to detailed reaction cross section data files and decay data, the amount of radioactivity induced by both protons and neutrons can be calculated. This will assist in the selection of proton beam parameters to replicate irradiation damage, to the required DPA, whilst keeping the radioactivity at a safe level.

1.6 Simulation Material Damage

Irradiating and testing materials irradiated by both neutrons and protons have a number of drawbacks, including expensive facilities and the creation of radioactive waste. Simulations may be used to help understand the processes on a mesoscopic scale and make predictions on how the material in question may behave inside a reactor under certain specified conditions.

Part of this work focuses on the damage of stainless steel by neutrons. The damage process occurs on time scales and sizes too small to capture experimentally and play back to study. The theories may not be sufficiently well understood, or are often unsolvable with current techniques. Modelling helps bridge the gap between theory and experiment.

1.6.1 Molecular Dynamics

Molecular dynamics models have been used to simulate radiation damage. Damage cascades caused by primary knock-on atom (PKA)s with energies of 10, 20 and 50KeV have been modelled in BCC W[**damagebcc tungsten**], whilst cascades caused by PKAs of 5, 10 and 20KeV have been simulated in BCC Fe[**damagebcc iron**].

Neutrons have a long mean path before interacting with a target when compared to ions. It would be impossible with current and foreseeable technology to simulate a neutron travelling through a material because the volume of the material, and the number of atoms and interactions between atoms, would be so large. Rather than attempt this, it is more productive to focus on individual damage cascades caused by PKAs in order to conserve computing resources.

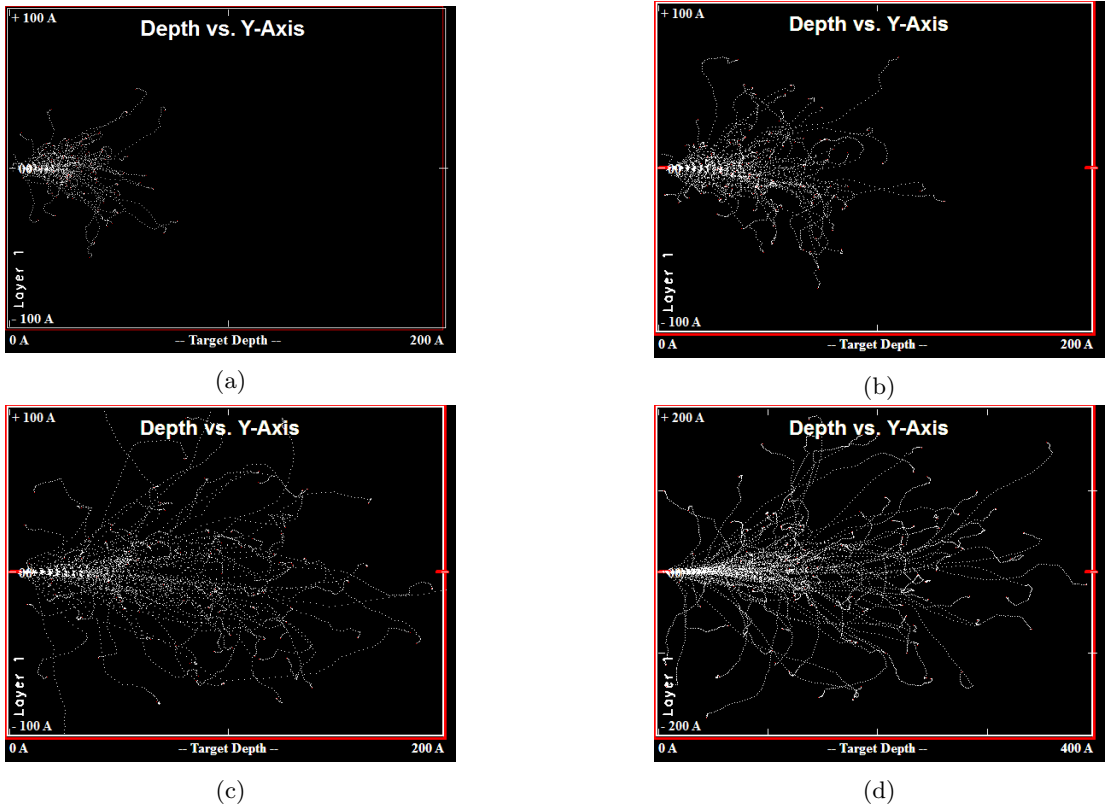


Figure 1.12: (a) 5KeV Fe PKA Damage Cascade in Fe (b) 10KeV Fe PKA Damage Cascade in Fe (c) 20KeV Fe PKA Damage Cascade in Fe (d) 50KeV Fe PKA Damage Cascade in Fe

Molecular Dynamics simulations require interatomic potentials to govern how the atoms in the simulation interact with one another. Typical simulation sizes range from thousands of atoms to millions of atoms.

Fe has a density of approximately 8.5×10^{-2} atoms per cubic angstrom, and this leads to simulation sizes between almost one million atoms and fifty million atoms for cascades with PKAs ranging from 5KeV to 50KeV (fig ??, table ??).

PKA Energy (KeV)	Volume (Ang^3)	Atoms
5	1.0×10^6	9.0×10^5
10	6.0×10^6	5.4×10^6
20	8.0×10^6	6.9×10^6
50	6.4×10^7	5.5×10^7

Table 1.2: Approximate simulation sizes by PKA energy

The interatomic potentials used to simulate a damage cascade must be able to model the very close separations during the collisions event. For very close separations, an exponential potential such as the Ziegler-Biersack-Littmark (ZBL) potential may be used, and for other separations a standard potential such as the embedded-atom method (EAM) may be used, in particular for metals.

There have been attempts to create potentials based on Physics, but the nuances are still poorly understood and there aren't any models that can be applied accurately to any material type under any set of circumstances. A number of recent interatomic potentials, including a selection of transition metals, have been fit to match the experimental data rather than the underlying physics.

1.6.2 Density Functional Theory

In quantum mechanics, the Schrödinger equation and the wavefunction of a system describes all that can be known about that quantum system. Unfortunately, it is very difficult to compute when there are just several electrons in the system. Many atoms in a system makes this an impossible task with current technology.

Density Functional Theory (DFT) replaces the many electron wavefunction with a single electron wavefunction. Rather than use the positions of all the electrons, which would result in 3^n parameters, the charge density, which varies in space with just 3 parameters, is used.

DFT allows for the calculation of the forces between atoms and the energy of that collection of atoms by replacing the many parameters to give the coordinates of many electrons with the three coordinates for the charge density. From the forces the optimum (relaxed) basis vector and atom positions may be computed, and from the energy of multiple configurations other properties are computable (bulk modulus, elastic constants, etc).

1.6.3 Interatomic Potentials for Molecular Dynamics

Interatomic potentials help to describe the interaction between atoms. Originally they were used for pairs of atoms and a collection of atoms on a pair by pair basis, but in the 1980s the complexity of potentials increased as they started to include the effects of the background electron density that the atoms are embedded in. This lead to the Finnis-Sinclair (FS) and embedded-atom method (EAM) type potentials.

Whilst DFT is a purer form of computational materials science, more closely linked to physics, it is computationally intensive and suitable for small systems of hundreds to thousands of atoms. By using interatomic potentials to recreate the forces and energies that would be computed by DFT, the systems may be increased in size to thousands to millions of atoms, and these calculations may be run over a time frame with hundreds or thousands of time steps.

There are a wide range of potentials, and these are typically selected based on the type of material and the required accuracy. Simple pair potentials may still be used, but angularly dependent potentials have been developed for materials with covalent bonds, and metals use FS and EAM potentials. The potentials are made up of a set of functions, and these functions change from derivation to derivation.

Chapter 2

Background: Ionizing Radiation

There are a wide range of radiation sources and types of ionising radiation. They interact differently with matter, depending on the type of radiation and its energy. Damage may be caused with the radiation transferring energy directly to the target. The target may be transmuted or the surrounding, for example the creation of Cobalt-60 in steel in the nuclear industry. The environment may be changed chemically, and one example of this is the radiolysis of water.

2.1 Radiation Types Relevant to This Work

2.1.1 Introduction

There are three types of radiation that are useful to discuss in this work, neutrons, ions and Ggammas, and two of these (neutrons and protons) are of particular interest in this work. Each of these are capable of ionizing the atoms they interact with, given sufficient energy. Higher energy and momentum radiation it is able to directly damage materials, or the DNA structure of organic life, that it interacts with. Lower momentum ionizing radiation may change the water chemistry of the environment or within the cells of organic lifeforms that is detrimental to life.

2.1.2 Protons and other Ions

Charged particles interact with matter through the Coulomb interaction. As a charged particle passes through matter, it may interact with both the nucleus and electrons of an atom. A sufficiently energetic ion may lose kinetic energy to electrons by either raising the electrons to higher energy levels in their atoms, or by removing electrons from atoms altogether, causing the ionization of those atoms.

Ions may also lose kinetic energy to the nucleus of an atom through elastic scattering and, where the atom is in a crystal structure, through knocking atoms in the material out of their lattice positions. Inelastic scattering is also a possibility, leaving the target nucleus in an excited state.

Knock on atoms and electrons with enough kinetic energy that have been removed from atoms (delta rays), continue the irradiation of the material while they have the kinetic energy available to do so.

A large proportion of the energy of a charged projectile is lost to the electrons of the target material. There is a chance, depending on the energy and type of charged projectile (and the cross section of the target nucleus), that the charged particle will overcome the coulomb potential and be captured by the nucleus.

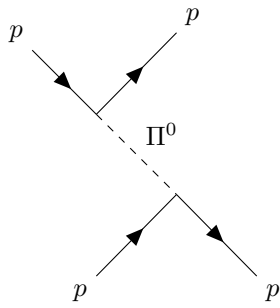


Figure 2.1: Direct interaction p-
p[pionexchange]

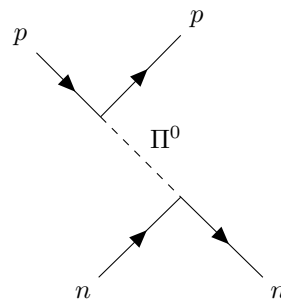


Figure 2.2: Direct interaction p-
n[pionexchange]

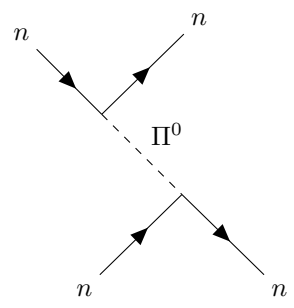


Figure 2.3: Direct interaction n-
n[pionexchange]

This may result in a stable nucleus or an unstable nucleus. If it is unstable, there is a probability that it will decay releasing energy in the form of photons, nucleons or electrons. The initial ion irradiation creates sources of further radiation within the target material.

2.1.3 Neutrons

Neutrons interact with matter differently to that of protons, ions and other atoms, as the neutron has no overall charge. Neutrons do have a magnetic moment and experience a weak interaction with unpaired electrons by a dipole-dipole interaction. Neutrons also interact with the nucleus of atoms, and this is dependant upon the target atom and the energy of the projectile neutron. The energy of neutrons may be grouped as shown in table ??, and as mentioned earlier, thermal neutrons are of interest to current reactor designs, and fast neutrons are of interest to several future designs.

Name	Energy Range	Velocity/ms ⁻¹	Wavelength Ang
Cold	0-0.025 eV	$0.0 - 2.2 \times 10^3$	> 1.8
Thermal	0.025 eV	2.2×10^3	1.8
Epithermal	0.025-0.4 eV	$2.2 \times 10^3 - 8.8 \times 10^3$	0.5-1.8
Cadmium	0.4-0.6 eV	$8.8 \times 10^3 - 1.1 \times 10^4$	0.4-0.5
Epicadmium	0.6-1.0 eV	$1.1 \times 10^4 - 1.4 \times 10^4$	0.3-0.4
Slow	1-10 eV	$1.4 \times 10^4 - 4.4 \times 10^4$	0.09-0.3
Resonance	10-300 eV	$4.4 \times 10^4 - 2.4 \times 10^5$	0.02-0.09
Intermediate	300 eV - 1 MeV	2.4×10^5	$2.9 \times 10^{-4} - 0.02$
Fast	1-20 MeV	$1.4 \times 10^7 - 6.1 \times 10^7$	$6.5 \times 10^{-5} - 2.9 \times 10^{-4}$
Relativistic	> 20 MeV	$> 6.1 \times 10^7$	$< 6.5 \times 10^{-5}$

Table 2.1: Neutron Categories by Energy Range [njcarron]

The nuclear force holds nuclei together by exchanging pions. It is 137 times stronger than the electromagnetic force, but because of the mass of the pion (approximately 130-140MeV) it only acts over a short range of approximately 1fm. The nuclear force is attractive but has a short-range repulsive core.

For nuclear reaction and damage calculations, the interaction of neutrons with matter is represented by a cross section (section ??). Cross sections are used to calculate the probability of a certain interaction occurring and are dependent upon the target nucleus, how much of the material the pass through and the energy of the neutron.

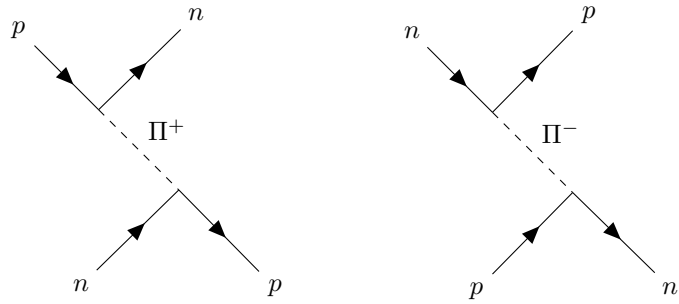


Figure 2.4: Exchange interaction n-
p[pionexchange]

Figure 2.5: Exchange interaction p-
n[pionexchange]

2.1.4 High Energy Photons

The electromagnetic spectrum classifies photons based on their energy and/or source, but visible light, x-rays, gamma rays and so on are all the same elementary “particle”. During the early years of Quantum Mechanics, the relationship between the energy and wavelength of a photon was discovered: the Planck-Einstein relation (eq. ??).

$$E = hf \quad (2.1)$$

Pair Production

The energy of photons in the database used for this work ranges from 1keV up to almost 10MeV. There are several ways high energy photons will interact with the atoms of a target material. The rest mass of an electron is 511keV. If the photon energy is greater than 1.02MeV, i.e. there is at least enough energy to create an electron and positron, there is a chance that the photon will create an electron-proton pair.

$$hf = (m_e + m_p)c^2 + T_e + T_p \quad (2.2)$$

The creation conserves energy and mass, with excess energy carried away as the kinetic energy of the particle pair. The charge before the creation is zero, as the photon is neutral, and the charge after is also zero, with the -1 of the electron and +1 of the positron cancelling out. Angular momentum is also conserved; the photon is a spin 1 Boson and, as electrons and positrons are Leptons they have half integer spin, adding up to 1. Finally, momentum is not conserved in a vacuum, and this is why pair production occurs in the coulomb field of a nucleus. The nucleus carries away excess momentum, fulfilling this conservation law (fig. ??).

Compton Scattering

An incident photon with enough energy may interact with the electron of an atom, and if it transfers enough kinetic energy it will eject the electron from the atom (fig. ??). A lower energy photon is also created that carries away the remainder of the energy, but also linear momentum, as both energy and momentum must be conserved.

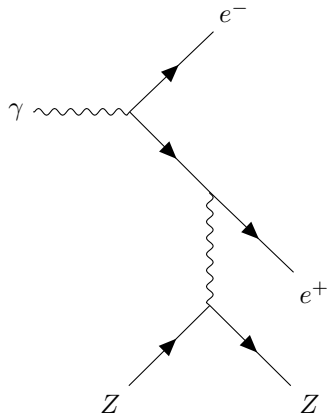


Figure 2.6: Pair production Feynman diagram

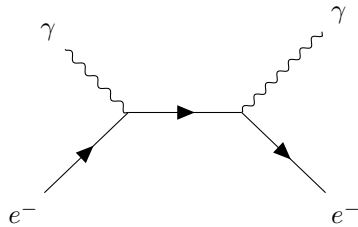


Figure 2.7: Compton Scattering Feynman diagram

Photoelectric Effect

Photons of sufficient energy interact with and eject electrons from the surface of a metal (fig. ??). At lower energies, the photons have no effect on the electrons. Ejected electrons have a maximum kinetic energy equal to the difference between the energy of the interacting photon and the workfunction, $T_{max} = h\nu - \phi$.

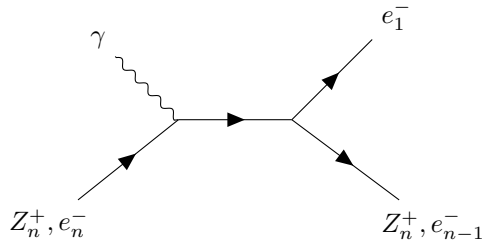


Figure 2.8: Photoelectric Effect Feynman diagram

Coherent Scattering

Lower energy, non-ionizing photons, have insufficient energy to eject electrons (fig. ??). Coherent scattering is the interaction in which photons change direction, scattering, without losing energy.

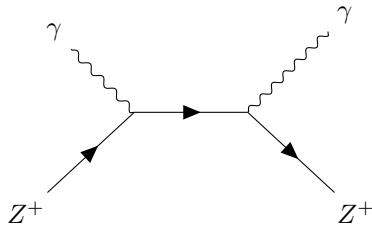


Figure 2.9: Coherent Scattering Feynman diagram

2.2 Effects of Radiation on Organics

2.2.1 Dose: A Multitude of Units and Definitions

There is a distinction between how radioactive a source is and how much radiation is absorbed by an organic due to that source. There are different measures of radioactivity and its effects, and they may be summarised very briefly as follows:

- Radioactivity of a source - decay events per second (Bq) (also measured in Curie, 3.7×10^{10} decays per second)
- Absorbed dose of any target - energy absorbed per unit mass (Gy) (equivalent of Joules per Kilo)
- Equivalent dose absorbed by tissue/organ - type of radiation is important (Si)
- Effective dose on tissue/organ - how the equivalent dose affects the specific tissue/organ (Si)

One joule of ionising radiation absorbed by a person may not seem a lot of energy, but the average annual doses are so small they are measured in millisieverts per year. A dose of just 5 Sieverts is enough to kill 50% of people within 1 month (table ??).

Exposure	Dose (mSv)
Dental X-ray	0.005
Chest X-ray	0.02
UK average annual dose	2.7
Whole body CT scan	10
Nuclear industry employee annual exposure	20
Acute radiation effects	1,000
50% lethal dose within 1 month	5,000

Table 2.2: Irradiation dose comparison in mSv

2.2.2 Levels of Radioactivity from Neutron Irradiated Components

In work by Rodenas and Verdu a MCNP5 simulated neutron flux environment and a thermal flux of $2.5 \times 10^7 n/cm^2 s$ a stainless steel cylinder (20mm diameter and 70mm depth) was irradiated for 10 hours[radionuclides]. The sample was composed of 65% Fe, 19% Cr, 2.0% Mn, 1.0% Si by weight as well as small amounts of C, Ti, P and S. After 10 minutes cooling, it was calculated to have an activity of over 1.0×10^7 Bq and, by several orders of magnitude, it was predominantly due to the creation of Mn⁵⁶.

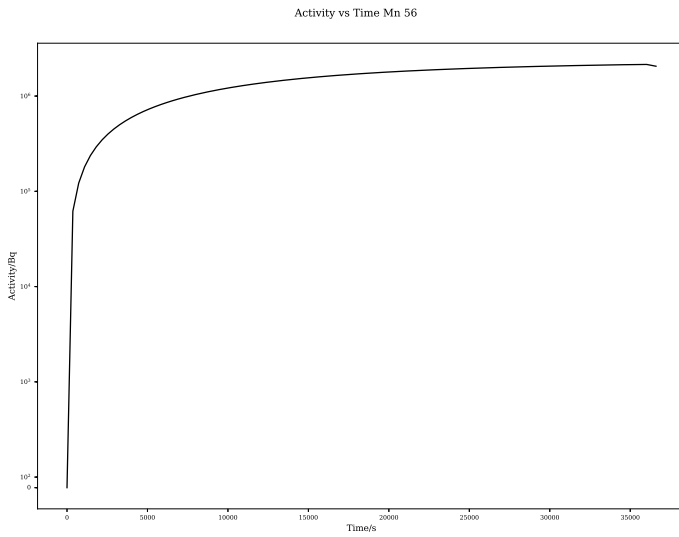


Figure 2.10: Predicted Mn 56 activity after neutron irradiation

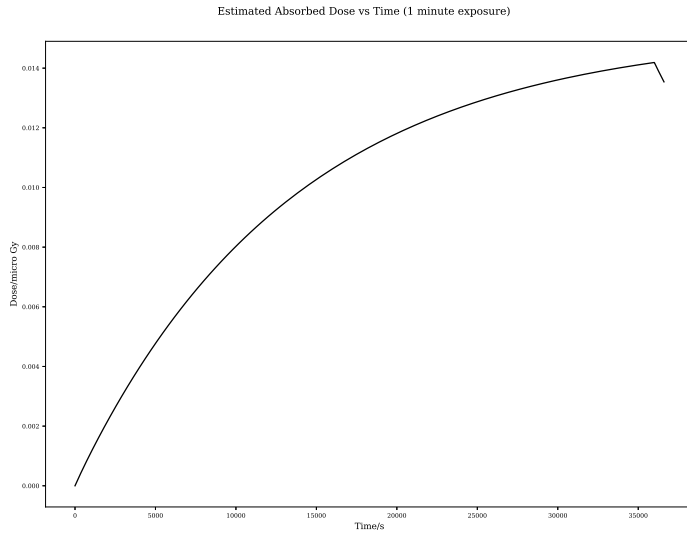


Figure 2.11: Steel Irradiation Gamma Dose 2.5×10^7 neutrons per cm squared per second

The maximum cross section of Mn^{55} (n, γ) Mn^{56} is 2.0 barns and the estimated reaction rate at this flux is just over 2.0×10^6 . As the half life of Mn^{56} is short compared to the irradiation time (a half life of 2.5 hours) the creation rate of Mn^{56} and decay rate equalise, saturating the sample with Mn^{56} .

A simple neutron activation code was developed, which will be discussed in more detail in this work, and the predicted Mn^{56} activity vs time was calculated (fig. ??). The overall gamma dose, for 1 minute of exposure to an 80kg person standing 2m from the source was also calculated (fig. ??). The calculated activity for Mn^{56} was less than that predicted by Rodenas and Verdu [radionuclides], but it was within an order of magnitude. It predicts a total activity after cooling of 2.3×10^6 Bq with almost 90% of this due to Mn^{56} .

The flux in the within the flux trap of the HFIR is much higher, with high energy neutrons having a flux of 1.0^{14} neutrons per cm squared per second (fig. ??). A second calculation was performed for this increased flux, also irradiated over 10 hours (fig. ??). The total activity increased from 2.3×10^6 Bq to 7.1×10^{12} Bq and the overall dose per minute was much higher, between 40 and 50 milligrey per minute over the first hour of cooling. These are dangerous levels of radiation.

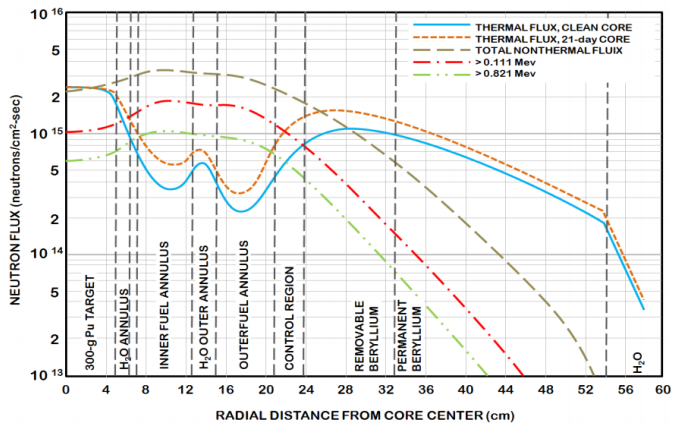


Figure 9: Neutron Flux at the MidPlane of HfIR (at 85MW)

Figure 2.12: High Flux Isotope Reactor Neutron Flux

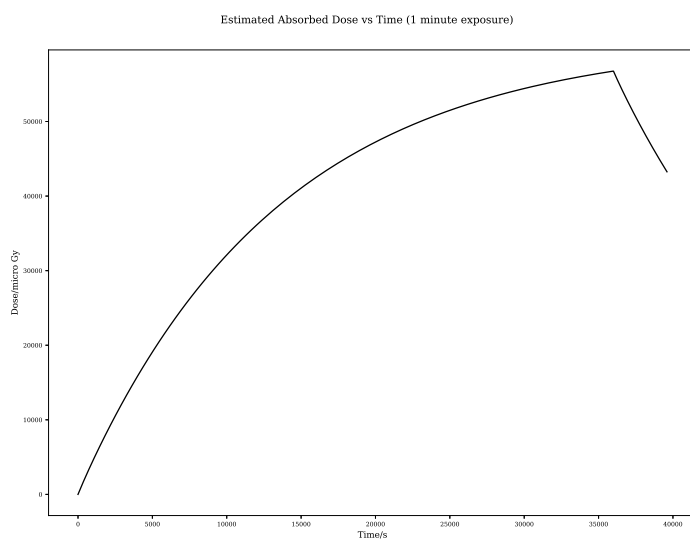


Figure 2.13: Steel Irradiation Gamma Dose 1.0×10^{14} neutrons per cm^2 squared per second

Damage to Organics by Radiation

Life evolved on Earth from single cell to multicelled organisms such as humans. Prokaryotic cells are single celled organisms that do not have a nucleus, an example being bacteria. Our cells are eukarytic cells, and these have a nucleus that contains the genetic information. Millions of cells die in our body every second, and our body replaces these by replicating living cells. During the replication stage, the DNA within the nucleus is copied.

DNA is a polymer that is carefully constructed from six components. Stretched out, it is approximately 2m in length and approximately 25 angstrom wide, and it is neatly contained within the cell nucleus which is on average just 6 microns across. The structure of DNA is the well known double helix. The sides of the helix are made from alternating sugars and phosphates, while the “rungs” of the ladder like structure are pairs of either thymine and adenine or cytosine and guanine. These pairs are covalently bonded to the sugar-phosphate sides, and by hydrogen bonds to each other.

Mitosis is the part of the cell cycle where the DNA within the nucleus is replicated and the cell splits into two. There are repair mechanisms, but if the DNA beyond repair, the cell may die through apoptosis, or it may replicate in an uncontrolled way leading to cancer.

Direct damage is caused when ionising radiation alters or destroys sections of DNA through a direct collision, for example a neutron colliding with and knocking out an atom in the DNA strand.

Our cells are predominantly water, so there is a higher probability of the radiation colliding with water molecules than DNA directly. The chemistry of the contents of the cell is changed, for example by the creation of free radicals, and these lead to damage of DNA as an indirect result of radiation passing through the cell.

2.3 Damage Cascades in Metals

When a metal is damaged by radiation, there are microscopic defects created and removed in a very short space of time. The result of many months or years of damage is complex and will be discussed in more detail in chapter ??.

The cohesive energy of atoms are measured in eV (table. ??), whereas the energy of incoming neutrons or fission fragments are measured in MeV. Radiation in the form of electrons, protons and heavy ions will lose energy to electrons in the target as they pass through. They may also lose energy to atoms within the lattice, knocking that atom out of place and creating a PKA. Due to its neutral charge and magnetic moment, neutrons have a very weak interaction with charged particles. They primarily lose energy directly with the nucleus of atoms within the target, also creating a PKA.

Element	Cohesive Energy/eV
Aluminium	-3.36
Iron	-4.32
Palladium	-3.91
Platinum	-5.77
Zirconium	-6.32

Table 2.3: Cohesive Energies [[shengeamonline](#)]

The PKAs create a damage cascade, and their mean recoil energy is dependent upon the energy and type of radiation. After each cascade, there will be a period of time where the material quenches, with a recombination of some interstitials and vacancies. The PKA creation and cascade thermal spike cover a time range of 10^{-18} s

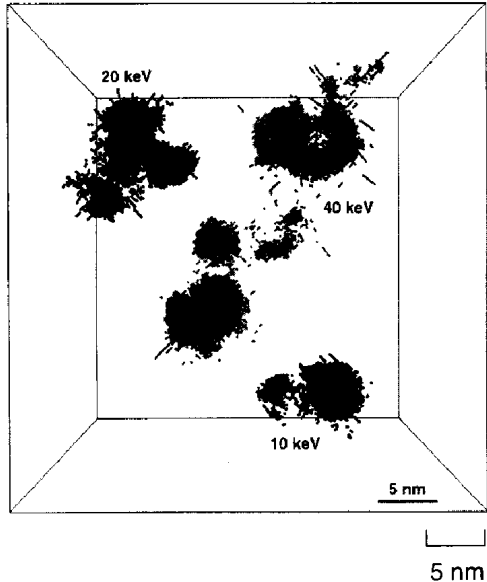


Figure 2.14: Interstitials in the cascades of 10keV, 20keV and 40keV displacement cascades [stollerdamage1996]

to 10^{-13} s, with the quenching phase lasting in the region of 10^{-11} s. However, the cumulative effect of radiation damage on a component within a reactor core may only become apparent after months or years.

Projectile	Mean Recoil Energy
1 MeV Electrons	60eV
1 MeV protons	200eV
1 MeV heavy ions	5keV
1 MeV neutrons	35keV

Table 2.4: Average recoil energy of Nickel PKAs[gswas]

The immediate aftermath of interstitials created three damage cascades is shown in fig. ???. Damage cascades have been the subject of a number of studies and due to their short time scale and complexity, involving thousands to millions of atoms, are studied with computer simulations.

Chapter 3

Background: Austenitic Steels and Nuclear Power

Austenitic stainless steels have played an important role in the nuclear industry. They have a good resistance to corrosion and behave well at moderately high temperatures, having a good resistance to creep. They have been used within the primary circuit and secondary circuit of power stations, as cladding for fuel pellets, in the steam dryers, pre-heater tubing, core structurals, primary piping and more. Ferritic steel is magnetic and has a BCC structure, whereas austenitic steel is non-magnetic with a FCC structure, with its high Nickel content stabilising this phase. An area of concern is the susceptibility of austenitic stainless steels to IGSCC.

3.1 Stainless Steel

3.1.1 Introduction

Stainless steel is a relatively new material, having first been developed and refined from the 1800s to the early 1900s, then being defined as a steel with at least 10.5% Cr in 1911. The addition of Cr to this level causes the formation of a passive protective layer of chromium oxide.

Fe is alloyed with Cr, Nickel and Carbon in varying quantities to make Stainless Steel. Depending on the application, other elements, such as Molybdenum, may be added to enhance the properties of the steel.

3.1.2 Grades of Stainless Steel

While the criteria that qualifies an alloy as Stainless Steel is containing Fe, Mg and at least 10.5% Cr, there are many grades that have variety of properties and atomic structures. The composition influences the structure, resistance to corrosion, yield strength, whether it is magnetic or not, and more.

Both Fe and Cr are BCC at standard temperatures and pressures, but adding austenite stabilisers such as Ni, Mn or C, the structure of the steel can be altered from BCC to FCC. Balancing the proportion of these elements changes the phase of the steel, and this may be represented as a Schaeffler diagram (fig. ??) or a ternary phase diagram (fig. ??).

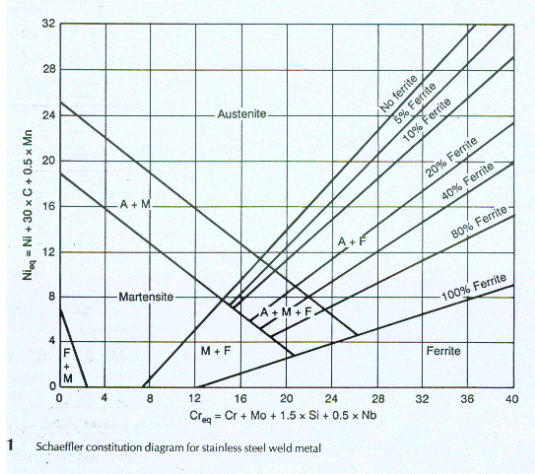


Figure 3.1: Steel Cr-Ni Schaeffler Diagram

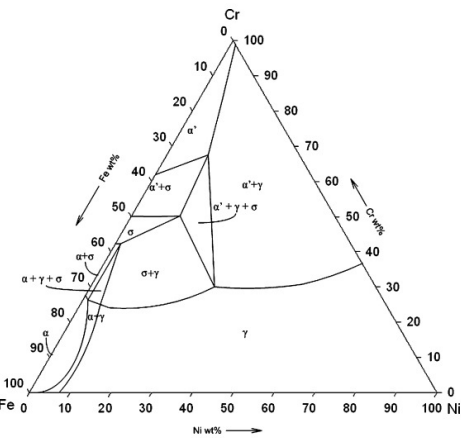


Figure 3.2: Iron-Chromium-Nickel Phase Diagram [fenicrternaryphase]

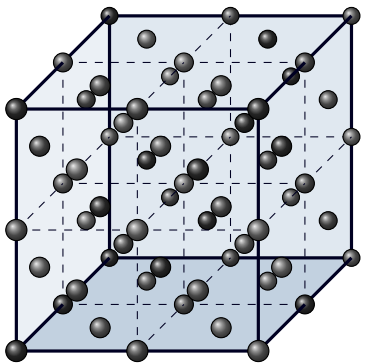


Figure 3.3: BCC structure of ferritic stainless steel

Ferritic Stainless Steel

At room temperatures and pressures, Fe exists in the alpha phase, which is a BCC crystal. It is energetically favourable for the magnetic moments of the Fe atoms to align with one another ferromagnetically. Ferritic stainless steels also have the natural alpha phase crystal structure of pure Fe at room temperature which is BCC (fig ??). These steels are magnetic and may be hardened by cold working. They are less corrosion resistant than austenitic stainless steels. Two common examples of this grade of steel are American Society of Engineers codes 405 and 430.

Austenitic Stainless Steel

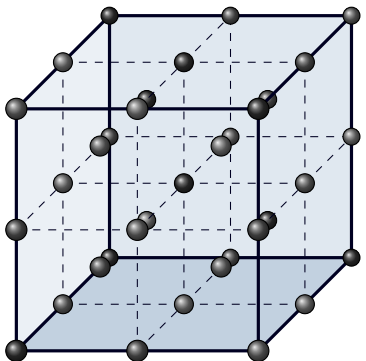


Figure 3.4: FCC structure of austenitic stainless steel

Austenite is a FCC allotrope of Fe (fig ??), and austenitic stainless steels are useful in many applications,

including a structural material for nuclear plant components, due to their resistance to corrosion. In addition to 10.5 wt% or more Cr they require an austenite stabilising element such as carbon and/or nickel to be added.

Two examples of such steels are ASME codes 304 and 316. Both have a high Cr content, in the region of 18-20%, which is in excess of the minimum passive film requirement of around 10-11%. The natural structure of such an Fe Cr alloy would be BCC, however 304 and 316 Steels contain Nickel (approximately 8% and 10% respectively) which is an austenite stabiliser, and this is responsible for the FCC structure of the steel. The 316 grade contains a minimum of 2% Mo to improve its resistance to corrosion.

Ferritic and martensitic have a better resistance to thermal or swelling shock than austenitic [bccfenimodel], but the corrosion resistance of austenitic steels is a deciding factor when choosing a steel for an application where corrosion resistance is important.

Martensitic Stainless Steel

Martensitic stainless steels have a FCC structure at high temperature, but when heat treated take on a BCC structure. This allows martensitic, unlike austenitic and ferritic, to be hardened by heat treatment. These steels are magnetic, they contain more than 10.5% Cr but have a much lower Ni than austenitic grades, if any. They are corrosion resistant, but the corrosion resistance of austenitic steel is typically better. Two examples of such steels are ASME codes 410 and 431. A comparison of properties between common grades of each steel are detailed in table ??.

Grade	Code	HRB	Proof strength (MPa)	UTS (MPa)	Density (kgm^3)	E (GPa)
Austenitic	304	80	230	540-750	7900	200
Austenitic	316	79	240	530-680	8000	200
Ferritic	405	75	250	400-600	7700	220
Ferritic	430	85	280	450-600	7700	220
Duplex	255	32	550	750-1000	7800	200
Martensitic	410	90	205	600	7700	215
Martensitic	420	95	345	700	7700	215

Table 3.1: Common grades of ferritic, austenitic, duplex and martensitic stainless steel and their properties. Hardness using the HRB, ultimate tensile strength (UTS) and Young's modulus E.

3.2 Austenitic Steels in Nuclear Reactors

3.2.1 The Use of Austenitic Steels in Reactors

Due to their excellent strength and corrosion resistance, austenitic steels have been widely used in nuclear reactors. The cheaper to manufacture 304SS and more corrosion resistant 316SS have been particularly popular choices of steel. There are drawbacks, when compared to other alloys including ferritic and martensitic steels, and two in particular are IGSCC and swelling.

3.2.2 Atom Damage Cascades

Fission fragments carry away the majority of the energy released during fission, with an approximate energy of 170MeV per ^{235}U fission event. The fragments are large and have a highly charged positive nucleus that stops rapidly due to the Coulomb interaction with the nuclei of surrounding atoms. Electrons released by beta decay travel a greater distance; they lose energy by interacting with electrons, but may also knock atoms out of place. Neutrons travel further still and lose energy by interacting directly with the nuclei of the surrounding material.

When an incoming projectile hits an atom (the primary knock-on atom (PKA)), it is knocked out of its place and loses energy by colliding with other atoms and to the electrons in the metal. Depending on the energy of the PKA, this causes a damage cascade. Atoms knocked out of their regular position in the crystal lattice leave vacancies behind. The displaced atoms either recombine with vacancies, become interstitial atoms or diffuse to defect sinks. A number of complex problems arise as a result of this damage, and this can take many years and high damage doses to appear.

3.2.3 Damage Rates

The safety of a Nuclear reactor is the primary concern; it must generate power, but it must be safe. It must also be cost efficient. Gen II PWR fuel assemblies were expected to withstand several DPA[genIVstrucmat]. In BWRs the materials are designed to be irradiated by $10^{22} n/cm^2/s$, experiencing approximately 7 DPA over the lifetime of the components[lightwaterallenbusby]. Components in PWRs are irradiated by up to $10^{22} n cm^{-2}s^{-1}$, and are expected to operate up to an irradiation dose of 70 dpa[lightwaterallenbusby]. To remain cost efficient, components in Gen IV reactors will be expected to operate safely up to even higher doses or irradiation damage (fig ??). Components in sodium-cooled fast reactors will be expected to withstand up to 200 DPA over their lifetime to meet the requirements of cost effectiveness and durability[genIVstrucmat].

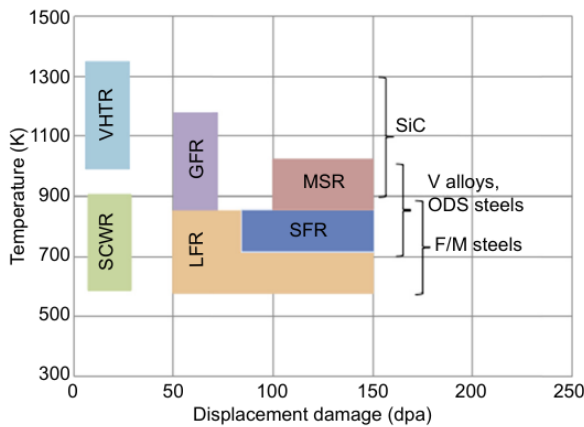


Figure 3.5: Expected DPA during component life time and operating temperatures[genIVstrucmat]

Neutrons released during the fission of U235 range from 0 to 14 MeV (fig ??), and the energy transferred to a target atom depends on the scattering angle of the neutron and the mass of the target nucleus.

$$\alpha = \left(\frac{m_N - 1}{m_N + 1} \right)^2$$

$$E_N = E_n \left(1 - \frac{(1 + \alpha) + (1 - \alpha) \cos\theta_C}{2} \right) \quad (3.1)$$

In a collision, the amount of energy transferred to a target atom will depend on both the scattering angle of neutron recoiling from the target and the mass of the target nucleus. If the neutron does not change direction, a small amount of energy will be transferred, but if it bounces back at 180 degrees it will transfer the maximum amount of energy. A neutron will lose more energy per collision with light atoms (hydrogen, helium, carbon), but much less energy per collision with larger atoms (iron, molybdenum, lead).

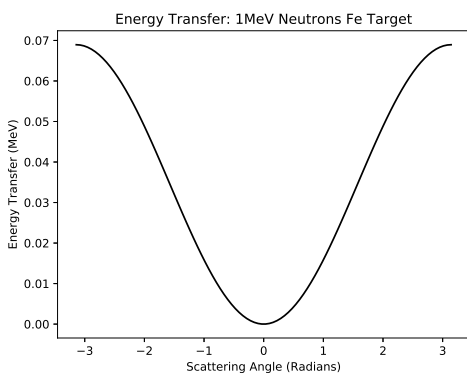


Figure 3.6: Scattering angle probability of neutrons

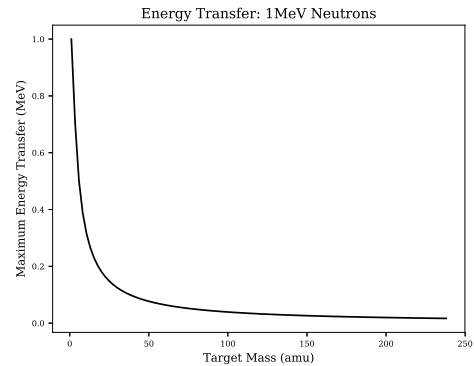


Figure 3.7: Energy transfer as a function of target mass

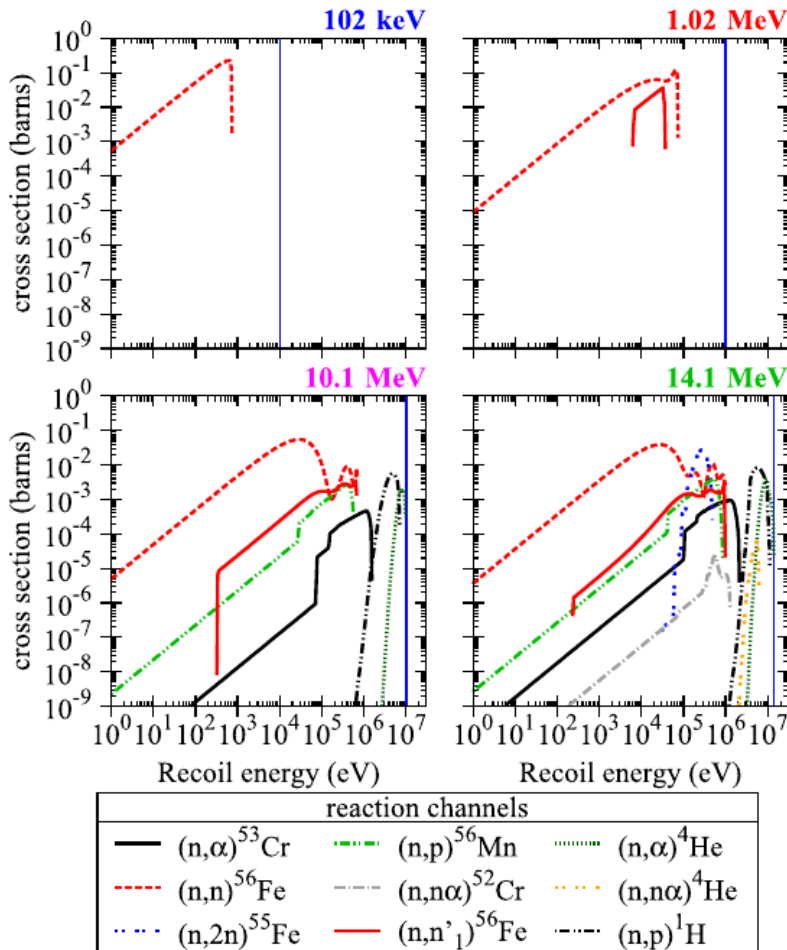


Figure 3.8: Recoil energies for neutrons at 102keV, 1.02MeV, 10.1MeV and 14.1MeV [pkaenergyspectra]

The energy of Fe PKAs as a result of neutron irradiation has been calculated for an Fe target [**pkaenergyspectra**] (fig. ??), and those created by 1MeV neutrons may have an energy up to 100keV. As nuclear reactions are also possible between the neutrons and the target nuclei, there is an inelastic $(n, n)^{56}Fe$ channel as well as other elastic scattering channels where the post collision particles are different to the pre collision particles (fig. ??).

3.2.4 Swelling

Swelling results from damage to the crystalline structure of the metal, and is formed through small voids being created in the crystal. As vacancies are created by radiation damage, they precipitate into small voids. The temperature range for such swelling is primarily from 670K to 870K.

Materials have been known to swell to a 100% increase in their original volume at these intermediate temperatures under irradiation [**wasstrucaustenitic**]. Swelling is sensitive to the total damage amount, the temperature and composition of the alloy. An increase in Ni decreases swelling as does the addition of Zr. Small amounts of P and Mo (0.02% and 0.5-1.0% respectively) cause the swelling of the alloy to increase, however higher concentrations of either cause swelling to decrease [**swellingris**].

As a component swells its properties change. By definition the volume changes, but so does the elastic moduli. Not only this, but the swollen component may stress itself and surrounding components, and this may lead to SCC.

In the EBR-II structural 304SS was irradiated to 20DPA. At a temperature of approximately 650K the steel's volume increased by 2% due to swelling [**radisandvoid**]. With components in future reactors expected to withstand ten times this damage, swelling is a concern. However, increased temperatures and a careful balance in the composition of future alloys will help to reduce this.

3.2.5 Radiation Induced Segregation

The diffusion of atoms within an alloy has an impact on the characteristics of the metal [**nickeldiffusion**]. When radiation causes point defects, these interstitials also diffuse parallel to thermal solute diffusion. At low temperatures, the atoms are unable to diffuse at an appreciable rate; the mobility of vacancies are low [**gswas**] and there are an excess of vacancies due to radiation damage, and this leads to recombination of defects. At high temperatures, there is a higher concentration of thermal defects [**lightwaterallenbusby**]. This increases the defect recombination rate and reduces migration of defects to sinks, such as grain boundaries.

The melting temperature range of 304 and 316 stainless steel are approximately 1695-1722K and 1644-1672K respectively. Gen II reactors, such as Sizewell B, have an operating temperature of several hundred degrees centigrade. The inlet temperature for the Sizewell B PWR reactor is 566K [**sizewellbtemp**] and the outlet temperature is 597K [**sizewellbtemp**]. Operating at approximately 35% the melting point of the steel this is, unfortunately, a good temperature for radiation induced segregation (RIS) to occur.

The Kirkendall effect (KE) concerns the diffusion of one material into another and vice versa at an interface. In the original experiment performed by Kirkendall and Smigelskas, brass (Cu and Zn) was sandwiched between Cu and left at a temperature of over 1050K for almost two months. Using Mo as a marker, it was discovered that Zn diffused out of the brass faster than the copper diffused into the brass. The flux of atoms results in a flux defects and a shrink in volume of brass [**gswasike**].

The inverse Kirkendall effect (IKE) is driven by an external force, such as irradiation. Irradiation of the material causes a flux of defects and, inverse to the KE, this causes a flux of atoms. For an austenitic stainless steel the diffusion coefficients in order of size are $D_{Cr} > D_{Fe} > D_{Ni}$ [**risfecrni**], so Cr will diffuse away from grain boundaries and other sinks, followed by Fe. As Ni is slowest to diffuse, this will be enriched. An additional mechanism that is thought to contribute to RIS is interstitial flux where undersized atoms as interstitials are preferential [**risfecrni**].

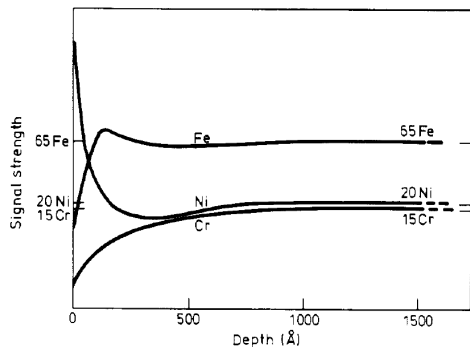


Figure 3.9: Depletion of cr, fe and enrichment of ni at the surface[johnstonris]

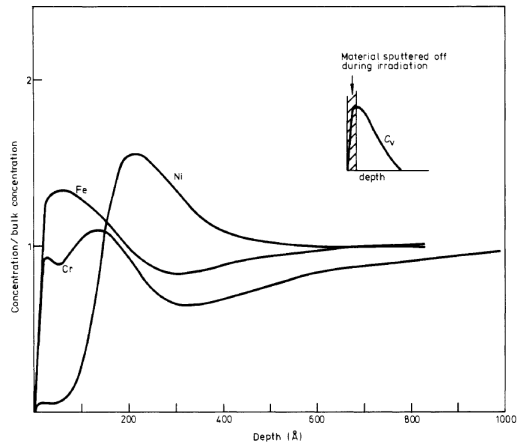


Figure 3.10: Concentration profile after 46DPA irradiation with 75 keV Ni ions[marwickris]

Experimental work by Johnston et al irradiated steel, containing 15% Cr and 20% Ni, with 4MeV Ni ions. It was irradiated to a damage dose of 8DPA at 950K. Some material will have been sputtered from the surface, but in the remaining material Cr, and Fe, were depleted. Ni, however, was enriched (fig. ??).

In work by Marwick a similar alloy with 14% Cr and 15% Ni was irradiated to a much higher dose of 46 DPA with lower energy 75KeV Ni ions. In this instance the damage occurs in a much thinner layer of the surface that was approximately 30nm thick (fig. ??). Conversely to Johnston et al, in this thin layer there is a depletion of Ni and an enrichment of Cr in the first 20nm or so. However, between approximately 25nm and 60nm there is a similar depletion of Fe and Cr as well as an enrichment of Ni.

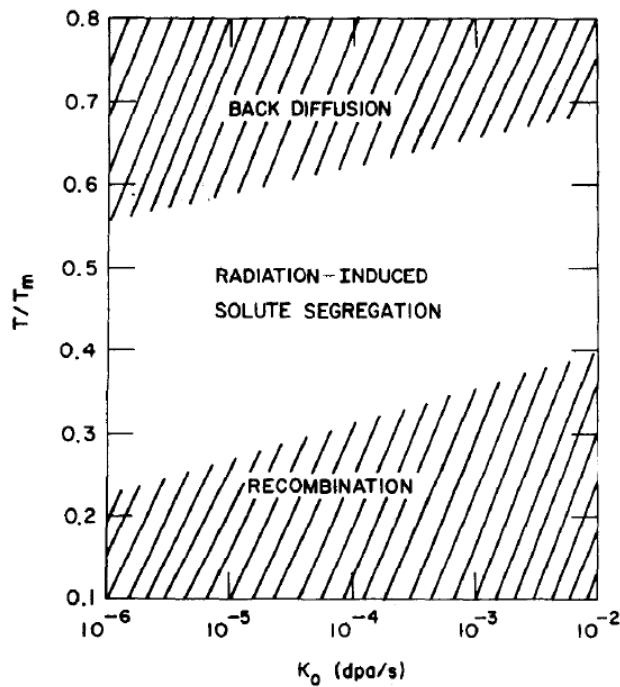


Figure 3.11: Temperature and DPA dependence of RIS[risokamoto]

The underlying mechanisms of RIS are dependent on both the temperature (relative to the melting point of the material) and the amount of damage (fig. ??). The result of RIS is a breakdown in the passive protection of Cr, which leads to IGSCC under the correct conditions.

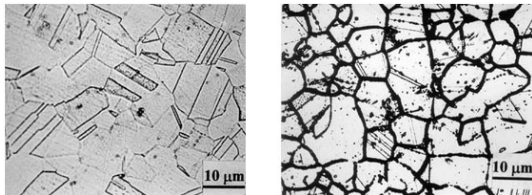


Figure 3.12: Formation of chromium precipitates at the grain boundary [rolledalloys]

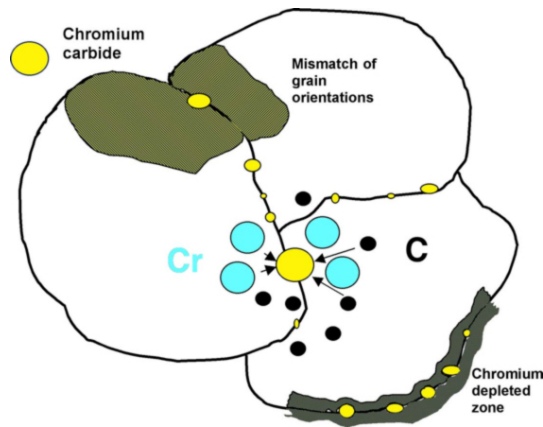


Figure 3.13: Sensitization of an alloy: chromium carbide precipitation [ssina]

3.3 Corrosion Resistance of Austenitic Stainless Steels

3.3.1 Passive Film Protection of Chromium

The addition of Cr improves the resistance of stainless steel to corrosion by orders of magnitude. A very thin passive oxide layer, 20-30 angstroms in width, forms when the surface is exposed to an environment containing oxygen. The protective layer is self repairing and, if the surface is damaged, the oxide layer reforms in the presence of oxygen.

When the steel is in an environment containing oxygen, electrons within the metal tunnel through the surface. As an oxidizing agent, the nearby oxygen atoms readily accept the electrons. A strong electric field forms between positive ions within the metal and the negatively charged oxygen atoms [medicalmetals133].

Fe at the surface of the forming oxide layer is preferentially dissolved away over Cr [kirchheimcc] and Cr ions within the oxide layer have a lower mobility than Fe ions [kirchheimpassive]. Ni remains in place within the alloy, and this leads to an enrichment of chromium oxide in the passive layer. Once the layer is thick enough to reduce the electric field across it, the formation of the layer stops. As mentioned previously, this is at a layer thickness of 2-3nm for stainless steel.

The Cr_2O_3 layer may be formed by heating the steel to 770K[propaustenitic]. However, at higher temperatures, the steel begins to lose its protective layer due to sensitization.

3.3.2 Sensitization and Passive Film Removal

Steel by definition is Fe alloyed with varying small percentages of C. C changes the property of the alloy, and one example of this is an increase in hardness over pure Fe. At elevated temperatures, 670K to 1020K, the added Cr within the steel forms precipitates of Fe-Cr carbides $(\text{FeCr})_{23}\text{C}_6$ at the grain boundaries, reducing the percentage of Cr at the grain boundary and removing the layer of passive protection.

The sensitization of the steel can be reversed. By heating the steel further, to approximately 1,320K to 1,420K, the steel is solution annealed dissolving the carbides back into the steel.

3.3.3 Addition of Molybdenum

A common austenitic stainless steel is 304SS and this relies heavily on the passive film due to a high content of Cr, ranging from 17.5% to 20% for grades 304, 304L and 304H. A similar stainless steel, 316, has slightly less Cr, slightly more Ni and 2-3% Mo, an element not present in 304 stainless steel.

Pure Mo has a BCC crystal structure, and it is a ferrite former. However, high proportions of austenite former such as Ni and N force 316 stainless steel to keep its FCC structure despite the addition of Mo. Adding it to austenitic steels improves their strength and resistance to creep at high temperatures.

Steels such as 316SS are known to have better corrosion resistance in chloride rich environments. Where at least 2% Mo has been added it improves resistance to pitting and crevice corrosion resistance [corrosionmo]. The mechanism by which Mo helps to protect against corrosion is still unclear. It is possible the addition helps to reduce the breakdown of the passive film protecting the steel, but it may also be the case that Mo promotes the repair of the passive film [moprotection].

3.4 Irradiation Assisted Stress Corrosion Cracking

Damage due to irradiation was first identified in high stress stainless steel components in a reactor, such as bolts, springs, and fuel elements [gswasiasscc] [iascckenikjonesbell], and later being found in lower stress austenitic stainless steel components [iascckenikjonesbell].

Irradiation of water causes the radiolysis of water, changing the chemistry of water and creating hydrogen, radicals and other ions that increase the corrosiveness of the environment (fig ??). The radiation also damages the material directly, changing its properties. A form of IASCC to which high nickel alloys, including austenitic steels, are particularly susceptible to is inter granular stress corrosion cracking.

3.5 Inter granular stress corrosion cracking

Stress corrosion cracking may be trans granular (through the grains) or inter granular, at the grain boundary. IGSCC is a particularly prominent failure mechanism for austenitic stainless steels. For IGSCC to occur, there must be a material that is susceptible to this form of cracking, an environment that is corrosive to the material as well as stress (fig. ??).

Stress may come from a high pressure environment or residual stresses due to welding. In a nuclear reactor the atomic structure may be under stress due to damage caused by neutrons passing through the steel, or due to the swelling of the steel on the macroscopic scale. If Cr is depleted at the grain boundary, protection to corrosion due to the passive layer is lost. This, coupled with the knowledge that austenitic stainless steels are susceptible to IGSCC, completes the three requirements and, over time, components of this material in these conditions will eventually fail to IGSCC.

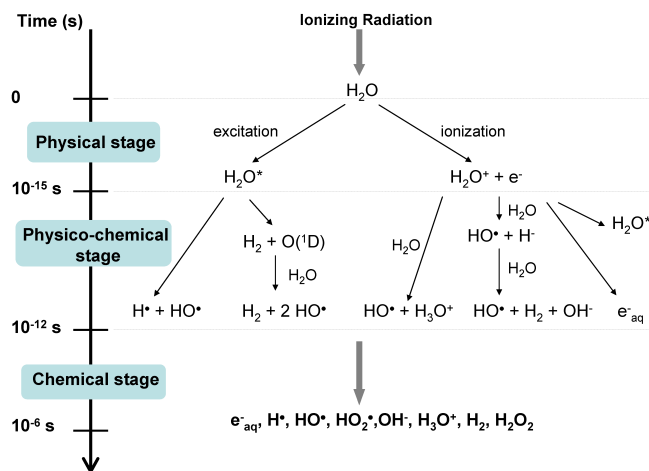


Figure 3.14: Changing water chemistry: radiolysis of water [waterradiolysis]



Figure 3.15: Three requirements for IGSCC to occur

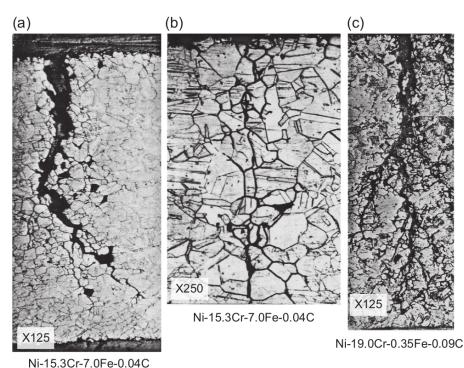


Figure 3.16: Inter Granular Stress Corrosion Cracking in Nickel Alloy[staehlecoriou]

IGSCC has not only been a defect in stainless steel. High Ni content alloys, such as Alloy 600 (Inconel: Ni-72, Cr-17, Fe-10), have been known to suffer from IGSCC since the very early days of nuclear energy, in particular with the prototype S1W reactor, prototype for the first nuclear powered submarine, the USS Nautilus.

After the war, there was a drive to develop a nuclear powered navy for the US. There are obvious benefits in replacing conventional power in vessels with nuclear, in particular for submarines. This was pushed by Admiral Rickover and the route to building the USS Nautilus began. A number of available Fe-Cr-Ni alloys were considered for the construction of the reactor (fig. ??).

Prototypes developed for the USS Nautilus experienced stress corrosion cracking in the Inconel Alloy 600 components. H. Coriou replicated this damage to Inconel in the laboratory, holding a sample at 620K in deoxygenated water for 3 months[staehlecoriou]. Further studies showed that IGSCC became a particular issue to alloys with a high Ni content in pure water, commencing with a content of approximately 70% Ni. In a weak salt water solution (0.1% NaCl) IGSCC occurred as with the same alloy in pure water, but TGS SCC occurred in similar alloys with a low Ni content (less than 15%) (fig. ??).

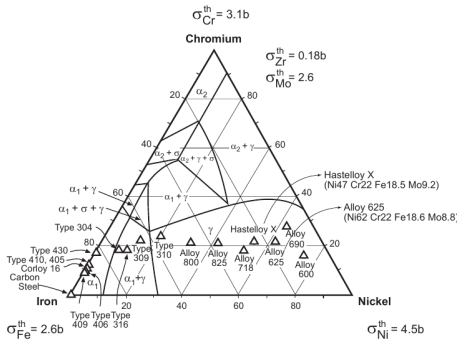


Figure 3.17: Alloy choices for early LWRs

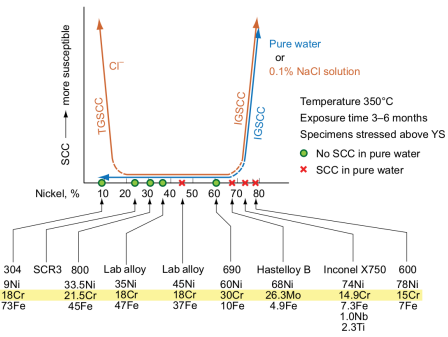


Figure 3.18: Nickel, IGSCC and TGS SCC

3.5.1 IGS SCC in Light Water Reactors

In LWRs a major factor in corrosion of components is the water chemistry and electrochemical corrosion potential that they operate in. Higher levels of oxygen dissolved in the water leads to an increase in the corrosion potential[wasstrucaustenitic]. Other factors within LWRs include depletion of Cr due to either heat treatment, welding or irradiation.

The primary circuit of a BWR includes components such as a reactor pressure vessel, piping that leads out of the containment building, fuel and fuel assembly. 300 series steels, including 304 and 316, are used within the primary circuit, including the piping and control rod absorbers. In BWRs the purity of the water has been addressed, and the addition of hydrogen to the water has reduced cracking of components[staehlecoriou].

Higher nickel content steels such as the 600 series alloys are used in PWRs, and components that are made from these alloys include steam generators and pressure vessels. In the AP-1000 design, the control rod drive mechanism at the reactor coolant pressure boundary are made from 304, 304L, 304LN, 316, 316L and 316LN steel. Higher nickel content 690 is used for penetration into the pressure vessel[ap1000dcd]. As illustrated by Coriou's work in the 1950s and 1960s, higher nickel content steels are susceptible to stress corrosion cracking.

3.5.2 IGS SCC and Advanced Gas-cooled Reactors

The first generation of nuclear reactors in the UK were Magnox type reactors. They used un enriched Uranium 0.7% U235 as fuel which was contained within magnesium oxide cladding due to its low absorption cross section. A major drawback was the relatively low operating temperature of 630K.

Carnot's theorem shows that the maximum amount of energy from an engine is dependent on the difference between the hot and cold reservoirs (section ??). The ambient temperature of the power station will vary a small amount with the seasons. The practical way to improve the maximum possible efficiency is to increase the engine (reactor) temperature.

$$\eta_{max} = 1 - \frac{T_c}{T_h} \text{ where the temperature is measured in absolute units} \quad (3.2)$$

AGR's were designed to run at much higher temperatures of 920K. By increasing the temperature, the maximum possible thermal efficiency was increased from just over 50 percent to almost 70 percent. To withstand higher temperatures, the magnesium oxide cladding used in the earlier Magnox reactors was replaced with stainless steel. To counteract the higher neutron absorption cross section of the cladding, the fuel was enriched up to 3.5% U²³⁵.

The cladding holds the fuel elements together and at the required location inside the reactor whilst it is consumed in the reactor. The cladding also performs several functions once the fuel has been spent. It holds the fuel elements together and acts as a primary containment for the spent fuel[[agrfuelstorage](#)].

During its lifetime as a fuel element within the reactor, the cladding has been heated and irradiated. By the process of RIS the Cr at the grain boundary can drop to 10% concentration[[agrigscc](#)]. The C rich environment within the reactor, due to the CO₂ coolant, provides yet another mechanism to deplete Cr at the grain boundary by the formation of Fe-Cr carbides (FeCr)₂₃C₆).

This loss of protection at the grain boundary, stress due to the role of the component within the reactor, the changing environment due to radiation damage and the material's susceptibility lead to IGSCC.

3.6 Austenitic Stainless Steels in Gen III+ and Gen IV Reactors

The AP1000 is an advanced PWR. As a Westinghouse reactor, the fuel cladding will be their trademarked Zirlo alloy. Inconel will be used for the steam generator and heat exchanger with carbon steel used for the construction of the pressure vessel. The control rod absorbers, however, will be constructed from 304SS[[ap1000mat](#)].

Areva designed the EPR and this will use 316SS as the fuel cladding material. It will also use the slightly less corrosion resistant 304SS (forged) in parts of the control rod drive mechanisms[[eprmat](#)].

The perforated upper core plate, between the reactor core and the inlet/outlet/control rod mechanisms, is also made from austenitic stainless steel. The pressuriser is constructed from ferritic steel, but its internals are clad with austenitic stainless steel to protect the structure from the coolant.

Gen IV designs also include the use of austenitic stainless steels. Experimental fast reactors in many countries, including the US, UK, Japan, France, India and China have used either 304SS, 316SS or both in their construction.

Austenitic steels are more corrosion resistant than ferritic or martensitic steels. They do expand more as a result of being irradiated, but they are stronger at higher temperatures. Many of the Gen IV reactors operate at much higher temperatures than existing reactors and the components will be expected to resist higher doses of radiation damage throughout their lifetime.

GFRs are expected to use austenitic steels. Due to their chemical compatibility with sodium they are also expected to be used in SFRs. As well as being used in the reactor core, these steels will also be used outside the core. For example, SFRs in France will use austenitic steels in the secondary circuit, primary pump, internal heat exchanger and more[[convsteelooc](#)].

3.7 The Addition of Platinum group metals to Stainless Steel

Water purity is a concern for light water reactors. The fewer contaminants there are to begin with, the better. Even so, the radiolysis of the purest water will still create a steady supply of corrosive molecules (fig. ??). Adding hydrogen to the water reduces the electrochemical corrosion potential of the water, but if too much is added it will combine with the radioactive nitrogen-16 created by the $^{16}O(n,p)^{16}N$ reaction to form $^{16}NH_3$ [[noblemetalchemical](#)].

Cathodic modification is a technique used to improve corrosion resistance, and one way to do this for stainless steel is to add small amounts of PGMs[[potgieter1994](#)]. By adding such metals, the anodic reaction may be reduced. PGMs also act as a catalyst in the reduction and removal of O₂ and H₂O₂ from the water[[noblemetalchemical](#)].

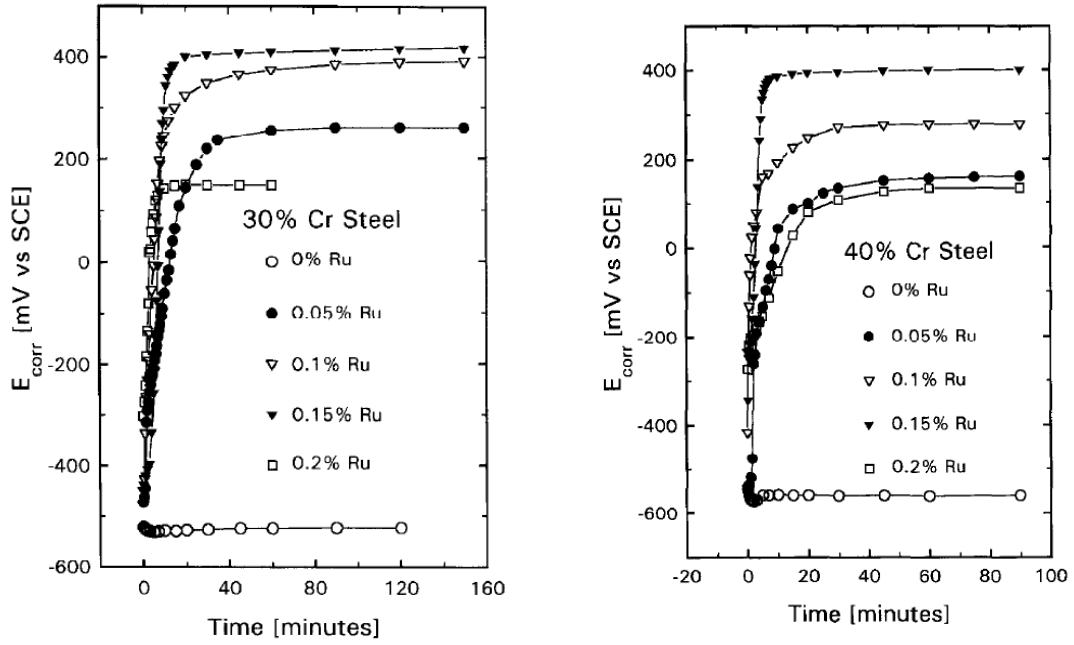


Figure 3.19: Addition of Ru to Fe30Cr and Fe40Cr steels - open current corrosion potential variation with time in 10% sulphuric acid [potgieter1994]

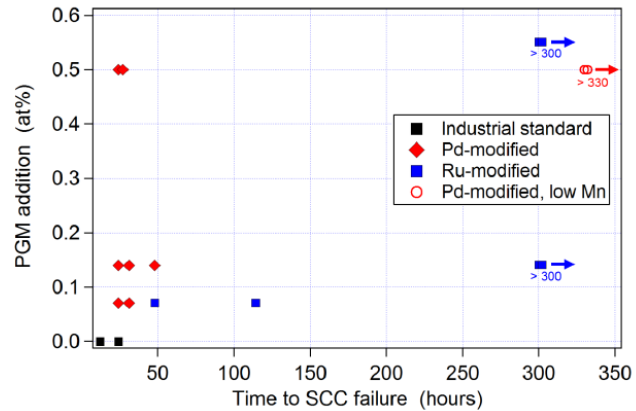


Figure 3.20: Failure times for 304SS, Pd doped 304SS (with and without Mn) and Ru doped 304SS in polythionic acid at ambient temperature [scrstainless]

The increased corrosion resistance is dependant upon the amount of PGM added, but a higher percentage does not necessarily mean better protection. This is important for two reasons, to find the optimum amount for the sake of corrosion resistance, and to keep the price down as the additions are so expensive, even in such small amounts.

It was found that an addition of 0.15% Ru (out of a selection of 0%, 0.05%, 0.10%, 0.15% and 0.20%) was optimum for both Fe30Cr and Fe40Cr steel (fig. ??)[potgieter1994]. Other PGMs may be used for cathodic modification, including Pd, Ir and Pt, but the cost of the metal must be weighed against the possible gains.

Connolly et al recently added Ru and Pd to 304SS samples that were sensitized at 920K for 24 hours [scrstainless]. After sensitization, the steel was analysed by TEM and Cr-rich carbides were found at grain boundaries. Without the passive protection due to Cr, the samples were exposed to polythionic acid to promote SCC. The Ru doped steels performed well, but the Pd doped steels showed no improvement over regular 304SS. Further analysis of the samples by TEM reveals that the low percentage of Mn in the steel allows the formation of Pd-Mn precipitates at the grain boundary [scrstainless]. These precipitates form during the sensitization procedure

and thus negate the protection by cathodic modification at the surface of the metal by removing the Pd.

With a low Mn 304SS (less than 0.05% Mn), varied amounts of Pd have been tested. With the reduction in Mn the corrosion resistance improves greatly over regular 304SS. Palladium remains at the surface, as the amount of Mn is too low for appreciable amounts of Pd to be lost to precipitate formation during sensitization. No failures have been observed with either the Ru or Pd (low Mn) samples for 330 hours exposure to polythionic acid at ambient temperatures (fig. ??) [scrstainless].

The surface of the metal does not need to have a full coating of PGM but it should be equally spaced across the surface. Oxidant in the layer at the surface will be consumed at the locations of PGMs and the change in concentration at those points will naturally cause diffusion of more oxidant to those locations[noblemetalchemical].

The PGMs may be coated on the surface of the metal or alloyed to the metal. The first method is the more cost efficient but if a crack does form, or if a layer is removed, it will expose the regular alloy underneath. If the PGM is alloyed, there will always be protection, unless a mechanism is removing the PGM from the surface. This could be through precipitation as a carbide, or it could be due to radiation causing the metals to segregate.

Reaction	Product Halflife
$^{54}Cr(n, \gamma)^{55}Cr$	3.5 mins
$^{64}Ni(n, \gamma)^{65}Ni$	2.5 hrs
$^{55}Mn(n, \gamma)^{55}Mn$	2.6 hrs
$^{104}Ru(n, \gamma)^{105}Ru$	4.4 hrs
$^{108}Pd(n, \gamma)^{109}Pd$	13.7 hrs
$^{196}Pt(n, \gamma)^{197}Pt$	19.9 hrs

Table 3.2: Radioactive products and their half lives for PGM doped 304SS

Adding elements to metals, even in small amounts, may be problematic as certain elements have high neutron reaction cross sections and transmute into radioactive isotopes. ^{55}Cr is a concern for all neutron irradiated stainless steels, but with a very short half life it quickly cools and becomes less of a concern, with ^{65}Ni becoming the dominant source of activity after 10 hours. Adding Mn to steel that is in a reactor is known to result in an increase in activity due to the $^{55}Mn(n, \gamma)^{56}Mn$ reaction (section ??).

The addition of PGMs alters the activity of the steel following neutron irradiation and with just a 1% addition there is an increase in activity comparable to that of the 10% Ni transmuted to ^{65}Ni . This is due to reactions that create ^{105}Ru , ^{109}Pd and ^{197}Pt for Ru, Pd and Pt respectively (table ??).

With such small additions required for cathodic modification and the short half lives of the radioactive isotopes, there isn't a concern due to neutron activation over regular 304SS, and much less of a concern than that of 304SS containing Mn. More data computed using the TENDL library is available in appendix ??.

Chapter 4

Background: Proton Activation and Radioactive Decay

Where proton or deuteron radiation is used to emulate neutron damage, there is still an associated risk of transmuting atoms in the target material, creating radioactive isotopes. An equation was derived to calculate the radioactivity of each element in the decay chain. It takes into account a source term for each isotope in the decay chain, as well as any branching factors.

Once derived, the equation was used in a computer code that, coupled with cross section data from the TENDL library and ion transport data from the SRIM ion transport code, predicts the radioactivity of a sample (chapter ??).

4.1 Ion Sources

4.1.1 LINAC

Since the development of the first linear accelerator (LINAC) in the 1940s, their modern day versions have become some of the most powerful accelerators in the world. The longest LINAC, Stanford Linear Accelerator Center, is 3.2km in length and it accelerates electrons and positrons at energies of up to 50GeV. Several LINACs for protons include the 800MeV LINAC component of the ISIS neutron source in Oxfordshire, and the 800MeV LINAC used by the Spallation Neutron Source at Oak Ridge National Laboratory.

The accelerator is constructed of several tubes, connected alternately to opposite terminals of a high frequency alternating current supply. As protons enter the first tube, a negative voltage is applied. As the protons reach the gap between the first and second tube, the polarity is reversed. The positive charge that is now applied to the first tube pushes the protons forward as the negative charge on the second tube pulls the protons forward. This process is repeated along the length of the accelerator, with the sections increasing in length due to the increase in velocity of the protons.

4.1.2 Cyclotron

Cyclotrons are reasonably compact and cost effective. The largest current cyclotron, TRI-University Meson Facility, is located in Canada and is able to output protons with energies over 500MeV. It is relatively large, weighing 170 tons. There are approximately 350 cyclotrons[cyclotrons] around the world today.

The University of Birmingham cyclotron is more compact. The protons it accelerates are in the 8-40MeV range and the projectiles are not just restricted to protons (table ??).

Projectile	Energy (MeV)	Maximum Current (micro A)
proton	8-40	60
deuteron	8-40	30
He^{2+}	8-53	30

Table 4.1: University of Birmingham Cyclotron Ion Beams

The moderate size, energy range, availability and cost of these Cyclotrons make them ideal candidates for damaging targets with light ions, rather than neutrons from a neutron source.

The Scanditronix MC40 is an isochronous cyclotron. As the ions are accelerated to higher and higher velocities, the effects of special relativity become appreciable.

$$v = c \sqrt{1 - \frac{{E_{rest}}^2}{{E_V}^2}} \quad (4.1)$$

The cyclotron has two Dees and these are D shaped hollow electrodes. Ions enter at the center of the cyclotron and are held in the Dees as they are accelerated. The magnetic field is varied to bend the path of the ions from a circle into a round cornered triangle.

4.1.3 Synchrotron

Two of the most well known accelerators are Synchrotrons: the Large Hadron Collider at Conseil Europen pour la Recherche Nuclaire, and the now retired Tevatron at Fermilab. These are typically large machines and there are approximately 70 around the world [[synchrotrons](#)], approximately a fifth the number of Cyclotrons.

Synchrotrons are used for storing high energy particles in a continuous loop, either to generate light through magnetobremssstrahlung, or for high energy collisions. Cyclotrons are more commonly used for lower energy (tens of MeV) projectiles, in materials science for damaging materials and for medical use (creating radioactive isotopes for use in hospitals).

4.2 Neutron Sources

4.2.1 High-Flux Neutron Reactors

There are 250 or so research reactors in 55 countries [[researchreactorstats](#)], and a number of these are used for materials research. In the UK, there is only one remaining research reactor, and this is the Neptune pool type reactor at Rolls Royce [[neptunereactor](#)]. In Cadarache, France, the Jules Horowitz reactor is under construction and this is being built specifically as a materials testing reactor. It will be crucial in researching new materials for use in upcomming Gen IV nuclear power stations [[researchreactorstats](#)].

High Flux Isotope Reactor, Oak Ridge

The High Flux Isotope Reactor, at the Oak Ridge National Laboratory in America, is an 85MW research reactor that provides testing space within the reactor as well as a number of neutron beam lines. The reactor uses

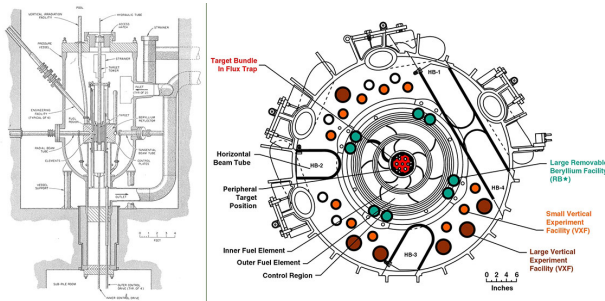


Figure 4.1: A cross section of the HFIR [hfirornl]

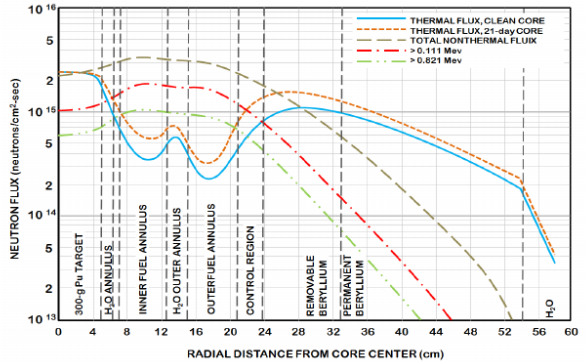


Figure 4.2: Neutron Flux in the HFIR while at 85MW
/hfiruserguide]

highly enriched Uranium as its fuel source and is scheduled to operate at 100% capacity for 161 days per year, in cycles of approximately 23 days. A 30cm surround of Beryllium is used to reflect neutrons, and in the reactor core there is a high flux of thermal neutrons at a rate of 2.3×10^{15} neutrons $\text{cm}^{-2}\text{s}^{-1}$ [hfirornluserguide].

NIST Center for Neutron Research

The National Bureau of Standards Reactor (fig. ??) was designed as a research reactor with a power output of 40MW and a neutron flux of approximately 1.0×10^{15} neutrons $\text{cm}^{-2}\text{s}^{-1}$. It uses highly enriched Uranium as fuel and is both moderated and cooled by heavy water.

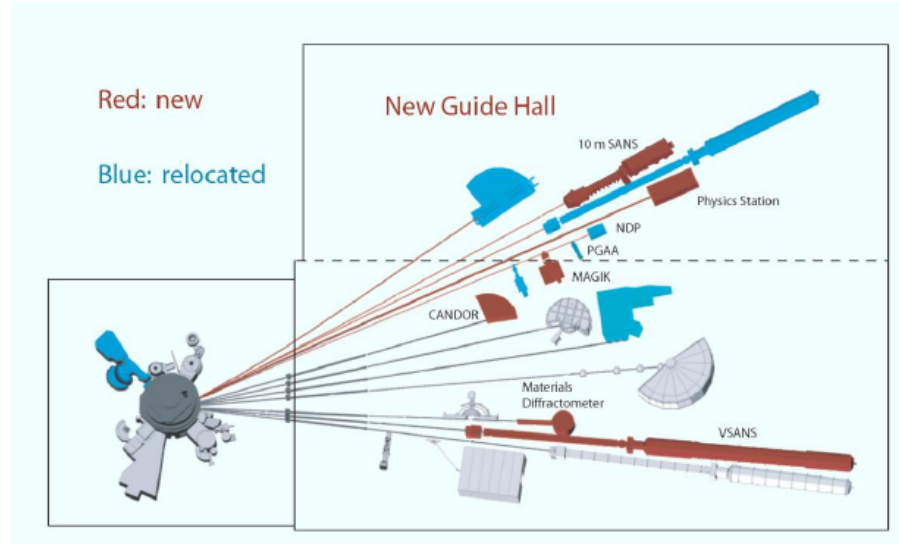


Figure 4.3: NBSR building layout[nbsrhistory]

4.2.2 Spallation

Neutrons cause fission in nuclear reactors, but spallation sources require protons and high mass targets. The energy of the protons required is a magnitude greater than that of the Scanditronix MC-40 Cyclotron at the University of Birmingham, with spallation source accelerators having a range from 500MeV to over 1GeV.

ISIS is a neutron spallation source located in Harwell, Oxford. Protons are accelerated in a LINAC to 0.37c before being fed into a 163m circumference synchrotron. The protons are then accelerated to 0.84c before being projected, in bunches, at a tungsten target. The impact with the tungsten releases neutrons[isisneutronsource].

Oak Ridge National Laboratory also has a neutron spallation source, the SNS. A LINAC accelerates a negatively charged proton (a hydrogen atom with two electrons) up to just below 0.9c. It is stripped of the electrons and enters an accumulation ring as a proton. More protons are accumulated until the beam in the accumulator is diverted at a mercury target. The collision between the mercury target and the protons releases approximately 20 neutrons per collision, and these neutrons pass through beam lines to the experiments.

The source creates a pulse of neutrons from the 50 ton mercury target 60 times per second. The protons are accelerated by the LINAC to between 2.5MeV and 1.0GeV and this results in neutrons with energies almost as high as the proton projectiles. A spectrum of neutron energies is produced with each pulse, although the neutrons may be moderated at the end of the beam lines to slow the neutrons down.

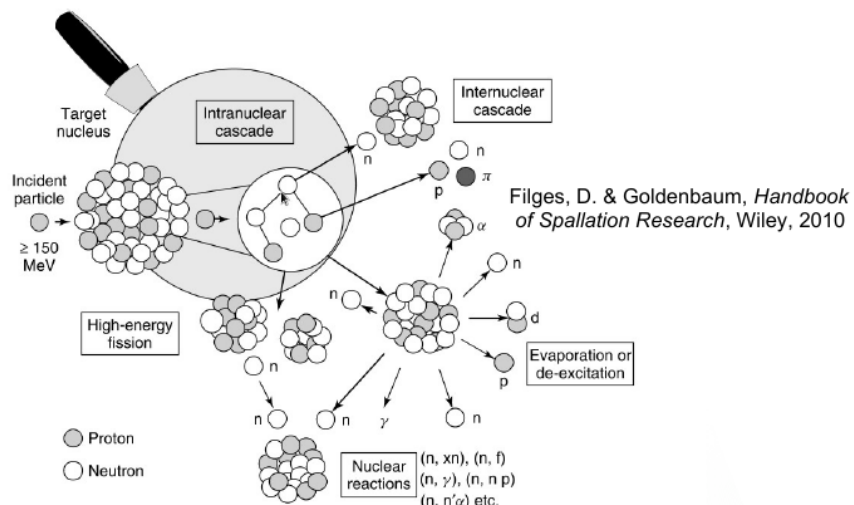


Figure 4.4: An example of a neutron spallation source where high energy ions collide with heavy atoms [spallationsource]

4.3 Source Review

Source	Cost	Projectile	Flux/Current	Energy
Scanditronix MC-40	1 million	Proton	3.7×10^{14}	8-40MeV
HFIR[hfiruserguide]		Neutron	3.0×10^{15}	Full Spectrum
HFIR[hfiruserguide]		Thermal Neutron	Over 2.0×10^{15}	Thermal
HFIR[hfiruserguide]		Fast Neutron	2.0×10^{15}	> 0.111MeV
HFIR[hfiruserguide]		Fast Neutron	1.0×10^{15}	> 0.821MeV
SNS[spallationsourceflux]	\$1.4 billion	Neutron	Average 1.2×10^{13}	Full Spectrum
ISIS spallation source[spallationsourceflux]		Neutron	Average 4.0×10^{13}	Full Spectrum

Table 4.2: Examples of neutron sources, energies and flux, with the MC-40 as a reference for protons

The compact proton source that is the cyclotron is compared to neutron sources. It is much smaller and cheaper in comparison and the energy of the projectile may be controlled, whereas a spectrum of energies of neutrons is produced by reactors and spallation sources. Faster neutrons will cause more damage to materials in Gen IV reactors giving the cyclotron an advantage, being able to focus in just one energy range. The three mentioned isotope sources are national facilities that cost much more than a cyclotron. Access is shared between many researchers whereas a cyclotron, such as the Scanditronix MC-40 at the University of Birmingham may have a beam dedicated to a particular task.

4.4 Ion Irradiation to Investigate Neutron Damage

Neutrons emitted during the fission of Uranium-235 have an energy spectra in the intermediate to fast range, with a peak at 1MeV, and a large proportion in the 1MeV to 10MeV range (fig. ??). The higher energy neutrons are more of a concern to this work as higher energy neutrons, on colliding with atoms within the target material, cause large damage cascades.

As discussed earlier in this chapter, there are a number of methods available to create both high energy neutrons and ions, but each has its own set of advantages and disadvantages. At the University of Birmingham high energy ions are created using a cyclotron.

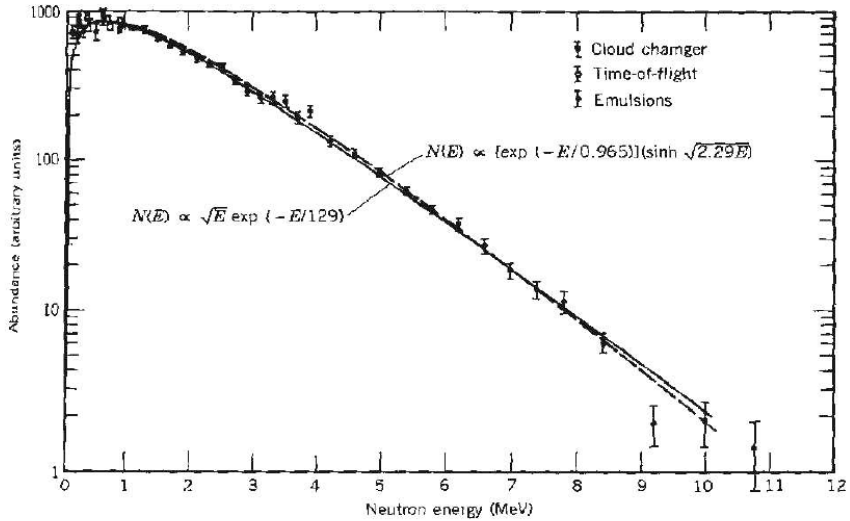


Figure 4.5: Neutron Spectra from the Fission of U235[leachmanneutrons]

4.4.1 Ion Irradiation at the University of Birmingham

The Scanditronix MC-40 Cyclotron is used at the University of Birmingham to create a beam of protons or other light ions. The energies of these ions are typically between 10 MeV and 60 MeV with beam currents ranging up to 50 microamps (3.1×10^{14} protons per second). Target materials are irradiated by this cyclotron for a number of reasons, including purposely creating radioactive isotopes for the nearby Queen Elizabeth Hospital, investigating ion irradiation damage and emulating neutron irradiation.

The Cyclotron is usually used to create radioactive isotopes for medical use, but an additional beam line has been devoted to material science investigations into radiation damage. While the creation of radioactive isotopes is desired in some cases, material being tested for radiation damage should preferably have low levels of radioactivity.

It is expensive to arrange the irradiation of target materials by high energy neutrons sources, whereas it is relatively inexpensive to irradiate using an ion beam on the MC-40 Cyclotron. The energies can be controlled, and a set dose at a single energy, or a range of energies, can be precisely deposited into the target material. The reaction cross section for neutrons also cover a much larger range including lower energy projectiles, something Coulomb repulsion reduces for ions (fig. ??).

The Activity code discussed in this work was developed to calculate the activity of a target material irradiated

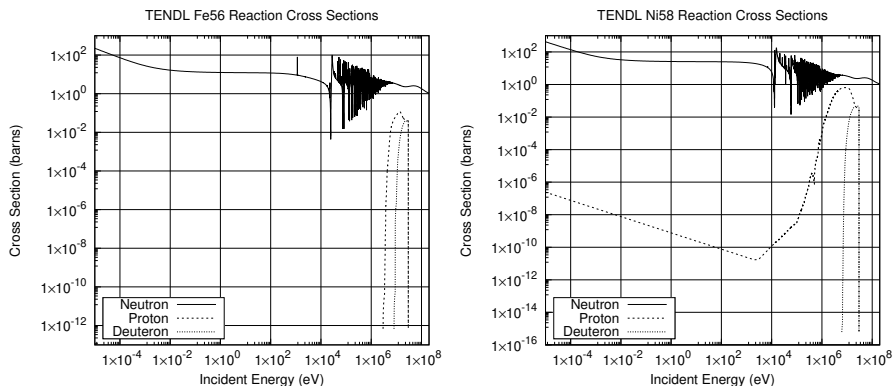


Figure 4.6: Neutron, proton and deuteron cross sections for Fe56 and Ni58

by a proton beam. It has been developed in Fortran and uses data from the TENDL-2013 proton cross section database, SRIM ion transport code and Nuclear Data Services radioactive decay database. A second version was also developed using Python and a more recent TENDL database.

4.4.2 Transmutation of Nuclei by Neutrons and Protons

Neutron Activation

The fission of Uranium-235 atoms results in neutrons with a varied spectrum of energies. The neutrons will bounce around inside the reactor losing energy quickly to light atoms within moderators and coolants, such as water. At lower energies the neutrons may be captured by the nuclei of atoms they interact with. This creates a new isotope which may or may not be stable.

Proton Activation

Considering a simplified nuclear potential well, energetic protons approaching a nucleus may overcome the Coulomb potential barrier. They are captured by the nucleus and held within the potential well by the strong nuclear force. This process may leave the nucleus in an excited and unstable state, depending on the input energy of the proton and configuration of nucleons. The process is probabilistic, and the average chance of a reaction (the microscopic cross section) may be measured as a function of the projectile, projectile energy and target, either experimentally or by optical model potential calculations. The reaction rate is calculated from the microscopic cross section using the following equation:

$$R = \frac{J}{Q} \cdot n_p \cdot \sigma \cdot 10^{-28} \delta t \quad (4.2)$$

- R Reaction Rate (reactions per second)
- J Beam current (A)
- n_p Number density of target (atoms per cubic metre)
- σ microscopic reaction cross section (barns)
- Q projectile charge e.g $1.602177 \times 10^{-19} C$ for a proton
- δt target thickness (m)

4.4.3 Nuclear Reaction Cross Sections

Reaction Cross Sections

The type of reaction for an individual reaction cannot be determined, but the probability of that reaction happening may be measured and future events predicted. This data may be gathered experimentally, or it may be calculated using various models.

TALYS and the Optical Model Potential

In the standard model, protons and neutrons are composed of quarks, held together by the strong nuclear force. The nucleus of an atom is also held together by the strong nuclear force that on such small separations overwhelms the electromagnetic force of the protons with one another.

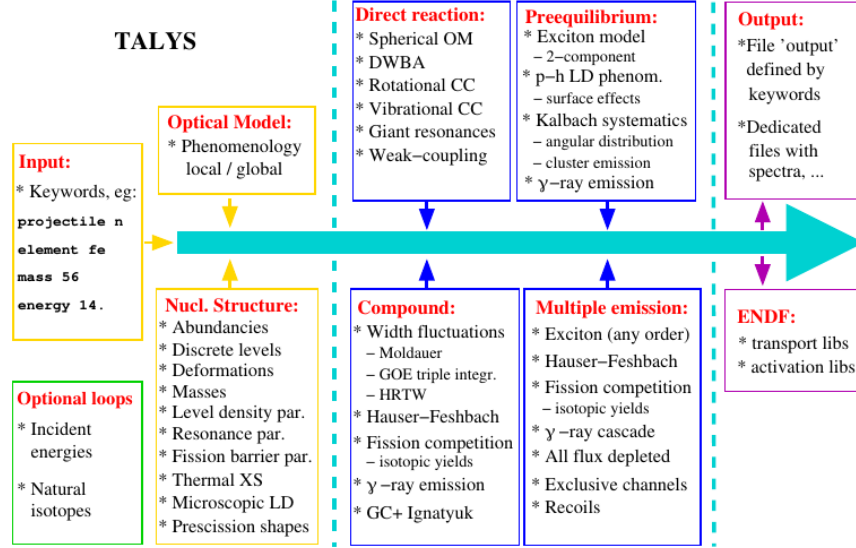


Figure 4.7: TALYS work flow [talsysmanual]

This is a complicated system, not to mention the excited states that nuclei may occupy. The interaction of a projectile (proton, neutron or a heavier ion) with the nucleus is a challenge to model.

Initially, reaction data for protons and neutrons were gathered through experimentation. In the 1950s, Feshbach et al put forward a simple model for nuclear reactions between the nucleus and neutrons, and this model was restricted to 0-20MeV neutrons. The form of the potential used was a complex function[hodgson1].

$$\begin{aligned} V &= V_0(1 + i\zeta)r < R \\ V &= 0r > R \end{aligned} \tag{4.3}$$

The potential in equation ?? has the parameters $R = 1.4 \times A^{\frac{1}{3}}$, $V_0 = 42\text{MeV}$ and $\zeta = 0.03$ where A is the atomic mass of the target atom.

Considering the complexity of the system being modelled, this simple model was very successful. Over the years since, the models used have become more complex and parameters used have been fit to an increasing amount of experimental data.

The Talys code uses a range of models (figure ??). These include the optical model which is solved using the Equations Couples Itrations Squentielle (ECIS-06) code of Jacques Raynal, implemented as a subroutine within Talys, and this is accurate up to 180MeV[talsysmanual]. Whilst the Talys code has been extended up to 1GeV, it is experimental in the 180MeV to 1GeV range. Fortunately, this work only requires nuclear reaction cross section data up to approximately 100MeV as the current ion source under consideration produced ions with energies up to 60MeV.

The Talys code has potentials for protons and neutrons, but it also has potentials for deuterons, tritons, helium-3 and alpha particles. The potentials are discussed in detail in the Talys manual[talsysmanual]. This extension to heavier ions may be useful for this work as the University of Birmingham cyclotron is capable of accelerating deuterons and He^{2+} ions.

Comparing experimental data to the Talys data for $Fe54(p, \gamma)Co55$ shows good agreement between 1MeV and 10MeV?. There was insufficient experimental data from this source, but the Talys generated data ranges from

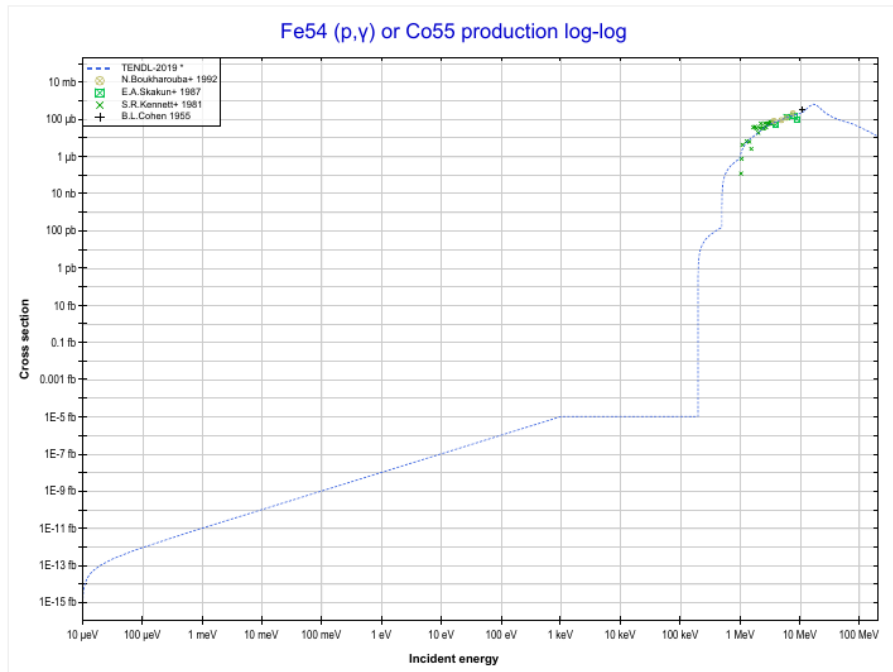


Figure 4.8: TALYS Fe54-Co55 cross section comparison with experiment [tendlfeco]

micro eV up to 100MeV+ (fig. ??).

PADF

The Proton Activation Data File was released in 2007 and contained nuclear reaction data for 2355 target nuclei, ranging from Magnesium (12) to Radon (86) with proton energies up to 150MeV. The file contains the sum of all individual reactions as well as certain yields, and the data was generated using the TALYS and ALICE/ASH codes, as well as experimental data from Exfor[[exforlink](#)].

Listing 4.1: A sample of the Iron-56 PADF data file

```
1 Proton Activation Data File          528 1451 12
2 ****
3
4 Authors: C.H.M.Broeders, U.Fischer, A.Yu.Konobeyev, L.Mercatali 528 1451 15
5
6
7 Data for PADF file were obtained using the TALYS code [1] for 528 1451 18
8 target nuclei with half-life more than 10 min and using the 528 1451 19
9 ALICE/ASH code [2] for nuclei with 1 sec < T1/2 < 10 min and 528 1451 20
10 available experimental data        528 1451 21
11 MAT numbers are taken according to JEFF-3.1/RDD      528 1451 22
12
13 Evaluation for Fe-56 (stable) : TALYS code           528 1451 24
14 Experimental data used for the correction of calculated 528 1451 25
15 excitation functions are taken from Refs.[3-12]       528 1451 26
16
17
18 File contains                      528 1451 28
19
20 MF=3 MT=5                          528 1451 30
21 Sum of all individual reaction cross-sections (Total 528 1451 32
22 reaction cross-section)           528 1451 33
23
24 MF=6 MT=5                          528 1451 34
25 Yields of nuclei in nuclear reactions including 528 1451 35
26 n, p, d, t, He-3, He-4 and photon production 528 1451 37
```

TENDL 2019 Data Files

The cross section data for protons and neutrons is available to download in ENDF format files. The data files used by this work are TENDL data files, and these are created by a combination of different nuclear models and experimental data. The TENDL nuclear reaction simulation code provides the calculated data.

The nuclear reaction files are rather large, and they all follow a standard format.

Listing 4.2: Sample TENDL File

```
1 2.605600+4 5.545443+1      0      0      0      02631 3 2   1
2 0.000000+0 0.000000+0      0      0      1      462631 3 2   2
3     46      2
4 1.000000+3-9.920042-7 1.000000+6-9.920042-7 2.000000+6-2.167241-42631 3 2 4
5 3.000000+6-7.609736-3 4.000000+6-3.232345-2 5.000000+6-5.975554-22631 3 2 5
6 6.000000+6-5.149510-2 7.000000+6-3.685484-2 8.000000+6-5.542173-22631 3 2 6
7 9.000000+6-9.978765-2 1.000000+7-1.599116-1 1.100000+7-2.206871-12631 3 2 7
8 1.200000+7-2.743084-1 1.300000+7-3.165007-1 1.400000+7-3.471231-12631 3 2 8
9 1.500000+7-3.674350-1 1.600000+7-3.788282-1 1.700000+7-3.825634-12631 3 2 9
10 1.800000+7-3.799978-1 1.900000+7-3.725944-1 2.000000+7-3.617662-12631 3 2 10
11 2.200000+7-3.342054-1 2.400000+7-3.031296-1 2.600000+7-2.709398-12631 3 2 11
12 2.800000+7-2.388019-1 3.000000+7-2.077513-1 3.500000+7-1.398614-12631 3 2 12
13 4.000000+7-8.801994-2 4.500000+7-5.013441-2 5.000000+7-2.349373-22631 3 2 13
14 5.500000+7-5.480233-3 6.000000+7 6.189980-3 6.500000+7 1.332313-22631 3 2 14
```

```

15  7.000000+7 1.727774-2 7.500000+7 1.906833-2 8.000000+7 1.943711-22631 3 2 15
16  9.000000+7 1.783081-2 1.000000+8 1.499871-2 1.100000+8 1.211197-22631 3 2 16
17  1.200000+8 9.641120-3 1.300000+8 7.717424-3 1.400000+8 6.318436-32631 3 2 17
18  1.500000+8 5.367555-3 1.600000+8 4.771939-3 1.800000+8 4.312985-32631 3 2 18
19  2.000000+8 4.445323-3                               2631 3 2 19

```

4.4.4 Radioactive Decay

Radioactive decay is the random change in nucleons or energy state of an unstable nucleus. It is impossible to predict when a single nucleus will decay, but the decay of a collection of nuclei is statistical in nature. The radioactivity and number of unstable nuclei at time t can be predicted using the decay constant, λ , for the radioactive isotope. This constant is defined as follows:

$$\lambda = -\frac{N'(t)}{N(t)} \quad (4.4)$$

The number of radioactive nuclei $N(t)$ at time t is given by the following equation, where $N(0)$ is the starting number of nuclei:

$$N(t) = N(0) \exp(-t\lambda) \quad (4.5)$$

The activity $A(t)$ of the radioactive nuclei is predicted at time t by using the following equations, where $N'(t)$ is the change in amount of nuclei with respect to time:

$$A(t) = -N'(t) = \lambda N(t) \quad (4.6)$$

$$A(t) = \lambda N(0) \exp(-t\lambda) \quad (4.7)$$

4.4.5 Saturation Activity

As a radioactive isotope is created by reactions between target atoms and projectiles (protons, neutrons, deuterons) it will begin to decay. The amount of the isotope will continue to increase until the decay rate equals the reaction rate for the creation of the isotope.

For a single isotope:

$$\frac{dN}{dt} = \frac{J}{Q} \cdot n_\rho \cdot \sigma \cdot 10^{-28} \delta t - \lambda N \quad (4.8)$$

$$N(t) = \frac{\frac{J}{Q} \cdot n_\rho \cdot \sigma \cdot 10^{-28} \delta t}{\lambda} (1 - \exp(-\lambda t)) \quad (4.9)$$

The saturation time for a given percentage may then be calculated directly from the decay constant.

$$t = \frac{\ln(1 - (p/100))}{-\lambda} \text{ where } p \text{ is the saturation percentage} \quad (4.10)$$

4.4.6 Decay Constants: Joint Evaluated Fission and Fusion File (JEFF) 3.3 Data File

JEFF 3.3 is an evaluated data file[jeff311], meaning it has been evaluated by a relevant authority. The quality of the data may affect the health of the public and industry workers, so it must be evaluated. This particular

file is managed by and available through the Nuclear Energy Agency (NEA).

It is a collection of many data files. Released in 2017, it also contains several files for incident gammas, protons, deuterons, tritons, helium-3 and alphas from the TENDL 2017 data file.

The files that will be important for this work are the ENDF-6 radioactive decay data files only. The nuclear reaction cross section data will come from Talys and various iterations of the TENDL libraries. The decay data held in the JEFF 3.3 file includes isotope data, masses, half lives, branching factors, continuous and discrete gamma data.

4.4.7 Bateman Equation for Radioactive Decay

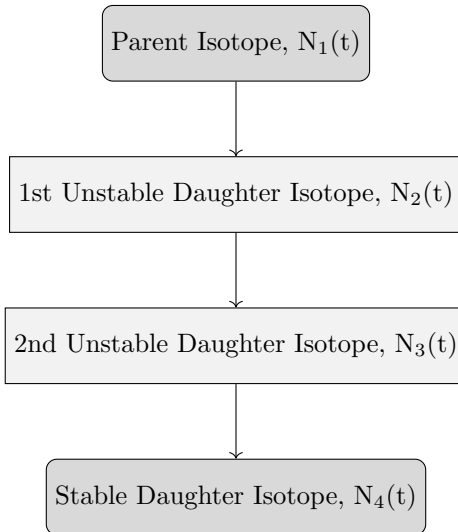


Figure 4.9: An example decay chain from an unstable parent isotope, through unstable daughter isotopes ending with a stable daughter isotope.

The English mathematician Harry Bateman derived an equation (eq. ??) to calculate the amount of each isotope in a decay chain, illustrated in Figure ??, at time t.

$$N_n(t) = \sum_{i=1}^{i=n} \left(\left(\prod_{j=i}^{j=n-1} \lambda_{(ij+1)} \right) \sum_{j=i}^{j=n} \left(\frac{N_{i0} \exp(-\lambda_j t)}{\prod_{p=i, p \neq j}^{p=n} (\lambda_p - \lambda_j)} \right) \right) \quad (4.11)$$

When a radioactive isotope decays, there may be more than one mode of decay, and this leads to branching factors. Pb-214 only decays via beta decay to Bi-214, giving a branching factor of 1.0, whereas Bi-214 has a 99.979% chance of decaying to Po-214 by beta decay and a 0.021% of emitting an alpha particle and decaying to Tl-210 (branching factors of 0.99979 and 0.00021 respectively) [jeff311].

When a target material is irradiated, there is a source term for transmuted nuclei due to the irradiation. The daughter isotopes of these transmuted isotopes will also be affected by the irradiation and will transmute further, giving a source term for each daughter isotope as a result of the irradiation. Sources for each isotope in the decay chain, and branching factors between a parent isotope and its daughter isotope/s must be accounted for.

4.5 Simulating Ion Irradiation with SRIM and TRIM

A package of ion transport codes, SRIM, is freely available to download and use to investigate the transport of ions through matter. It includes tools to calculate the stopping range of a given ion in a material as well as TRansport In Matter, a code used to calculate the energy and position of an ion through a target.

TRIM does not take into account the structure of a target. It may be layered in the calculation perpendicular to the beam, but beyond that the target is treated as amorphous. It will give the same result for BCC iron as it would for FCC iron, providing the density remains the same. The density and whether or not the target layer is a gas or solid are options that must be configured when setting up a calculation. Each ion history is tracked through the same target; the target never changes. TRIM is ignorant to the structure and therefore damage to the structure that would accumulate over time, and to any swelling and change in composition or density.

The interaction of the ion with the target material is split into two parts: nuclear loss and electronic loss. The ion is tracked through the target until either its energy drops below a set threshold (10eV) or it leaves the target (fig ??). The code then moves on to the next ion history.

In a projectile-nucleon interaction, the magic formula (eq. ??)[**srimbook**] is used to determine the scattering angle Θ of the ion and target nucleus, as well as the amount of energy transferred. The azimuthal angle is selected randomly by multiplying 2π by a random float [0.0, 1.0].

$$\begin{aligned}
 \cos\left(\frac{\Theta}{2}\right) &= \frac{B + R_c + \Delta}{R_0 + R_C} \\
 B &= \frac{p}{a} \\
 R_0 &= \frac{r_0}{a} \\
 R_C &= \frac{\rho}{a} \\
 \Delta &= A \frac{R_0 - B}{1 + G} \\
 A &= 2\alpha\epsilon B^\beta \\
 G &= \gamma \left((1 + A^2)^{\frac{1}{2}} - A \right)^{-1} \\
 \alpha &= 1 + C_1\epsilon^{-\frac{1}{2}} \\
 \beta &= \frac{C_2 + \epsilon^{\frac{1}{2}}}{C_3 + \epsilon^{\frac{1}{2}}} \\
 \gamma &= \frac{C_4 + \epsilon^{\frac{1}{2}}}{C_5 + \epsilon^{\frac{1}{2}}}
 \end{aligned} \tag{4.12}$$

where p is the impact parameter

where a is the screening length

where r_0 is the distance of closest approach

where ϵ is the reduced energy

The potential between the projectile and target is calculated at the distance of closest approach, r_0 . It is a Coulomb type potential (eq. ??) than includes the universal screening function (eq. ??). This potential will appear again, although occasionally with differing parameters, in chapter ??.

$$V(R) = \frac{Z_1 Z_2 e^2}{a R} \Phi(R) \tag{4.13}$$

$$\Phi(R) = 0.1818 \exp(-3.2x) + 0.5099 \exp(-0.9423x) + 0.2802 \exp(-0.4028x) + 0.2817 \exp(-0.2016x) \tag{4.14}$$

The recoil nuclei are also followed through several generations until their energies fall below that set for either the surface binding energy or displacement energy (3-6eV and 15-30eV respectively)[**srimbook**].

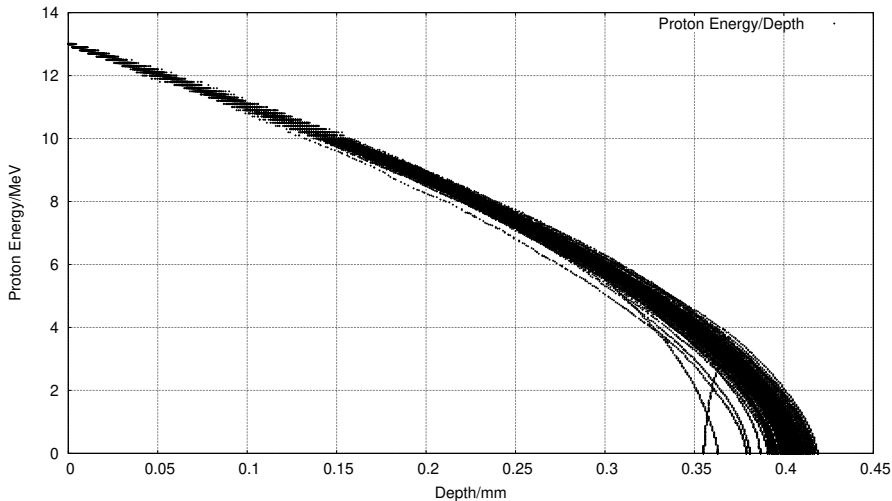


Figure 4.10: One hundred simulated 13MeV proton energy loss curves in Fe simulated with SRIM [srim]

The free flight path between large collisions is calculated based on the projectile energy, type and the target material. The path length between collisions is randomly generated by taking the maximum free path and multiplying by a random float [0.0, 1.0]. Smaller projectile-nucleus interactions are not individually calculated, but the average energy that would have been lost is calculated and applied.

The ion continuously loses energy to the electrons in the material. TRIM calculates this over the free flight path, L (eq. ??).

$$\Delta E_e = L N S_e(E) \quad (4.15)$$

where $S_e(E)$ is the electronic stopping
and N is the atomic density of the target

The target damage is a combination of the incoming ion, the primary knock on atoms and their damage cascades. The user has the option of running a full damage cascade that plots the entire cascade, or a quicker calculation where the cascade is treated as just a point. The total number of displacements is the sum of vacancies and replacement collisions, and the vacancies is sum of interstitials with the number of atoms that leave the target.

One file that SRIM creates is of importance to the Activity code, and that is the trajectory file that contains the energy and x,y,z co-ordinate data points for simulated ions moving through matter. Figure ?? shows the trajectory of one hundred 13MeV protons entering and passing through an Iron target, and it is this set of data points (together with the cross section database) that the Activity code uses to calculate the reaction rates for the transmutation of nuclei in the target. At higher energies, the ions slow as they lose energy due to electronic stopping, but as the ion energy drops the mechanism of loss through nuclear collisions becomes important. The spreading of ion depths at lower energies is a result of the higher momentum transfer during nuclear collisions, as can be seen in Figure ??.

Chapter 5

Background: Interatomic Potential Fitting

In order to model Fe and Pd with Molecular Dynamics codes, an interatomic potential is needed. This will require experimental data and data generated by first principles calculations. The simplified model will consist of just Fe and Pd, but pure Fe does not take the FCC structure that it does when alloyed with Nickel in Austenitic Stainless Steel.

The properties of theoretical pure FCC Fe are estimated using Density Functional Theory that solves the many body Schrödinger Equation. While it is impossible to solve this equation exactly, with our current technology and knowledge, it is possible to solve approximately by making several approximations and by using the Hohenberg-Kohn theorem.

Many bodey potentials such as the FS and embedded-atom method are often used to model metals. The force matching method is used to fit the potentials to data. Optimization algorithms are split into global and local, with an example of a global being simulated annealing and a local being BFGS.

5.1 Experiment, Modelling and Theory

5.1.1 Introduction

We do not have a complete understanding of the world around us, so it may be that experiment is the “best” method of testing a material, as by its nature it will obey the rules of physics. As far as we know, these do not change from one place to another. A piece of steel used in an experiment is never going to have precisely the same composition and structure as similar steel use in a reactor, but it should be close enough.

The scanning electron microscope has a magnification of approximately 1 million times and they are able to generate a picture of the surface of a specimen using a beam of electrons. The transmission electron microscope has the ability to magnify a specimen further, with a resolution of less than 1 angstrom. The trade off is that a it covers a smaller area of the specimen than a SEM and the sample must be prepared in thin slices.

The composition of an irradiated sample may be tested by a number of methods including neutron activation analysis and secondary-ion mass spectrometry. Scattering techniques, such as x-ray or neutron diffraction, can give an insight into the structure of a material, but they are statistical methods and do not give detailed measurements of individual atoms or defects.

There are draw backs to experiments, several of which are particular to this work. Even with our advances in technology, there are still errors introduced into any experiment. When dealing with smaller and smaller volumes of atoms quantum effects will also need to be considered, but this is perhaps a difficultly in our inability to visualise what happens on such small scales.

Radiation damage experiments, whether by neutrons or ions, will result in radioactive waste and the target must be safe to handle to be examined. The collision event happens up to a micron or more into the material. They occur on a very short timescale and within small volumes of space at random points along the path of the projectile, so the events would be very hard or impossible to track as they occur with current technology.

Current theories have been developed and modified over hundreds of years, and in the last 100 years Quantum Mechanics has been introduced to better describe physics on a small scale. It is a well proven theory that has been very successful. Unfortunately, using the theory exactly for a large ensemble of atoms and electrons is impossible with our current level of technology.

Computer models use theory, and a number of approximations, to simulated reality. These models may need to be fine tuned, to better fit both the theory and experiment, but they allow us to do what is not possible with either experiment or theory. It is possible to simulate an individual damage cascade and watch it in fine detail spatially and temporally. As computer power increases, the models used become more complex and the simulation boxes and time spans grow.

This chapter discusses the background required to link the more accurate DFT to MD by deriving interatomic potentials based on experiment and calculated data. By doing this, the concentrations at the grain boundary for an iron-palladium alloy may be modelled following irradiation damage.

5.1.2 Simulating Materials on a Variety of Scales in Time and Space

Taking a 1 micron grain in a steel as an example, it would contain tens of billions of atoms. There are a wide range of modelling programs available (fig. ??).

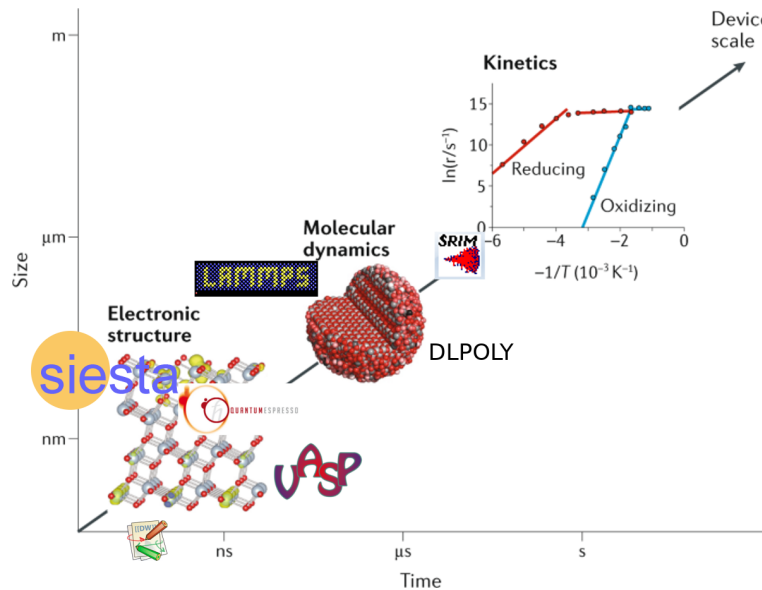


Figure 5.1: Time and Size Scales for Computer Packages [scalediagram]

The properties of metals may be approximated using small crystals, and this is ideally suited to DFT calculations. Simulations of small ensembles of atoms over time are now also possible using DFT molecular dynamics. Larger simulations containing thousands to millions of atoms, that are able to simulate single damage cascades are suitable for MD simulations.

5.2 Properties of Crystals

5.2.1 Introduction

There are seven crystal classes (table. ??) and 14 Bravias lattices (section ??), although this work is only concerned with cubic and orthorhombic crystals.

Class	Lengths	Angles
Cubic	$a = b = c$	$\alpha = \beta = \gamma = 90^\circ$
Hexagonal	$a = b, c$	$\alpha = \beta, \gamma = 120^\circ$
Rhombohedral	$a = b = c$	$\alpha = \beta = \gamma \neq 90^\circ$
Tetragonal	$a = b, c$	$\alpha = \beta = \gamma = 90^\circ$
Orthorhombic	a, b, c	$\alpha = \beta = \gamma = 90^\circ$
Monoclinic	a, b, c	$\alpha = \beta = 90^\circ, \gamma \neq 90^\circ$
Triclinic	a, b, c	$\alpha, \beta, \gamma,$

Table 5.1: Seven Crystal Classes

Metals are rarely single crystals, but are made from many crystals separated by grain boundaries. However, the knowledge of the microscopic crystals translates well to the properties of the metals on a macroscopic scale.

This work does not attempt to calculate properties based on a collection of many crystals, but on a single crystal with less than a thousand atoms. The crystals are then assumed to be infinite in size, due to periodic boundary conditions.

5.2.2 Equation of State

The equation of state of a material relates either the pressure on that material as a function of the volume, or the energy of a sample of a material to the volume. This not only allows one to predict the energy or pressure at a certain volume, but also the minimum energy, relaxed volume and the bulk modulus.

Bulk Modulus

The bulk modulus of a material is defined as the bulk stress of a sample divided by the bulk strain on that sample and several example values are given in table ???. It is also the inverse of the compressibility of that material, which means that materials with a higher bulk modulus are less compressible than those with a lower value.

$$B_0 = -V \frac{\partial P}{\partial V} \quad (5.1)$$

$$B_0 = V \frac{\partial^2 E}{\partial V^2} \quad (5.2)$$

Material	Bulk Modulus/GPa
Aluminium	70
Iron (BCC)	110
Stainless Steel 18-8	163

Table 5.2: Example bulk modulii for three metals

Murnaghan Equation of State

Hooke's law implies a linear relationship between stress and strain. In practice, where a pressure is applied to a material, the application of Hooke's law is limited[**murnaghaneq**]. Muraghan derived a new equation to improve upon formulae developed in the 1930's, using compression data from high pressure experiments.

$$P(V) = \frac{B_0}{B'_0} \left(\left(\frac{V_0}{V} \right)^{B'_0} - 1 \right) \quad (5.3)$$

As pressure is the negative derivative of the internal energy of the system with respect to change in volume, $p = -(\partial E/dV)$, and the equation can be integrated and written in terms of the energy, volume, bulk modulus and its derivative[**crystaleos**].

$$E(V) = E_0 + \frac{B_0 V}{B'_0} \left[\left(\frac{V_0}{V} \right)^{B'_0} \frac{1}{B'_0 - 1} + 1 \right] - \frac{B_0 V_0}{B'_0 - 1} \quad (5.4)$$

Birch-Murnaghan Equation of State

Several years after Murnaghan's equation, Birch developed the equation of state further upon the experimental data provided by work from Bridgman in high pressure physics. For cubic symmetry, the description of free energy now includes third order terms in the strain components[**birchmurnaghaneq**].

$$P(V) = \frac{3B_0}{2} \left[\left(\frac{V_0}{V} \right)^{\frac{7}{3}} - \left(\frac{V_0}{V} \right)^{\frac{5}{3}} \right] \left[1 + \frac{3}{4}(B'_0 - 4) \left(\left(\frac{V_0}{V} \right)^{\frac{2}{3}} - 1 \right) \right] \quad (5.5)$$

The energy-volume relationship may again be constructed[**crystaleos**].

$$E(V) = E_0 + \frac{9V_0 B_0}{16} \left[\left[\left(\frac{V_0}{V} \right)^{\frac{2}{3}} - 1 \right]^3 B'_0 + \left[\left(\frac{V_0}{V} \right)^{\frac{2}{3}} - 1 \right]^2 \left[6 - 4 \left(\frac{V_0}{V} \right)^{\frac{2}{3}} \right] \right] \quad (5.6)$$

In order to fit the Birch-Murnaghan, the first step is to fit a second order polynomial to the energy-volume data. This may be achieved using least-squares fitting with a vandermonde matrix. The coefficients from this polynomial may then be used to calculate reasonable value for E_0 , V_0 and B_0 ; sane starting values of B'_0 are between 1 and 10, and the code takes a starting value of 2[**gilgamesheos**].

$$\begin{aligned}
E(V) &= c_0 + c_1 V + c_2 V^2 \\
V_0 &= -\frac{c_1}{2c_2} \\
E_0 &= c_2 * V_0^2 + c_1 V_0 + c_0 \\
B_0 &= 2c_2 V_0 \\
B'_0 &= 2
\end{aligned} \tag{5.7}$$

Newton Gauss is then used to minimise E_0 , V_0 and B_0 while $B'_0 \in 1.0, 1.5, 2.0, 2.5, 3.0, 3.5, 4.0, 4.5, 5.0, 5.5, 6.0$

$$[J^T J] P = J^T R \tag{5.8}$$

The parameters with the lowest residual square sum are returned.

5.2.3 Voigt Notation

Where a tensor is symmetric, Voigt notation is used to simplify how the tensor is written. It reduces a second order tensor such as stress or strain, represented by a 3x3 matrix, to a 6 row matrix. It also reduces a fourth order tensor, such as the compliance or stiffness tensor (represented by a 3x3x3x3 matrix), to a 6x6 matrix.

$$\vec{A} = \begin{bmatrix} A_{11} & A_{12} & A_{13} \\ A_{21} & A_{22} & A_{23} \\ A_{31} & A_{32} & A_{33} \end{bmatrix} = \begin{bmatrix} A_{11} \\ A_{22} \\ A_{33} \\ A_{23} \\ A_{13} \\ A_{12} \end{bmatrix} \text{ if } \vec{A} \text{ is symmetric} \tag{5.9}$$

5.2.4 Elastic Constants

Stress and strain are both related by either the stiffness tensor C , filled with the elastic constants, the compliance tensor S and this is the inverse of the stiffness tensor. Strain is a measure of the deformation of a material and by definition has no units. In one dimension $\epsilon = \frac{\delta l}{l_0}$ where l_0 is the unstrained length and δl is the change in length. The Generalized Hooke's law relating these tensors allows the computation of the Cauchy stress if the elastic constants are known and an input strain is provided.

$$\vec{A} = \begin{bmatrix} \epsilon_{11} & \epsilon_{12} & \epsilon_{13} \\ \epsilon_{21} & \epsilon_{22} & \epsilon_{23} \\ \epsilon_{31} & \epsilon_{32} & \epsilon_{33} \end{bmatrix} = \begin{bmatrix} \epsilon_{11} \\ \epsilon_{22} \\ \epsilon_{33} \\ \epsilon_{23} \\ \epsilon_{13} \\ \epsilon_{12} \end{bmatrix} \text{ where } \epsilon_{ij} \equiv \frac{1}{2} \left(\frac{\partial u_i}{\partial x_j} + \frac{\partial u_j}{\partial x_i} \right) \tag{5.10}$$

$$\vec{\sigma}_{ij} = \vec{C}_{ijkl} \vec{\epsilon}_{kl} \tag{5.11}$$

$$\vec{\epsilon}_{ij} = \vec{S}_{ijkl} \vec{\sigma}_{kl} \quad (5.12)$$

$$\epsilon_{ij} = \begin{bmatrix} \epsilon_1 = \epsilon_{11} = \epsilon_{11} \\ \epsilon_2 = \epsilon_{22} = \epsilon_{22} \\ \epsilon_3 = \epsilon_{33} = \epsilon_{33} \\ \epsilon_4 = \epsilon_{23} = \epsilon_{32} \\ \epsilon_5 = \epsilon_{13} = \epsilon_{31} \\ \epsilon_6 = \epsilon_{12} = \epsilon_{21} \end{bmatrix} \quad (5.13)$$

$$\begin{bmatrix} \sigma_1 \\ \sigma_2 \\ \sigma_3 \\ \sigma_4 \\ \sigma_5 \\ \sigma_6 \end{bmatrix} = \begin{bmatrix} C_{11} & C_{12} & C_{13} & C_{14} & C_{15} & C_{16} \\ C_{21} & C_{22} & C_{23} & C_{24} & C_{25} & C_{26} \\ C_{31} & C_{32} & C_{33} & C_{34} & C_{35} & C_{36} \\ C_{41} & C_{42} & C_{43} & C_{44} & C_{45} & C_{45} \\ C_{51} & C_{52} & C_{53} & C_{54} & C_{55} & C_{55} \\ C_{61} & C_{62} & C_{63} & C_{64} & C_{65} & C_{66} \end{bmatrix} \begin{bmatrix} \epsilon_1 \\ \epsilon_2 \\ \epsilon_3 \\ \epsilon_4 \\ \epsilon_5 \\ \epsilon_6 \end{bmatrix} \quad (5.14)$$

The number of independent elastic constants changes depending on the symmetry of the crystal. The tensors in Voigt notation are given for cubic, orthorhombic/orthotropic, monoclinic and triclinic in appendix ??.

5.2.5 Calculating Elastic Constants for a Cubic Crystal

Cubic crystals are the most simple class with primitive unit cells having three orthonormal basis vectors. Four of the most common variants of the cubic crystal are the simple cubic, body centered cubic, face centered cubic and zincblende. Due to symmetry, a cubic crystal has only three elastic independent constants; in Voigt notation these are C_{11} , C_{12} and C_{44} .

Applying two strains to a cubic crystal [**pressuredepmehl**] coupled with the calculation of the Bulk Modulus, as already discussed, allows the three independent elastic constants to be calculated.

First, the bulk modulus may be calculated either by finding the second derivative of the energy wrt volume at the relaxed volume, $B(V) = -VP'(V) = VE''(V)$ [**pressuredepmehl**], or by fitting the Birch-Murnaghan equation of state.

$$\epsilon_{(C_{11}-C_{22})} = \begin{bmatrix} \delta & 0 & 0 \\ 0 & -\delta & 0 \\ 0 & 0 & \delta^2/(1-\delta^2) \end{bmatrix} \quad (5.15)$$

Second, a volume conserving orthorhombic strain (eq. ??) may be applied to the crystal [**pressuredepmehl**]. The relation between the relaxed energy and that under strain is symmetric about $E(0)$ and is given by $E(\delta) = E(-\delta) = E(0) + (C_{11} - C_{12})V\delta^2 + O[\delta^4]$ [**pressuredepmehl**]. V is the volume of the relaxed unit cell and $E(0)$ is the minimum energy. By fitting a polynomial to the energy-strain data, the coefficient for the quadratic term is equal to $(C_{11} - C_{12})V$.

$$\epsilon_{(C44)} = \begin{bmatrix} 0 & \frac{\delta}{2} & 0 \\ \frac{\delta}{2} & 0 & 0 \\ 0 & 0 & \delta^2/(4 - \delta^2) \end{bmatrix} \quad (5.16)$$

Third, a volume conserving monoclinic strain (eq. ??) is applied and the relation between the relaxed energy, strained energy and the elastic constant C_{44} is $E(\delta) = E(-\delta) = E(0) + \frac{1}{2}C_{44}V\delta^2 + O[\delta^4]$. Similarly, fitting a polynomial to the strain-energy data points will calculate the value of C_{44} .

Finally, the relation between the bulk modulus, C_{11} and C_{12} , $B_0 = (C_{11} + 2C_{12})/3$ allows the computation of the individual constants eq. ?? (this relationship is only for cubic crystals).

$$\begin{aligned} C_{ortho} &= C_{11} - C_{12} \\ C_{11} &= \frac{3B_0 + 2C_{ortho}}{3} \\ C_{12} &= \frac{3B_0 - C_{ortho}}{3} \end{aligned} \quad (5.17)$$

5.2.6 Calculating Elastic Constants for Orthorhombic Crystal

The DFT work here includes Pd and Fe. The natural arrangement of Pd atoms in a pure sample are FCC within a cubic crystal. Pure iron at room temperature is BCC, but this work is interested in austenitic stainless steel where the structure of atoms in the alloy are FCC. When modelling FCC iron using DFT with a non-polarized calculation, the crystal favours a cubic crystal with the atoms fixed in the FCC positions. When a spin-polarized calculation is computed, with magnetization along the z-axis, the crystal becomes slightly tetragonal with one side being 5% larger than the other two.

$$C_{ij} = \begin{bmatrix} C_{11} & C_{12} & C_{12} & 0 & 0 & 0 \\ C_{12} & C_{11} & C_{12} & 0 & 0 & 0 \\ C_{12} & C_{12} & C_{11} & 0 & 0 & 0 \\ 0 & 0 & 0 & C_{44} & 0 & 0 \\ 0 & 0 & 0 & 0 & C_{44} & 0 \\ 0 & 0 & 0 & 0 & 0 & C_{44} \end{bmatrix} \quad (5.18)$$

(3 independent values)

$$C_{ij} = \begin{bmatrix} C_{11} & C_{12} & C_{13} & 0 & 0 & 0 \\ C_{12} & C_{22} & C_{23} & 0 & 0 & 0 \\ C_{13} & C_{23} & C_{33} & 0 & 0 & 0 \\ 0 & 0 & 0 & C_{44} & 0 & 0 \\ 0 & 0 & 0 & 0 & C_{55} & 0 \\ 0 & 0 & 0 & 0 & 0 & C_{66} \end{bmatrix} \quad (5.19)$$

(9 independent values)

Once the relaxed crystal basis vectors and atom positions have been determined for the orthorhombic crystal, nine strains are applied to the crystal [DftTiSiRavindran] in order to calculate the nine independent elastic constants.

As a strain is applied to a crystal its energy can change. The volume may also change, although it may be held constant. The relationship between the energy and the strain σ may be represented as a Taylor expansion of the internal energy in powers of the strain tensor[DftTiSiRavindran]. The equation used by Ravindran et al is in a slightly different notation to that used by Mehl[elasticpropertiesmehl]. It includes a constant xi to account for the symmetry of σ and the use of Voigt notation.

$$E(V, \sigma) = E(V_0, 0) + V_0 \left(\sum_i \tau_i \xi_i \sigma_i + \frac{1}{2} \sum_{ij} c_{ij} \sigma_i \xi_i \sigma_j \xi_j \right) + O(\sigma^3)$$

where σ is the strain
and τ is the stress

if the index k of ξ is $\in 1, 2, 3$ then $\xi_k = 1$
if the index k of ξ is $\in 4, 5, 6$ then $\xi_k = 2$

The first three strains applied to the orthorhombic crystal are non-volume conserving. They strain the crystal along each axis and allow the calculation of C_{11} , C_{22} and C_{33} .

$$D_1 = \begin{bmatrix} 1 + \delta & 0 & 0 \\ 0 & 1 & 0 \\ 0 & 0 & 1 \end{bmatrix} \quad (5.21) \quad E(V, \sigma) = E(V_0, 0) + V_0 \left(\tau_1 \sigma + \frac{c_{11}}{2} \sigma^2 \right) \quad (5.22)$$

$$D_2 = \begin{bmatrix} 1 & 0 & 0 \\ 0 & 1 + \delta & 0 \\ 0 & 0 & 1 \end{bmatrix} \quad (5.23) \quad E(V, \sigma) = E(V_0, 0) + V_0 \left(\tau_2 \sigma + \frac{c_{22}}{2} \sigma^2 \right) \quad (5.24)$$

$$D_3 = \begin{bmatrix} 1 & 0 & 0 \\ 0 & 1 & 0 \\ 0 & 0 & 1 + \delta \end{bmatrix} \quad (5.25) \quad E(V, \sigma) = E(V_0, 0) + V_0 \left(\tau_3 \sigma + \frac{c_{33}}{2} \sigma^2 \right) \quad (5.26)$$

Volume conserving monoclinic distortions (eq. ??, eq. ??, eq. ??) are used to calculate the C_{44} , C_{55} and C_{66} elastic constants (eq. ??, eq. ??, eq. ??).

$$D_4 = \begin{bmatrix} \frac{1}{(1-\sigma^2)^{\frac{1}{3}}} & 0 & 0 \\ 0 & \frac{1}{(1-\sigma^2)^{\frac{1}{3}}} & \frac{\sigma}{(1-\sigma^2)^{\frac{1}{3}}} \\ 0 & \frac{\sigma}{(1-\sigma^2)^{\frac{1}{3}}} & \frac{1}{(1-\sigma^2)^{\frac{1}{3}}} \end{bmatrix} \quad E(V, \sigma) = E(V_0, 0) + V_0 \left(2\tau_4 \sigma + 2 \frac{c_{44}}{2} \sigma^2 \right) \quad (5.28)$$

$$D_5 = \begin{bmatrix} \frac{1}{(1-\sigma^2)^{\frac{1}{3}}} & 0 & \frac{\sigma}{(1-\sigma^2)^{\frac{1}{3}}} \\ 0 & \frac{1}{(1-\sigma^2)^{\frac{1}{3}}} & 0 \\ \frac{\sigma}{(1-\sigma^2)^{\frac{1}{3}}} & 0 & \frac{1}{(1-\sigma^2)^{\frac{1}{3}}} \end{bmatrix} \quad E(V, \sigma) = E(V_0, 0) + V_0 \left(2\tau_5 \sigma + 2 \frac{c_{55}}{2} \sigma^2 \right) \quad (5.30)$$

$$D_6 = \begin{bmatrix} \frac{1}{(1-\sigma^2)^{\frac{1}{3}}} & \frac{\sigma}{(1-\sigma^2)^{\frac{1}{3}}} & 0 \\ \frac{\sigma}{(1-\sigma^2)^{\frac{1}{3}}} & \frac{1}{(1-\sigma^2)^{\frac{1}{3}}} & 0 \\ 0 & 0 & \frac{1}{(1-\sigma^2)^{\frac{1}{3}}} \end{bmatrix} \quad (5.31)$$

$$E(V, \sigma) = E(V_0, 0) + V_0 \left(2\tau_6 \sigma + 2 \frac{c_{66}}{2} \sigma^2 \right) \quad (5.32)$$

Finally, three orthorhombic strains (eq. ??, eq. ??, eq. ??) that conserve the volume, by altering the strain along each axis, are used to calculate the C_{12} , C_{13} and C_{23} elastic constants (eq. ??, eq. ??, eq. ??).

$$D_7 = \begin{bmatrix} \frac{1+\sigma}{(1-\sigma^2)^{\frac{1}{3}}} & 0 & 0 \\ 0 & \frac{1-\sigma}{(1-\sigma^2)^{\frac{1}{3}}} & 0 \\ 0 & 0 & \frac{1}{(1-\sigma^2)^{\frac{1}{3}}} \end{bmatrix} \quad (5.33)$$

$$E(V, \sigma) = E(V_0, 0) + V_0 \left((\tau_1 - \tau 2\sigma + \frac{1}{2}(c_{11} + c_{22} - 2c_{12})\sigma^2) \right) \quad (5.34)$$

$$D_8 = \begin{bmatrix} \frac{1+\sigma}{(1-\sigma^2)^{\frac{1}{3}}} & 0 & 0 \\ 0 & \frac{1}{(1-\sigma^2)^{\frac{1}{3}}} & 0 \\ 0 & 0 & \frac{1-\sigma}{(1-\sigma^2)^{\frac{1}{3}}} \end{bmatrix} \quad (5.35)$$

$$E(V, \sigma) = E(V_0, 0) + V_0 \left((\tau_1 - \tau 3\sigma + \frac{1}{2}(c_{11} + c_{33} - 2c_{13})\sigma^2) \right) \quad (5.36)$$

$$D_9 = \begin{bmatrix} \frac{1}{(1-\sigma^2)^{\frac{1}{3}}} & 0 & 0 \\ 0 & \frac{1+\sigma}{(1-\sigma^2)^{\frac{1}{3}}} & 0 \\ 0 & 0 & \frac{1-\sigma}{(1-\sigma^2)^{\frac{1}{3}}} \end{bmatrix} \quad (5.37)$$

$$E(V, \sigma) = E(V_0, 0) + V_0 \left((\tau_2 - \tau 3\sigma + \frac{1}{2}(c_{22} + c_{33} - 2c_{23})\sigma^2) \right) \quad (5.38)$$

5.2.7 Stability Conditions

Whilst the elastic constants may be computed using first-principles calculations, there are a series of assumptions and approximations made in order to solve first-principles calculations in a reasonable amount of time. There must be a sanity check, as it is no use to compute the elastic constants from DFT to find the crystals are unstable.

For a cubic crystal with three independent elastic constants and zero stress, the Born elastic stability criteria apply[acklandec]. The bulk modulus should be positive $(C_{11} + 2C_{12})/3 > 0$, the tetragonal shear should be positive $C_{11} - C_{12} > 0$ and the shear modulus should be positive $c_{44} > 0$.

For an orthorhombic crystal, there are additional conditions given there are nine independent elastic constants (eq. ??)[ghoshstability].

$$\begin{aligned} C_{11} > 0, C_{22} > 0, C_{33} > 0, C_{44} > 0, C_{55} > 0, C_{66} > 0 \\ (C_{11} + C_{22} - 2C_{12}) > 0, (C_{11} + C_{33} - 2C_{13}) > 0, (C_{22} + C_{33} - 2C_{23}) > 0 \\ (C_{11} + C_{22} + C_{33} + 2C_{12} + 2C_{13} + 2C_{23}) > 0 \end{aligned} \quad (5.39)$$

5.2.8 Computing Values from Elastic Constants

The bulk modulus, as noted earlier, is a measure of the effect of strain on stress. While it may be calculated by taking the second derivative of energy with respect to volume, or by fitting an equation of state, it may also be calculated using the elastic constants of a material or the compliance constants.

For cubic crystals the elastic constants may be used to calculate the bulk modulus, tetragonal shear, shear modulus and Cauchy pressure (eq. ??).

$$\begin{aligned} B_0 &= \frac{C_{11} + 2C_{12}}{3} = \frac{5C_{11}}{9} \text{ Bulk Modulus} \\ C' &= \frac{C_{11} - C_{12}}{2} \text{ Tetragonal Shear} \\ &\quad C_{44} \text{ Shear Modulus} \\ p_c &= C_{12} - C_{44} \text{ Cauchy Pressure} \end{aligned} \tag{5.40}$$

For an orthorhombic crystal, the Voigt bulk modulus (eq. ??) and Reuss bulk modulus (eq. ??) may be calculated from the stiffness and compliance matrix respectively. These two values are then averaged to give the bulk modulus (eq. ??)[DftTiSiRavindran].

$$B_V = \frac{1}{9} (C_{11} + C_{22} + C_{33} + 2(C_{12} + C_{13} + C_{23})) \tag{5.41}$$

$$B_R = (S_{11} + S_{22} + S_{33} + 2(S_{12} + S_{13} + S_{23}))^{-1} \tag{5.42}$$

$$B = 0.5(B_V + B_R) \tag{5.43}$$

Calculation by this method is particularly useful for this work, where the FCC iron crystal is orthorhombic, and not cubic (section ??).

Elastic constants are also used to calculate the shear modulus G . Where the crystal is cubic, there are several elastic constants that can be used (eq. ??)[DftTiSiRavindran]. Both the Voigt (eq. ??) and Reuss (eq. ??) values are calculated and averaged to give the value of G (eq. ??).

$$G = C_{44} = 0.5(C_{11} - C_{12}) = \frac{C_{11}}{3} \tag{5.44}$$

$$G_V = \frac{1}{15} (C_{11} + C_{22} + C_{33} - C_{12} - C_{13} - C_{23}) + \frac{1}{5} (C_{44} + C_{44} + C_{55}) \tag{5.45}$$

$$G_R = \frac{15}{4(S_{11} + S_{22} + S_{33}) - 4(S_{12} + S_{23} + S_{23}) + 3(S_{44} + S_{55} + S_{66})} \tag{5.46}$$

$$G = 0.5(G_V + G_R) \quad (5.47)$$

The Young's modulus E as a scalar is a measure of how easily the length an isotropic material is changed under tension or compression, and the computed elastic constants for a cubic crystal may be used to calculate E (eq. ??).

$$E = \frac{9B_0G}{3B_0 + G} \text{ where } B_0 \text{ is the bulk modulus and } G \text{ is the shear modulus} \quad (5.48)$$

The Poisson ration is a measure of how much a material changes in the direction perpendicular to a strain applied transversely.

$$\nu = -\frac{d\epsilon_{perp}}{d\epsilon_{transverse}} \quad (5.49)$$

The bulk modulus may be calculated from the equation of state or elastic constants, and the shear modulus may be calculated from the elastic constants. In turn, the Poisson ratio is calculated from these.

$$\nu = \frac{3B_0 - 2G}{2(3B + G)} \quad (5.50)$$

The ratio may be used as another data point in order to fit a potential, or at the very least as a check to compare to the known value once a potential has been derived.

5.2.9 Correlation of Melting Temperature in Metals with Elastic Constants

There is a correlation between the melting temperature of metals and their elastic constants detailed in eq. ?? and fig. ?? [ElasticMeltingTemp].

$$T \approx 598.0 + 6.66 \times (C_{11} + C_{22} + C_{33}) - 0.003 \times (C_{11} + C_{22} + C_{33}) \quad (5.51)$$

Where the temperature is in K, and the elastic constants are in GPA

The correlation values between the temperature and C_{11} are 0.848 and 0.780 for the Pearson and Spearman's correlation respectively. An accurate temperature will not be possible to predict, but it will act as a further sanity check within the computer codes developed in the results section of this work.

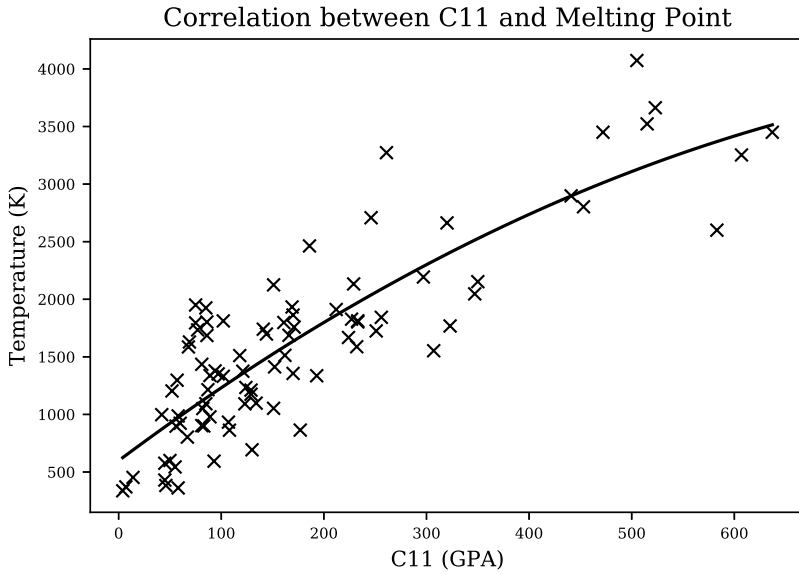


Figure 5.2: Correlation between C_{11} and temperature

5.3 Interatomic Potentials

5.3.1 Introduction

An interatomic potential, as used in this work and Molecular Dynamics computer codes, is a function or a set of functions that describe the energy and force between atoms. Simpler functions represent the potential energy between pairs of atoms only, but more complicated functions have been used in molecular dynamics since the 1980s that also attempt to represent the many body nature of materials, which applies in particular to metals.

5.3.2 Pair Potentials

A pair potential only considers individual pairs of nearby atoms, one pair at a time, and does not consider the effect of any other nearby atoms. Where an alloy is being modelled, there will be a pair potential function for each element and element combination; 1 for a single element, 3 for a two element alloy, 6 for a three element alloy and so on.

Lennard-Jones

The Lennard-Jones potential was proposed in the 1920s and has both an attractive term and a repulsive term; the $(r_m/r)^{12}$ becomes much larger than the $(r_m/r)^6$ term at close distances, and this mimics the coulomb repulsion as two atoms are pushed closer together. At larger separations, the attractive term dominates.

$$V(r) = e \left(\left(\frac{r_m}{r} \right)^{12} - 2 \left(\frac{r_m}{r} \right)^6 \right) \quad (5.52)$$

Lennard-Jones Potential

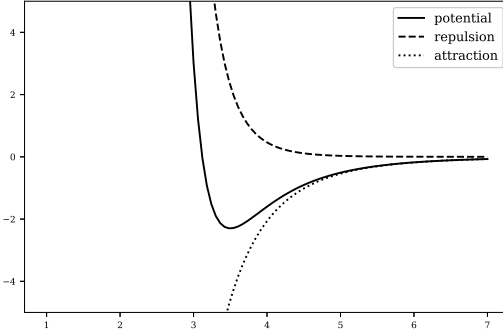


Figure 5.3: Lennard-Jones Potential

Morse Potential

The Morse potential was proposed five years after the Lennard-Jones potential. It also has an attractive and repulsive term, but it uses the exponential function rather than 6th and 12th powers.

$$V(r) = \exp(-2a(r - re)) - 2\exp(-a(r - re)) \quad (5.53)$$

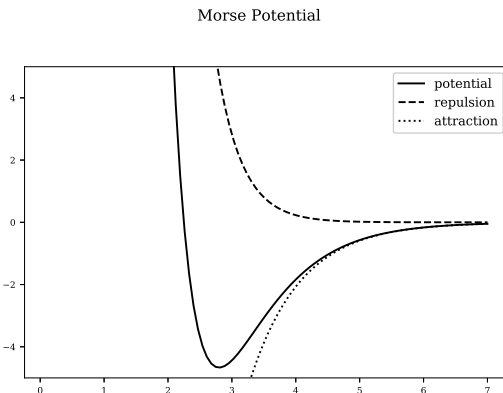


Figure 5.4: Morse Potential

Buckingham Potential

The Buckingham Potential consists of a repulsive and attractive part. As the separation decreases, the attractive term dominates and the overall function tends towards negative infinity. This shouldn't be problematic when gasses or solids are being modelled alone, but when collisions and damage cascades are being modelled, the separation between atoms may be much smaller than that in a typical simulation, ending with these atoms being pulled together (eq. ?? and fig. ??).

$$V(r) = A\exp(-Br) - \frac{C}{r^6} \quad (5.54)$$

Buckingham Potential

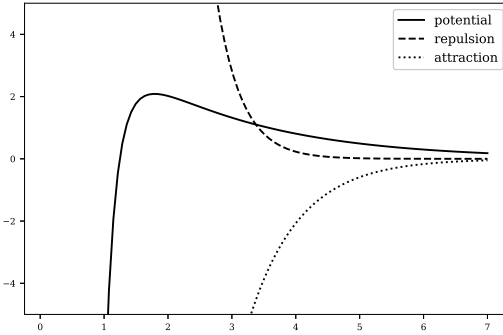


Figure 5.5: Buckingham Potential

Ziegler-Biersack-Littmark Universal Potential Function

It became clear, while experimenting with a number of existing potentials and molecular dynamics programs, that at the very least modifications to those potentials would need to be made for small atom separations. A simulation to model a projectile failed early on due to the projectile's proximity to target atoms, resulting in the MD code returning an error as the separation was out of the range of the potential.

The Ziegler-Biersack-Littmark potential, between an atom of charge Z_i and Z_j is set out in the SRIM manual [**srimbook**].

$$V_{zbl}(r_{ij}, Z_i, Z_j) = \frac{1}{4\pi\epsilon_0} \frac{Z_i Z_j}{r_{ij}} \phi\left(\frac{r_{ij}}{a_{ij}}\right) \quad (5.55)$$

where $\epsilon_0 = 8.85419 \times 10^{-12}$

The parameters of the Universal screening potential function are as follows:

$$\phi(x) = 0.181e^{-3.2x} + 0.5099e^{-0.9423x} + 0.2802e^{-0.4029x} + 0.02817e^{-0.2016x} \quad (5.56)$$

where $a_{ij} = \frac{0.8854a_0}{Z_i^{0.23} + Z_j^{0.23}}$

and $a_0 = 0.529$ angstrom

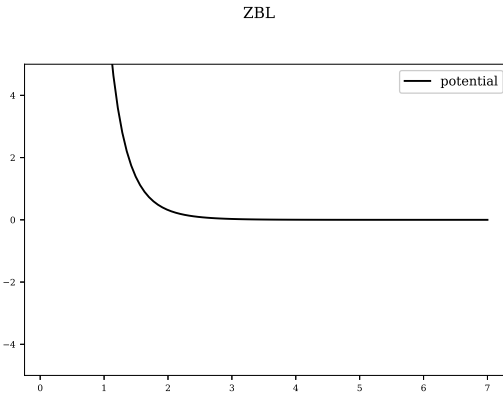


Figure 5.6: ZBL universal screening potential

5.3.3 Many Body Potentials

This work is focused on metals, and two popular, and closely related potentials, will be discussed in this section.

Finnis-Sinclair

The Finnis-Sinclair potential was published in 1984[finnissinclair] and it introduced both a pair potential and an embedded term to take into account the cohesive energy dependent on the local electron density. The pair term represents the repulsion between the atoms whereas the embedding functional glues the atoms together in the solid.

The tight-binding that this potential is based on is represented by the functional: square root of the density. The potential for a single element model consists of a pair function, a density function and a tight-binding functional.

$$\begin{aligned}
 w^{A,A} &= \sum_{i \neq j}^N(r) v^{A,A}(r_{ij}) \\
 \rho_i^A(r) &= \sum_{j,j \neq i}^N \phi(r_{ij}) \\
 F^A &= \sum_i^N \rho_i
 \end{aligned} \tag{5.57}$$

Embedded-atom method

The embedded-atom method was also invented in the 1980s. It was developed with metals in mind, and in many ways is a more flexible variant of the Finnis-Sinclair potential. It too has a pair and density function, but the functional of the EAM potential is not restricted to a square root.

$$U_{EAM} = \frac{1}{2} \sum_{i=1}^N \sum_{j \neq i}^N V_{ij}(r_{ij}) + \sum_{i=1}^N F[\rho_i] \quad (5.58)$$

where $\rho_i = \sum_{j=i, j \neq i}^N \rho_{ij}(r_{ij})$

Elastic properties were not reliably calculated from pair functions alone[**dawbaskeseam**], but the advent of Finnis-Sinclair and EAM type potentials changed this.

$$A_{ij} + F'(\vec{\rho})V_{ij} = 0$$

where

$$A_{ij} = \frac{1}{2} \sum_m \phi'_m a_i^m a_j^m / a^m \quad (5.59)$$

$$V_{ij} = \frac{1}{2} \sum_m \rho'_m a_i^m a_j^m / a^m$$

$$C_{11} = (B_{11} + F'(\vec{\rho})W_{11} + F''(\vec{\rho})(V_{11})^2) / \Omega_0$$

$$C_{12} = (B_{12} + F'(\vec{\rho})W_{12} + F''(\vec{\rho})(V_{11})^2) / \Omega_0$$

$$C_{44} = (B_{12} + F'(\vec{\rho})W_{12}) / \Omega_0$$

where

$$B_{ijkl} = \frac{1}{2} \sum_m (\phi''_m - \phi'_m / a^m) a_i^m a_j^m a_k^m a_l^m / (a^m)^2 \quad (5.60)$$

$$W_{ijkl} = \frac{1}{2} \sum_m (\rho''_m - \rho'_m / a^m) a_i^m a_j^m a_k^m a_l^m / (a^m)^2$$

where

$$\phi''_m = (d^2\phi(r)/dr^2)_{r=a^m},$$

$$\rho''_m = (d^2\rho(r)/dr^2)_{r=a^m}.$$

For homonuclear cubic crystals, the lattice constant may be calculated by the equilibrium condition in eq ???. The three independent elastic constants, C_{11} , C_{12} , C_{44} , may also be calculated at equilibrium from eq ???. There are notable consequences in removing either the pair function or embedding functional. If $V_{ij}(r_{ij})$ is removed, $F'[\vec{\rho}] = 0$ and this gives a shear modulus of 0 ($C_{11} = C_{12}, C_{44} = 0$)[**dawbaskeseam**]. If $F[\vec{\rho}]$ is removed the Cauchy discrepancy becomes zero ($C_{12} = C_{44}$)[**dawbaskeseam**]. Both of these situations are generally untrue, and both functions are required for a good potential for a metal.

Two band embedded-atom method

There are several variations of the potential, and one of particular interest to us is the two band embedded-atom method that has two electron density and embedding energy terms. This formalism was originally developed to model Caesium[**twobandackland**], and the transition of electrons between S and D bands under pressure, but it has been modified to apply to alloys.

Caesium changes its structure as pressure is applied. The first change is from BCC to a more compact FCC structure, but it then compresses further as electrons move from the S-band to the more compact D-band, reducing the size of the atom.

The bond energy may be described with eq. ?? where N_1 and N_2 are the capacities of each band, n_{i1} and n_{i2} are the electrons in each band of the i^{th} atom. E_{prom} is the energy required to promote an electron from band 1 to band 2.

$$U_{\text{bond}} = \sum_i \frac{W_{i1}}{2N_1} n_{i1}(n_{i1} - N_1) + \sum_i \frac{W_{i2}}{2N_2} n_{i2}(n_{i2} - N_2) + E_{\text{prom}} \quad (5.61)$$

A Finnis-Sinclair type EAM potential was used by Ackland and Reed in this work for both bands. The parameters fitted in Ackland and Reed's work are listed in table ??.

$$\begin{aligned} & \text{Pair} \\ V_s(r_{ij}) &= \sum_i \frac{A_s}{r_{ij}^{12}} \\ V_d(r_{ij}) &= \sum_i \frac{A_d}{r_{ij}^{12}} \end{aligned} \quad (5.62)$$

$$\rho_s(r_{ij}) = \begin{cases} C_s(d_s - r_{ij})^3 & r_{ij} < d_s \\ 0 & r_{ij} > d_s \end{cases} \quad \rho_d(r_{ij}) = \begin{cases} C_d(d_d - r_{ij})^3 & r_{ij} < d_d \\ 0 & r_{ij} > d_d \end{cases} \quad (5.63)$$

$$\text{Embedding} \quad (5.64)$$

Parameter	Value
C_s	$0.05617 eV^2 \text{ang}^{-3}$
C_d	$0.1681 eV^2 \text{ang}^{-3}$
d_s	9.5097 angstroms
d_d	6.9189 angstroms
A_s	$2.417 \times 10^7 \text{ang}^{12}$
A_d	$3.7668 \times 10^6 \text{ang}^{12}$

Table 5.3: Caesium 2BEAM parameters

The implementation of this two-band potential predicted the transformation of Caesium. The I phase, at ambient pressure, is BCC Caesium with a primitive cell volume of 115.9 cubic angstrom per atom. As more pressure is added, the optimum structure changes from BCC to FCC, and this results in a smaller volume per atom of 67.5 cubic angstrom. Finally Caesium undergoes an isostructural transformation, and the potential predicts a volume of 48.7 cubic angstrom per atom.

There is a transition pressure of 4.3 GPa between the phases II and III. The potentials developed by Ackland and Reed were “in good agreement with experiment”[[twobandackland](#)].

An alloy version of the two-band model was developed by Olsson et al. to investigate the α -prime phase formation in Fe-Cr[[olssonfecr](#)]. Fe-Cr alloys form ferromagnetic alloys with concentrations of up to 10% chromium at 750°C. As the concentration of chromium in the alloy increases, the alloy begins to decompose into iron rich and chromium rich precipitates, and this decomposition is accelerated under irradiation.

The two-band method for Caesium was extended to an Fe-Cr alloy in order to describe the heat of mixing in the alloy.

$$U_{EAM} = \frac{1}{2} \sum_{i=1}^N \sum_{j \neq i}^N V_{ij}(r_{ij}) + \sum_{i=1}^N F_D[\rho_{d,i}] + \sum_{i=1}^N F_S[\rho_{s,i}] \quad (5.65)$$

where $\rho_{d,i} = \sum_{j=i, j \neq i}^N \rho_{d,ij}(r_{ij})$ and $\rho_{s,i} = \sum_{j=i, j \neq i}^N \rho_{s,ij}(r_{ij})$

The embedding functional (eq. ??) was in the form of several functionals used in papers by Ackland and Mendelev, and an extension to the standard Finnis-Sinclair.

$$F_{band}(\rho_{band}) = A_1^{band} \sqrt{\rho_{band}} + A_2^{band} \rho_{band}^2 + A_3^{band} \rho_{band}^4 \quad (5.66)$$

The choice of function for both the pair and d-band density functions was a cubic spline, and a 4s Slater type function was used for the s-band alloy density. The Fe-Fe and Cr-Cr s-band density functions were zero functions. Where the alloy has high concentrations of Iron or Chromium, the respective d-band density functions will dominate, but as the elements mix, the s-band density will also contribute.

$$V(r) = \sum_i a_i (r - r_i)^3 H(r_i - r) \text{ where } H \text{ is the Heaviside Step function} \quad (5.67)$$

$$\phi_d^{CrCr}(r) = \sum_k b_i (r - r_k)^3 H(r_k - r) \text{ where } H \text{ is the Heaviside Step function} \quad (5.68)$$

$$\begin{aligned} \phi_s^{FeCr}(r) &= (H_s r^3 \exp(-\xi_s r))^2 \\ \phi_s^{FeFe}(r) &= 0.0 \\ \phi_s^{CrCr}(r) &= 0.0 \end{aligned} \quad (5.69)$$

The resulting potential, with the s-density fitted to the mixing enthalpy of Iron and Chromium, reproduces the formation of α -prime phase Cr with thermal ageing over a range of Cr concentrations.

The Fe-Cr potentials were further developed by Bonny et al. The mixing enthalpy changes sign in Fe-Cr, having a positive mixing enthalpy for Cr concentrations above 10% and a negative mixing enthalpy below. This results in the solubility of Cr in the alloy at lower concentrations, but as the concentration rises there's a tendency for Cr to form α -prime precipitates [bonnyfecr].

In the work by Bonny et al, the base Iron and Chromium potentials were those developed by Mendelev and Ackland, and from the Fe-Cr potentials of Olsson and Wallenius. In total, 11 functions make up the Bonny et al potential, higher than the usual 7 functions required for a two species EAM. In a standard EAM potential, the density contribution from an atom of one species is only dependent on that contributing atom, and not the embedded atom. This potential splits the density function into multiple bands and multiple permutations of atom species.

$$\begin{aligned}
\rho_{AA}^d(r) &= \rho_{BA}^d = \rho_A^d \\
\rho_{BB}^d(r) &= \rho_{AB}^d = \rho_B^d \\
\rho_{AB}^s(r) &= \rho_{BA}^s \\
\rho_{AA}^s(r) &= \rho_{BB}^s = 0
\end{aligned} \tag{5.70}$$

The chosen s-band density function for the Bonny et al Fe-Cr alloy was selected as an exponential style function with a cut-off function.

$$\rho_{FeCr}^s(r) = kr^6 \exp(-2\xi r) g_{cut}(r) \tag{5.71}$$

$$g_{cut}(r) = \begin{cases} 1 & r \leq r_c^i \\ \frac{1}{2} \left(1 - \sin\left(\frac{\pi}{2} \frac{r-r_m}{d}\right) \right) & r_c^i < r < r_c^f \\ 0 & r_c^f < r \end{cases} \tag{5.72}$$

$$F^s(\rho) = A_1\sqrt{\rho} + A_2\rho^2 \tag{5.73}$$

The magnetic properties of Chromium were considered during the development of these potentials. First-Principles calculations are equivalent to calculating properties at 0K, and at this temperature Chromium is antiferromagnetic. The Neel temperature for Cr, the point at which it transitions from an antiferromagnetic to a paramagnet, is 310K. The operating temperature of the alloys, within a reactor, will be above the Neel temperature. Chromium has a positive Cauchy pressure as a paramagnet, and a negative Cauchy pressure under the Neel temperature when an antiferromagnetic, and as a result of this and the operating temperature, a positive Cauchy pressure was used to fit the potential.

Modified embedded-atom method

All the potential types considered so far are spherically symmetrical about the atom. Typically covalent bonds tend to be directional but metallic bonds, in contrast, are isotropic about each atom. However, in alloys and magnetic materials where the system is not isotropic, the modified embedded atom method may be used.

$$U_{MEAM,i} = \frac{1}{2} \sum_{j \neq i}^N V_{ij}(r_{ij}) + F_i(\vec{\rho}_i) \tag{5.74}$$

The original form for the embedding functional is given below (eq. ??)[semiempiricalpots].

$$F(\vec{\rho}) = AE_{coh} \frac{r\vec{\rho}}{\vec{\rho}^0} \ln \left(\frac{\vec{\rho}}{\vec{\rho}^0} \right) \tag{5.75}$$

The electron density is made from four contributing functions. The first, ρ^0 , is not dependent on direction, but ρ^1 , ρ^2 and ρ^3 are dependent on the angle.

$$\begin{aligned}
\rho^0 &= \sum_i^N \rho_i^0(r^i) \\
(\rho^1)^2 &= \sum_{\alpha} \left(\sum_i \rho_i^1(r^i) \frac{r_{\alpha}^i}{r^i} \right)^2 \\
(\rho^2)^2 &= \sum_{\alpha} \left(\sum_i \rho_i^2(r^i) \frac{r_{\alpha}^i}{r^i} \frac{r_{\beta}^i}{r^i} \right)^2 - \frac{1}{3} \left(\sum_i \rho_i^2(r^i) \right)^2 \\
(\rho^2)^2 &= \sum_{\alpha} \left(\sum_i \rho_i^2(r^i) \frac{r_{\alpha}^i}{r^i} \frac{r_{\beta}^i}{r^i} \frac{r_{\gamma}^i}{r^i} \right)^2 - \frac{3}{5} \left(\sum_{\alpha} \frac{r_{\alpha}^i}{r^i} \rho_i^3(r^i) \right)
\end{aligned} \tag{5.76}$$

The partial electron densities may be combined as is eq. ??[semiempiricalpots].

$$\begin{aligned}
\vec{\rho}_i &= \rho_i^{(0)} \cdot 2 / (1 + \exp(-\Gamma_i)) \\
\Gamma_i &= \sum_{h=1}^3 t^{(h)} \left[\rho_i^{(h)} / \rho_i^{(0)} \right]^2 \\
\rho^{a(h)}(R) &= \exp(-\beta^{(h)}(R/r_e - 1))
\end{aligned} \tag{5.77}$$

This form of potential is implemented in LAMMPS and other molecular dynamics codes. It is more applicable to materials with bonds that depend on their angle, but it may have useful applications to metals where this is not as pronounced (if at all).

5.3.4 Function Types used by EAM and Two-Band EAM

In previous work, there are a wide range of functions used to represent the pair potential, density and embedding functional. These range from those that preserve and attempt to replicate the physics, to those that do away with knowledge of the physics underlying the potentials altogether. The pair potentials already covered here may also be used as the pair function component of the EAM or Two-Band EAM potentials.

A full list of the functions considered and included in the potential fitting code that resulted from this work is included in appendix ???. Only polynomial splines will be discussed further here.

Polynomial Splines

The form of polynomial spline used in the literature is a sum of N cubic polynomials that, by way of the Heaviside step function and their form, cutoff neatly at the desired radius. The cutoff radii are fixed and, during the fit of a potential, just the coefficients of each cubic spline are varied (eq. ??).

$$\begin{aligned}
V(r) &= \sum_i^N a_i (r - r_i)^3 H(r_i - r) \\
H(x) &= \begin{cases} 0 & x < 0 \\ 1 & x \geq 0 \end{cases} \quad \text{where}
\end{aligned} \tag{5.78}$$

If a continuous second derivative is required the cubic spline may be replaced with a quintic spline (eq. ??).

$$V(r) = \sum_i^N a_i (r - r_i)^5 H(r_i - r) \quad (5.79)$$

Polynomial Knot to Knot Splines

So far, analytic potentials have been discussed. There are existing potentials that do not have an analytic form, but are tabulated data that have the properties that they are continuous and have a continuous first derivatives. In attempting to fit or re-fit tabulated data, it would be problematic to adjust each data point individually given the number of data points and the requirement to have a continuous well behaved function with continuous first derivatives.

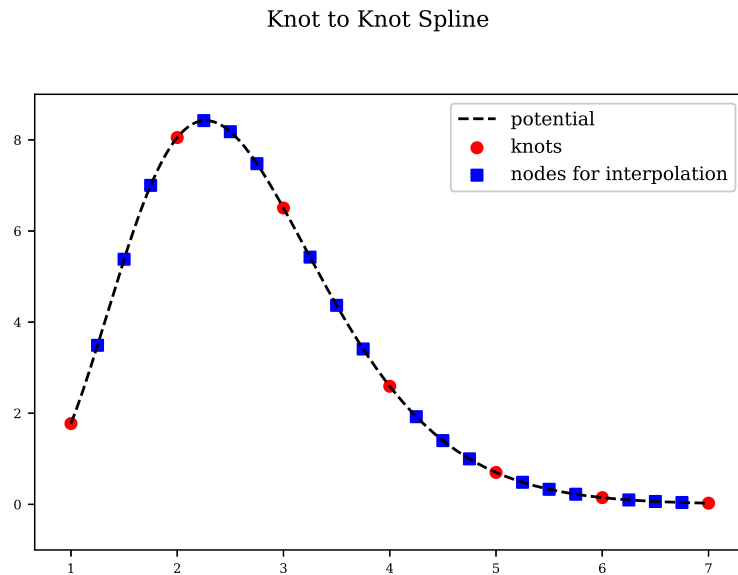


Figure 5.7: Polynomial knot to knot spline

The tabulated function is divided into sections, and the start and end of each section forms the knot of the spline. A polynomial may be splined between these knots, but the order of polynomial will depend on the data available. Immediately, the x and y positions are known: $x_a, x_b, f(x_a), f(x_b)$. A first order polynomial has two unknowns, and so these unknowns may be calculated using linear algebra.

$$\begin{aligned} c_0 + c_1 x_a &= y_a \\ c_0 + c_1 x_b &= y_b \end{aligned} \quad (5.80)$$

One of the requirements for the potential is to have a continuous first derivative, and this requires knowledge of the first derivative at each knot. In the figure, the knots are shown as circles. By taking several points near to each knot, shown as squares, the derivative at each knot may be calculated by interpolation. This allows a third order polynomial to be used (eq. ??).

$$\begin{aligned}
P_1 &= (x_A, f(x_A)) \\
P_2 &= (x_A, f'(x_A)) \\
P_3 &= (x_B, f(x_B)) \\
P_4 &= (x_B, f'(x_B))
\end{aligned} \tag{5.81}$$

$$\begin{aligned}
c_0 + c_1 x_a + c_2 x_a^2 + c_3 x_a^3 &= y_a \\
0 + c_1 + 2c_2 x_a + 3c_3 x_a^2 &= y'_a \\
c_0 + c_1 x_b + c_2 x_b^2 + c_3 x_b^3 &= y_b \\
0 + c_1 + 2c_2 x_b + 3c_3 x_b^2 &= y'_b
\end{aligned} \tag{5.82}$$

Rewriting as matrices:

$$\begin{bmatrix} 1 & x_a & x_a^2 & x_a^3 \\ 0 & 1 & 2x_a & 3x_a^2 \\ 1 & x_b & x_b^2 & x_b^3 \\ 0 & 1 & 2x_b & 3x_b^2 \end{bmatrix} \begin{bmatrix} c_0 \\ c_1 \\ c_2 \\ c_3 \end{bmatrix} = \begin{bmatrix} f(x_a) \\ f'(x_a) \\ f(x_b) \\ f'(x_b) \end{bmatrix} \tag{5.83}$$

It is important for the function and its derivative to be continuous. If it is also deemed necessary to have a continuous second derivative, a quintic spline may be used. By interpolating and calculating the second order derivative at each knot, a 5th order polynomial may be splined between pairs of knots.

This approach may be modified to spline functions of the form $\exp(p(r))$ between knots, and this is useful for splining between a ZBL or similar repulsive function at small r and a function of a different form at larger r.

where

$$V(r) = \begin{cases} ZBL(r, q_1, q_2) & r \leq r_a \\ \exp(a + br + cr^2 + dr^3) & r_a < r < r_b \\ v(r) & r_b < r < r_{cut} \\ 0 & r \geq r_{cut} \end{cases} \tag{5.84}$$

To spline the exponential the equations are set up in a similar way, but this time the system of equations are non-linear.

$$\begin{aligned}
\exp(c_0 + c_1 x_a + c_2 x_a^2 + c_3 x_a^3) &= y_a \\
(c_1 + 2c_2 x_a + 3c_3 x_a^2) \exp(c_0 + c_1 x_a + c_2 x_a^2 + c_3 x_a^3) &= y'_a \\
\exp(c_0 + c_1 x_b + c_2 x_b^2 + c_3 x_b^3) &= y_b \\
(c_1 + 2c_2 x_b + 3c_3 x_b^2) \exp(c_0 + c_1 x_b + c_2 x_b^2 + c_3 x_b^3) &= y'_b
\end{aligned} \tag{5.85}$$

Newton-Gauss is used to solve this problem where initial parameters are set for the constants in the equation and varying until the function values and derivatives at point A and point B match the values being fitted to.

Tending to Zero at the Cutoff Radius

It is desirable for the functions to be well behaved and continuous. The coulomb force between two charged particles reduces smoothly until theoretically at an infinite separation; it doesn't reach a set separation and abruptly drop to zero. It is impossible and unhelpful to consider a very large or infinite separation which is why the cutoff radius has been introduced. It represents the separation where the potential has reached zero; at the very least it's a trade off between accuracy and the computing time available for the problem.

The pair potential should therefore drop off to 0 at the cut off radius, and be equal to zero for larger separations. The electron density spherically around an atom should also smoothly drop off to zero, and similarly it should be equal to zero for distances larger than the cut off. The embedding energy is dependent on the density at the location of the atom embedded. The embedding function will not necessarily drop off to zero, and it depends on the density and not the separation.

In a molecular dynamics simulation, the neighbour list will usually be built considering atoms slightly more separated than the cut off radius of the functions. This allows the same neighbour list to be used for several time steps, before the need to update as atoms will get closer and further apart with each time step.

Collisions and Interatomic Potentials

In a simulation at room temperature the average energy of the atoms in the simulation are approximately 0.05eV, and at temperatures near the melting point of iron the energy is approximately 0.2eV. These are energy ranges that interatomic potentials are designed to operate in, but in typical damage cascades in nuclear core components the atoms in the cascade, including the PKAs, have energies up to approximately 100KeV.

If a potential is not designed for use in collision simulations, it may not contain the data points required for such close separations. If a potential, such as the Buckingham potential (section ??), is used, the energy peaks at a certain separation and then drops once more. This would cause colliding atoms to stick to one another once they reached a certain separation.

The ZBL function is designed specifically with collisions in mind and should be used in MD simulations that involve collisions. In simulations of BCC tungsten[[tungstenfikarschaublin](#)], the material had an initial temperature of 10K and 523K with PKAs energies at 10keV, 20keV and 50keV. The models were simulated with MOLDY using an EAM potential where the pair potential is splined to a ZBL for short range interactions.

5.3.5 Sheng EAM Potentials

A set of potentials have been derived by Sheng et al[[shengeam](#)] and are available to download in tabulated form[[shengeamonline](#)]. They were created using a modified version of the PotFit code by P. Brommer and F. Gähler[[pbrommer](#)]. The code had been modified extensively to include quintic spline interpolation, phonon calculation, elastic constant calculation and optimization techniques[[shengeamonline](#)]. The potentials (typically) used 15 knot splines for pair and density functions and 6 knot splines for the embedding functional for each element, but the potentials were published as tabulated functions. Potentials for fourteen FCC metals were derived in the first instance, but more (including alloys) are available on the website. Unfortunately, the (Sheng et al.) modified PotFit code is not available through the PotFit website[[pbrommer](#)], and the latest version of their code has moved on since 2011.

5.3.6 Calculating Energy, Force and Stress

Molecular dynamics simulations do not need to include the weak or strong force, and the gravitational force between atoms in the simulated material are so weak in comparison to the electromagnetic force, they can

also be ignored. There is a force between all the atoms within a real material, but the electromagnetic force is inversely proportionally to the separation of the atoms. Above a certain separation, the electromagnetic force can also be ignored, in order to simplify the computation.

Neighbour List

A cut off radius can be introduced to limit the number of neighbours (section ??). As the lattice parameter decreases, the atoms are brought closer together, and as the cut off radius is increased more atoms are considered to be within the sphere of influence of one another. Both increase the number of neighbours each atom has (fig. ??).

Building a neighbour list may take a long time, depending on the parameters. If a simplistic approach is taken, for N atoms in the supercell, there will be $27N^2$ checks between atoms to see whether they are within the cut off radius of one another. For larger numbers of atoms in a supercell, the whole may be decomposed into smaller domains.

For example, a $16 \times 16 \times 16$ FCC supercell, containing 16,384 atoms, would require looping $27 \times 16,384^2 = 7.25 \times 10^9$ times. Breaking the supercell into 64 smaller domains with 256 atoms in each, reducing the problem to $64 \times 27 \times 256^2 = 1.13 \times 10^8$ loops.

For this work, the supercells used to calculate bulk properties from the interatomic potentials, and the configurations generated by DFT, contain fewer than 1,000 atoms, removing the need to decompose the configuration into smaller sub cells.

To build the neighbour list a halo configuration is created such that it lies on top of the real atoms, but extends at least as far as the cut off radius on each side of the real simulation box (fig. ??). Periodic boundary conditions are used to construct the halo.

Once the halo list is computed, the neighbour list may also be computed by looping through the real atoms and halo atoms. A simple pseudo coded sub routine is given (listing ??).

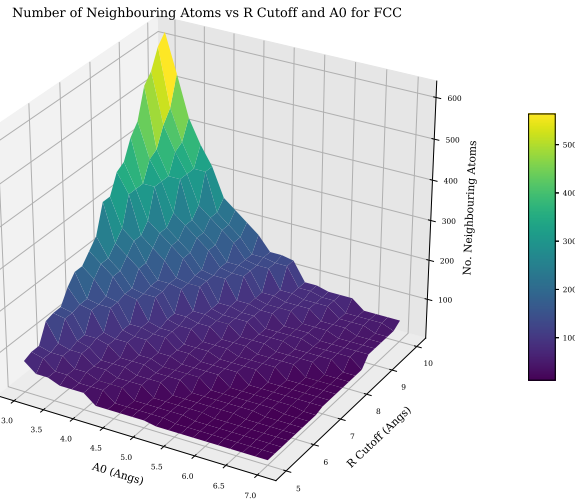


Figure 5.8: Neighbouring atom count dependant upon lattice parameter and cutoff radius

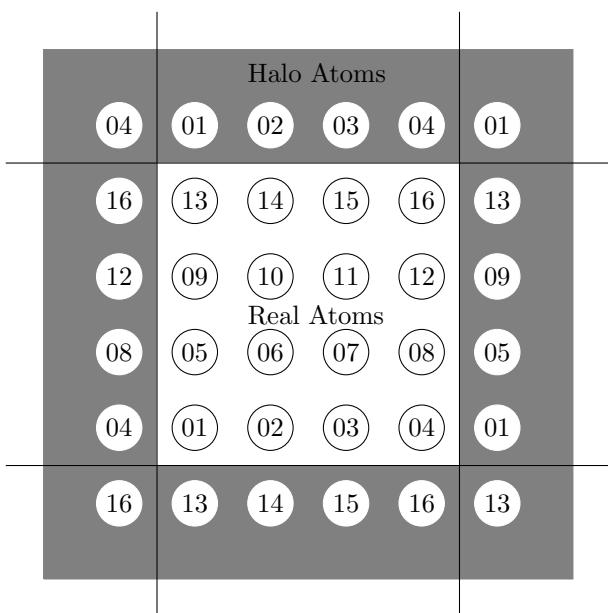


Figure 5.9: Atoms in simulation box with a halo of atoms at the boundary

Listing 5.1: Simple subroutine for generating a half size neighbour list

```

1 // real_atoms - array holding coordinates of all real atoms
2 // halo_atoms - array holding coordinates of all halo atoms
3 // real_ids - unique id for each atom
4 // halo_ids - unique atom ids for halo atoms
5 // nlist_ids - array to store ids
6 // nlist_r - array to store separation
7 // nlist_r - array to store separation
8
9 // Define the cutoff and counter start value
10 r_cut = 5.0
11 nl_counter = 1
12
13 // Calculate square
14 r_cut_sq = r_cut ** 2
15
16 // Loop over all real atoms
17 DO n_real = 1, real_atom_count
18   // Loop over all halo atoms
19   DO n_halo = 1, halo_atom_count
20     IF (real_ids(n_real) .LT. halo_ids(n_halo)) THEN
21       r(1:3) = halo_atoms(n_halo, :) - real_atoms(n_real, :)
22       r_sq = SUM(r(1:3) * r(1:3))
23       IF (r_sq .LE. r_cut_sq) THEN
24         r_mag = sqrt(r_sq)
25         nlist_ids(nl_counter, 1) = real_ids(n_real)
26         nlist_ids(nl_counter, 2) = halo_ids(n_halo)
27         nlist_r(nl_counter, 1) = r_mag
28         nlist_r(nl_counter, 2:4) = r(1:3)/r_mag
29         nl_counter = nl_counter + 1
30       END IF
31     END IF
32   END DO
33 END DO

```

The resulting list will contain unique pair combinations; i.e. the pair atom 1 and atom 2 will only be recorded once, and not also as atom 2 and atom 1.

Computing Total Energy

The total energy of the system is the sum of the individual energies for the atoms in the simulation. The type of atom (or pairs of atoms) will determine which function is used.

First, to compute the pair potentials:

- set the total energy of the system equal to zero
- set the starting energy for each atom in the system to zero
- loop through the atom pairs in the entire neighbour list
- for each atom pair, A and B, use the known separation and the potential function to compute the potential energy on atom A due to B and vice versa
- add this potential energy to both A and B
- after looping through the neighbour list, add all the energies due to the pair potential to the total energy

For an EAM or 2BEAM potential, the densities and embedding energies must also be computed:

- set the electron density at the position of (for each) atom to zero
- loop through the atom pairs in the entire neighbour list
- for each atom pair, using the density function for the atom A, the density at atom B due to atom A will be calculated and added to the density at atom B
- if the atoms are both of the same type the same density will be added to atom A due to atom B
- if the atom types are different, using the density function for the atom B, the density at atom A due to atom B will be calculated and added to the density at atom A
- following looping through the neighbour list, to calculate the densities at each atom, the list of atoms will be looped through
- for each atom, the density value at the position of that atom, will be input into the appropriate embedding function to calculate the embedding portion of the energy
- add all the embedding energies to the total energy of the system

For a 2BEAM potential, repeat the above procedure for the second group of density functions and embedding functions (do not repeat calculation of the pair potentials).

Computing Forces on Atoms

In order to calculate the forces on the atoms with an EAM or 2BEAM potential, the neighbour list and atom list will need to be looped through several times. First, the pair potential and force due to the pair potential must be calculated by a complete loop through the neighbour list. At the same time, the density at each atom location is also calculated. The embedding energy may then be computed by looping through all the atoms and using the electron density at each atom to give the energy of the atom embedded in that density. The third and final loop will run through the neighbour pairs in the neighbour list once more computing the force on each atom due to it's embedding.

The force on each atom, due to surrounding atoms, may be split into two; force due to the pair potential, and the force due to the embedding of the atom[[dlpolymanual](#)].

$$F_{pair}^k = - \sum_{j=1, j \neq k}^N \frac{\partial V_{kj}(r_{kj})}{\partial r_{kj}} \frac{\vec{r}_{kj}}{|\vec{r}_{kj}|} \quad (5.86)$$

$$F_{embed}^k = - \sum_{j=1, j \neq k}^N \left(\frac{\partial F}{\partial \rho_k} + \frac{\partial F}{\partial \rho_j} \right) \frac{\partial \rho(r_{kj})}{\partial r_{kj}} \frac{\vec{r}_{kj}}{r_{kj}}$$

Computing Stress

The stress is to be calculated assuming the system is at 0K[[wikivirialstress](#)] so the virial stress equation is eq. ??.

$$\tau_{ij} = \frac{1}{2V} \sum_{k,l \in V} \left(x_i^{(l)} - x_i^{(k)} \right) f_j^{(kl)} \quad (5.87)$$

Within the computer code, the individual force components between pairs of atoms are stored as well as an equal sized array of vectors representing their spatial separation. Those pairs with one atom in the halo around the simulation box are used to calculate the stress on the simulation box.

Pseudo Code for the Energy, Force and Stress Subroutine

The calculation requires several arrays to temporarily store data. The electron densities and gradients of the density function are stored for multiple groups of densities and embedding functionals. The overall forces on each atoms also need to be stored as well as the force between pairs of atoms, as this is required to compute the virial stress. The Fortran code to compute this is included in the appendix (section ??) and a pseudocode in listing ?? explains the process.

Listing 5.2: Pseudo Code for Energy and Stress Force Calculation

```
1
2 electron_density[1:n_atoms, 1:bands] = 0.0 // electron density at each atom
3 density_grad_ab[:, :] = 0.0           // grad density function
4 density_grad_ba[:, :] = 0.0           // grad density function
5 energy = 0.0                         // total energy
6 forces[:, :] = 0.0                   // forces each atom, 3D
7 force_between_pairs[:, :] = 0.0       // used to store force between pairs, for stress computation
8 stress[:, :] = 0.0DO
9
10 // LOOP 1 - Pair energy, force and calculate densities
11 DO n = 1, neighbour_count
12   E = get_PairEnergy(atom_a, atom_b, r[n,:])
13   F[:] = get_PairForce(atom_a, atom_b, r[n,:])
14
15   // Save energy
16   energy = energy + E
17
18   // Save Force
19   f[atom_a, :] = f[atom_a, :] - F[:]
20   f[atom_b, :] = f[atom_b, :] + F[:]
21   force_between_pairs[:, :] = force_between_pairs[:, :] - F[:] // Used to calculate stress
22
23 // Loop through density bands
24 DO band = 1, bands
25   // Electron density at A due to atom B
26   electron_density[atom_a, band] = get_Density(atom_b, r)
27   density_grad_ab[n, band] = get_DensityGradient(atom_b, r)
28
29   // Electron density at B due to atom A
30   electron_density[atom_a, band] = get_Density(atom_a, r)
31   density_grad_ba[n, band] = get_DensityGradient(atom_a, r)
32 END DO
33 END DO
34
35 // LOOP 2 - Embedding energy
36 DO n = 1, atom_count
37   // Loop through density bands
38   DO band = 1, bands
39     energy = energy + get_EMBEDDINGEnergy(n, band)
40   END DO
41 END DO
42
43 // LOOP 3 - Embedding force
44 DO n = 1, neighbour_count
45   // Loop through density bands
46   DO band = 1, bands
47     epA = get_EMBEDDINGGradient(atom_a, electron_density(atom_a, b))
48     epB = get_EMBEDDINGGradient(atom_b, electron_density(atom_b, b))
49
50     F[:] = (epA * density_grad_ba(n, band) + epB * density_grad_ab(n, band)) * r[n, :]
51
```

```

52     f(atom_a, :) = f(atom_a, :) - F[:,]
53     f(atom_a, :) = f(atom_a, :) + F[:,]
54
55     force_between_pairs[n,:] = force_between_pairs[n,:] - F[:] // Used to calculate stress
56 END DO
57 END DO
58
59 // LOOP 4 STRESS
60 DO n = 1, neighbour_count
61   // Only compute if the second atom is in the halo
62   IF(nlisthalo(n))THEN
63     DO i = 1,3
64       DO j = 1,3
65         stress[i,j] = stress[i,j] + (r[n, i] * force_between_pairs[n,j])
66     END DO
67   END DO
68 END IF
69 END DO
70 stress[1:3, 1:3] = stress[1:3, 1:3] / (2.0 * volume)

```

5.3.7 Choice of Functions and Functionals

The EAM potential, for n elements, is made up of n pair functions, $n(n+1)/2$ density functions and $n(n+1)/2$ embedding functionals. The choice of function varies greatly. Irrespective of the choice of function, there are a number of desireable properties:

- the function should be well behaved
- this should be true for the derivative and second derivative - ideally, these should be continuous too
- the pair and density functions should have a cutoff, and the value at this cutoff should be zero

ZBL to Pair Function Spline

Certain functions may behave oddly at small values of atom seperation, and this can be seen for the Buckingham potential, where the potential may drop sharply to negative values, pulling the modelled atoms together. The ZBL function is a good choice to model higher energy atoms that do come close together. It may be desireable to keep the characteristics for the

A One Time Neighbour List

As there are only static calculations in this work, the neighbour list will only need to be computed once. The potential functions will change during the fitting process, but the configuration, and neighbourlist, is frozen in place from the start to the end of the fitting procedure.

5.3.8 Sacrificing Physical Elegance

We have no knowledge of a formula that can be applied to any material and describe the energy and forces between atoms exactly. Even first priciples calculations rely of approximations, and the knowledge of an exact exchange functional eludes us. While it would be satisfying to derive a potential that reflects the fundamental physics, it may be something that is forever out of our reach.

It is more useful to develop a potential that replicates the behavior of DFT calculations (matches the forces, energies, stresses etc) and reproduces material properties such as its elastic constants. If it can do this, and give insights into the material in a way that is not yet possible experimentally, does it matter if the physical elegance is lost?

5.4 Force Matching

To derive a potential, one may approach the problem from first principles in an attempt to replicate reality. It has been more useful, however, to lose any physical elegance [**twobandackland**] to give potentials that work for specific elements under certain conditions. Force data, gathered experimentally or by first-principles calculations, has been used to develop potentials since the 1990s. The force matching method was developed in 1994 by Ercolessi and Adams [**forcematchingmethod**] to link the more accurate, more processor and memory intensive, world of first-principles calculations to Molecular Dynamics.

The force-matching method uses the difference between the actual force (either measured experimentally or calculated by first-principles calculations)

Given a set of M different atomic configurations, and a potential with a set of L parameters (\vec{p}), the function Z_F is a measure of the difference between the the forces calculated using the potential for all configurations and the actual (or DFT generated) forces.

$$Z_F(\vec{\alpha}) = \sum_{k=1}^M \sum_{i=1}^k \sum_{j=1}^3 |\vec{F}_{i,j}^k(\vec{\alpha}) - \vec{F}_{i,j}^0|^2 \quad (5.88)$$

This may be extended to include the calculation of other properties:

- Lattice Parameter a_0
- Cohesive Energy E_{coh}
- Bulk Modulus B_0
- Equation of State (E_0, V_0, B_0, B_0^p)
- Stress Tensor
- Elastic Constants
- Shear Modulus, Young's Modulus, Poisson Ratio
- Melting Temperature
- Surface Energy

Each may be weighted depending on how important the property is to the simulation the potential is required for.

$$Z(\vec{p}) = w_F Z_F(\vec{p}) + w_{b0} Z_{b0}(\vec{p}) + w_{e0} Z_{e0}(\vec{p}) + w_{a0} Z_{a0}(\vec{p}) + w_{ec} Z_{ec}(\vec{p}) + w_{coh} Z_{coh}(\vec{p}) \quad (5.89)$$

The result is a residual squared sum that measures how well or poorly a potential fits the required data.

5.5 Magnetism

5.5.1 Brief History of Magnetism

Magnetism as a phenomenon has been known to our civilisation for thousands of years. The magnetic mineral Lodestone contains the iron oxide Magnetite Fe_3O_4 and it was used by the ancient Greeks over two thousand years ago.

The magnetic compass had been used since the 12th century, but it wasn't until the 17th Century that the Earth was discovered as a magnet itself by William Gilbert.

In the early 1800s, Hans Christian Oersted discovered that an electric current could move a compass needle, and this lead to much research into the connection between electricity and magnetism. Experimental work by Michael Faraday lead to the discovery that a changing magnetic field produces an electric field. By the mid-1800s the mathematical physicist, James Clerk Maxwell, derived his set of equations describing the connection between magnetism and electricity.

$$\partial \cdot \vec{E} = \frac{\rho}{\epsilon_0}$$

$$\nabla \cdot \vec{B} = 0$$

$$\nabla \times \vec{E} = -\frac{1}{c} \frac{\partial \vec{B}}{\partial t}$$

$$\nabla \times \vec{B} = \frac{1}{c} \left(4\pi \vec{J} + \frac{\partial \vec{E}}{\partial t} \right)$$

5.5.2 Magnetism: Moving Charges and Spin

General Relativity and Quantum Mechanics were invented as theories to solve anomalies in science during the first part of the 20th Century, and they describe the very large and very small realms we do not notice in every day life. In describing how magnetism comes to be, it may be useful to use classical analogies, but that's all they are. Quantum Mechanics is required and this replaces intuition with a mathematical description.

$$\vec{B} = \frac{\mu_0 q}{4\pi r_{ij}^3} \vec{v} \times \vec{r}_{ij} \quad (5.90)$$

When a charged particle moves, it creates a magnetic field. The field at some point j created by a charge moving at \vec{v} at point i is calculated (eq. ??). Electrons do not orbit around a nucleus in the classical sense, but they do have an orbital angular momentum. The overall magnetic field created by an atom is made up of:

- orbital angular momentum of the electron
- spin of electrons
- spin of nucleons

The contribution of the nucleus to the magnetic field is small, and the orbital component and spin component of electrons are mostly responsible.

Spin is a property of quantum mechanics and it doesn't have an equivalent in classical mechanics, although it may be thought of similar to a spinning top or a rotating planet. Electrons are point like particles, and do not actually rotate, but they do have an intrinsic angular moment (spin). Where a spinning top might have a range of angular velocities, electrons have a quantised value and, as fermions, they have half integer spin.

5.5.3 Ferromagnetism, Antiferromagnetism and Hund's Rule

Electrons fill the shells of a ground state atom such that the energy is minimised. Four quantum numbers are used to describe electrons bound to an atom: n , l , m_l and m_s . The Pauli exclusion principle states that the electrons, which are fermions, cannot have the same quantum numbers as another electron bound to that atom.

Electrons may be spin up or spin down thus two electrons can have the same n , l , m_l with two values for m_s available. The energy is minimised by not pairing up and down electrons until all the free slots due to the coulomb interaction between the electrons. Once each slot contains one electron, they begin to pair.

The electronic configuration of Iron highlights this:

$$\begin{array}{ll}
 1s^2 & \underline{\uparrow\downarrow} \\
 2s^2 & \underline{\uparrow\downarrow} \\
 2p^6 & \underline{\uparrow\downarrow} \quad \underline{\uparrow\downarrow} \quad \underline{\uparrow\downarrow} \\
 3s^2 & \underline{\uparrow\downarrow} \\
 3p^6 & \underline{\uparrow\downarrow} \quad \underline{\uparrow\downarrow} \quad \underline{\uparrow\downarrow} \\
 4s^2 & \underline{\uparrow\downarrow} \\
 3d^6 & \underline{\uparrow\downarrow} \quad \underline{\uparrow} \quad \underline{\uparrow} \quad \underline{\uparrow} \quad \underline{\uparrow}
 \end{array} \tag{5.91}$$

Rather than fill the 3d shell from left to right, the first five slots take electrons with spin in the same direction, and the remaining electron fills the first slot with spin opposite to the first five electrons.

Being fermions the wavefunction for the two electrons must be antisymmetric, with spins opposite to one another. Electrons with the same spin will repel one another and this causes an increase in the screening between the electrons and the nucleus. The screening lowers the attraction between the electrons and the nucleus that then results in the total energy of the atom decreasing[[aligning electrons](#)].

Chromium

$$\begin{array}{ll}
 4s^1 & \underline{\uparrow} \\
 3d^5 & \underline{\uparrow} \quad \underline{\uparrow} \quad \underline{\uparrow} \quad \underline{\uparrow} \quad \underline{\uparrow}
 \end{array} \tag{5.92}$$

Iron

$$\begin{array}{ll}
 4s^2 & \underline{\uparrow\downarrow} \\
 3d^6 & \underline{\uparrow\downarrow} \quad \underline{\uparrow} \quad \underline{\uparrow} \quad \underline{\uparrow} \quad \underline{\uparrow}
 \end{array} \tag{5.93}$$

Cobalt

$$\begin{array}{ll}
 4s^2 & \underline{\uparrow\downarrow} \\
 3d^7 & \underline{\uparrow\downarrow} \quad \underline{\uparrow\downarrow} \quad \underline{\uparrow} \quad \underline{\uparrow} \quad \underline{\uparrow}
 \end{array} \tag{5.94}$$

Nickel

$$\begin{array}{ll}
 4s^2 & \underline{\uparrow\downarrow} \\
 3d^8 & \underline{\uparrow\downarrow} \quad \underline{\uparrow\downarrow} \quad \underline{\uparrow\downarrow} \quad \underline{\uparrow} \quad \underline{\uparrow}
 \end{array} \tag{5.95}$$

In pure Iron (eq. ??), under normal conditions, it is energetically favourable for the atoms to align in the same direction, and as such iron is ferromagnetic. Cobalt (eq. ??) has a face centered tetragonal structure at room temperature. It has a similar electronic structure to iron, but has three unpaired electrons in the 3d shell rather than four. It is a ferromagnetic whilst it remains in its CPH form. Nickel (eq. ??) is also ferromagnetic, but it is ferromagnetic in its FCC phase.

In its gamma phase, as it is in austenitic stainless steel, iron atoms align opposite to one another in an antiferromagnetic arrangement. This is also the same for BCC chromium (eq. ??) which is antiferromagnetic in its pure form under normal conditions.

5.6 Density Functional Theory

Acrlfulldft is a branch of quantum chemistry that approximately solves the Schrödinger equation using electron density, rather than the coordinates of each electron in the system. A number of simplifications are also applied in order for DFT to be practical to use, but despite this calculations are limited to just hundreds or thousands of atoms. A calculation of a hundred or so atoms may take thousands of CPU hours at the time of writing, depending on the type of calculation and complexity of the electron structures of the atoms involved.

It is through acrshortdft that the first principles energy, stress and force calculations will be made, and it's these results that the EAM potentials will be trained and fit to using the force matching method. This will allow much larger scale modelling using the extrapolated behaviour of accurate DFT calculations.

5.6.1 Brief Overview of DFT

Several important theories and approximations are used by DFT with the aim of calculating and minimising energies and forces. The Born-Oppenheimer approximation separates the electron-nucleus wave function. It treats the nuclei as fixed points, and the system of electrons in a fixed potential created by the nuclei.

The DFT of Kohn, Sham and Hohenberg proved that the potential of a system is uniquely determined by its ground state density. This makes solving the Schrödinger equation significantly easier.

5.6.2 Time Independent Schrödinger Equation

The Schrödinger equation is a linear partial differential wave equation and it was proposed by Erwin Schrödinger in 1925. There is a time-dependent and time-independent form of the equation. As the DFT calculations in this work are static only the time-independent version will be discussed.

$$\hat{H}|\Psi\rangle = E|\Psi\rangle \quad (5.96)$$

The Hamiltonian \hat{H} is an operator and it is the total energy in the system. Ψ is the wave function (for example, the wave function of an electron) and this contains all the measurable information possible about whatever it represents. E is the energy eigenvalue of this system and this will depend on the eigenstate of the system. The wave function is also connected to the probability of a particle being found at a certain point in space, and the integral over all space is equal to 1 i.e. the probability of it being found somewhere in space is equal to 1 (eq. ??).

$$\int_{-\infty}^{\infty} \int_{-\infty}^{\infty} \int_{-\infty}^{\infty} \Psi(x, y, z) dx dy dz = 1 \quad (5.97)$$

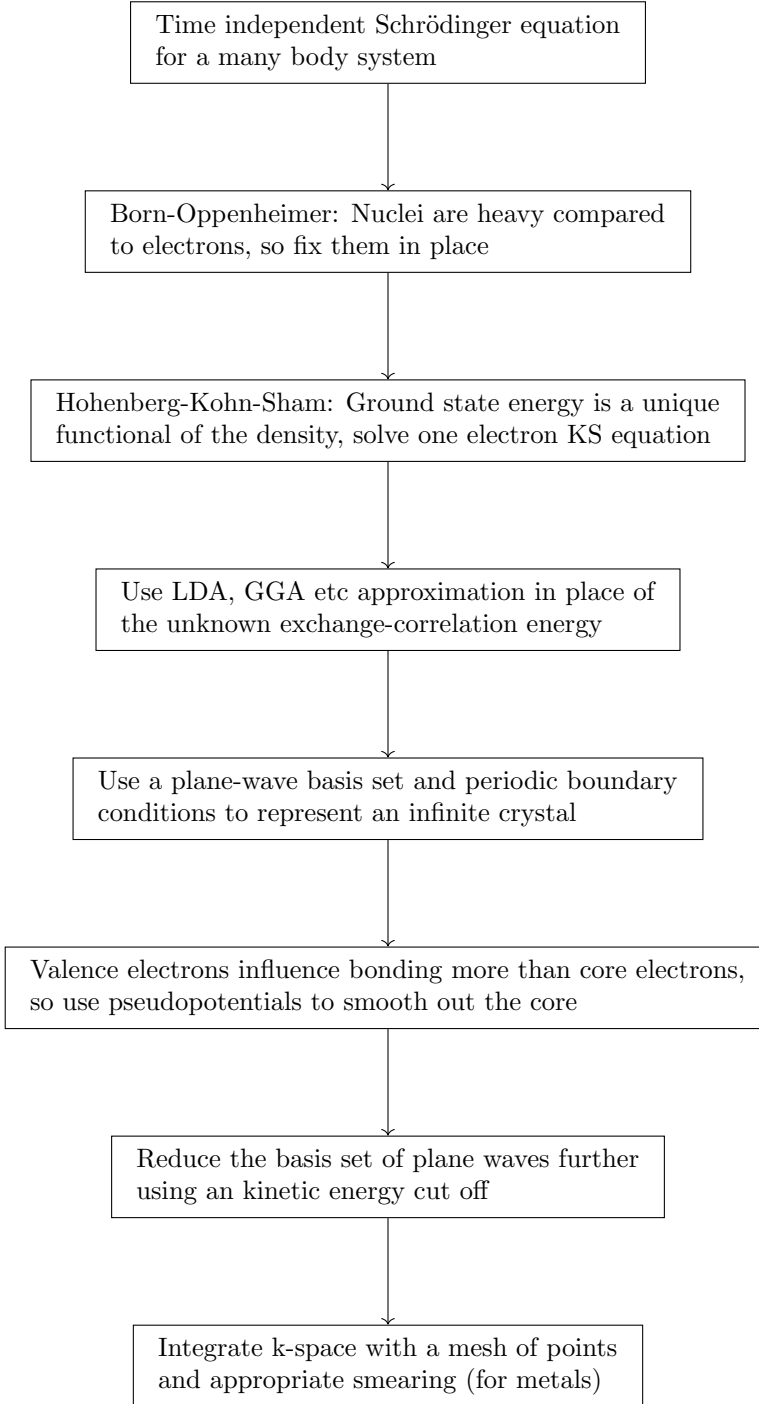


Figure 5.10: Common approximations used to enable DFT calculations

The Schrödinger equation is set up depending on the system being studied. Starting with the simplest, a free particle, the only non zero energy of the Hamiltonian is kinetic.

$$\hat{H} = \frac{\hbar^2}{2m} \nabla^2 - \frac{\hbar^2}{2m} \nabla^2 \Psi(\vec{r}) = E\Psi(\vec{r}) \quad (5.98)$$

If the particle is in a potential, it will have both kinetic energy \hat{T} and potential energy \hat{V} (eq. ??).

$$\hat{H} = \hat{T} + \hat{V} = \frac{\hbar^2}{2m} \nabla^2 + V(\vec{r})$$

$$\left[-\frac{\hbar^2}{2m} \nabla^2 \right] \Psi(\vec{r}) = E\Psi(\vec{r}) \quad (5.99)$$

5.6.3 Many Body TISE

Electronic structure calculations are important and allow the calculation of material properties that may be difficult or impossible to measure with current technology. The next step towards this is to set up the Schrödinger equation (time-independent) for nuclei and electrons in a crystal.

Relative to the strong force, the electromagnetic force is 1/137th as strong, but the strong force acts over a range of approximately 1.0×10^{-5} angstrom. In the calculations carried out in this section, the atoms will never be arranged close enough for the strong force to be considered at all. The gravitational force, as with the electromagnetic force, acts over an infinite range. The electromagnetic force is more than 1.0×10^{36} times greater than the gravitational force, so it too can be neglected. Finally, the weak interacting force has a range of approximately 1.0×10^{-8} angstrom which, as with the strong force, is a range small enough that the weak force may be neglected.

The energy operators required are kinetic and electromagnetic potential (eq. eq:TimeIndependentSchrodinger3).

$$\hat{H} = \hat{T}_e + \hat{T}_n + \hat{V}_{e-e} + \hat{V}_{e-n} + \hat{V}_{n-n} \quad (5.100)$$

The first two terms are the kinetic energy of the electrons and nuclei respectively (eq. eq:TimeIndependentSchrodinger4).

$$\hat{T}_e = -\sum_i \frac{\hbar^2}{2m} \nabla^2 \text{Sum of kinetic energy of electrons}$$

$$\hat{T}_n = -\sum_k \frac{\hbar^2}{2M} \nabla^2 \text{Sum of kinetic energy of nuclei} \quad (5.101)$$

The last three terms are potential energy terms due to the electromagnetic force (eq. eq:TimeIndependentSchrodinger5).

$$V_{e-e} = \frac{1}{2} \sum_{i,j, i \neq j} \frac{1}{|\vec{r}_i - \vec{r}_j|} \text{sum of potential energy between electrons}$$

$$V_{e-n} = \sum_{i,k} \frac{z_i}{|\vec{r}_i - \vec{r}_l|} \text{sum of potential energy between electrons and nuclei} \quad (5.102)$$

$$V_{n-n} = \frac{1}{2} \sum_{k,l, k \neq l} \frac{z_k z_l}{|\vec{r}_l - \vec{r}_k|} \text{sum of potential energy between nuclei}$$

These operators are now input into the TISE (eq. ??).

$$\left[\left(-\sum_i \frac{\hbar^2}{2m} - \sum_k \frac{\hbar^2}{2M} \right) \nabla^2 + \sum_{i,k} \frac{z_i}{|\vec{r}_i - \vec{r}_l|} + \frac{1}{2} \left(\sum_{i,j, i \neq j} \frac{1}{|\vec{r}_i - \vec{r}_j|} + \sum_{k,l, k \neq l} \frac{z_k z_l}{|\vec{r}_l - \vec{r}_k|} \right) \right] |\Psi\rangle = E|\Psi\rangle \quad (5.103)$$

5.6.4 Born-Oppenheimer

The TISE arrived at is far too complicated to solve, even for the simple ensembles of atoms. It represents the many body system of electrons and nuclei, and it takes the positions of all nuclei and electrons as input variables (eq. ??).

$$\hat{H}|\Psi(\vec{r}_e, \vec{r}_n)\rangle = E|\Psi(\vec{r}_e, \vec{r}_n)\rangle$$

where $\vec{r}_e = r_{e,1}, r_{e,2}, \dots, r_{e,i}$ (electron positions) (5.104)

where $\vec{r}_n = r_{n,1}, r_{n,2}, \dots, r_{n,i}$ (electron positions)

In 1927 the Born-Oppenheimer approximation was proposed to separate the electron components from the nuclei in the Hamiltonian.

Protons and Neutrons are almost 2,000 times the mass of electrons. With respect to the electrons, they move much slower and may be considered to be fixed or frozen in place. Simplifying for a moment to a single electron and proton, due to Newton's second law, we can see that the acceleration of the electron would be similarly 2,000 times that of the proton: $f_e = f_p$ and $m_e a_e = m_p a_p$ which leads to $a_e = \frac{m_p}{m_e} a_p$. As the nuclei move, the electrons are assumed to respond instantly, remaining in the ground state and not being promoted into higher energy levels.

The Hamiltonian for the electrons may be written with the electron co-ordinates as a variable, and the nuclei co-ordinates as a parameter (eq. ??).

$$\hat{H}_e(\vec{r}_e; \vec{r}_n) = \hat{T}_e(\vec{r}_e) + \hat{V}_{e-e}(\vec{r}_e) + \hat{V}_e - n(\vec{r}_e; \vec{r}_n) \quad (5.105)$$

The wavefunction and energy for the electrons may be calculated, although if the nuclear coordinates are changed, i.e. by changing the parameter r_n , the wavefunction and energy will need to be recalculated.

$$\hat{H}_e(\vec{r}_e; \vec{r}_n) \psi_e(\vec{r}_e; \vec{r}_n) = E_e(\vec{r}_n) \psi_e(\vec{r}_e; \vec{r}_n) \quad (5.106)$$

$$\Psi(\vec{r}_e, \vec{r}_n) = \chi_{ne}(\vec{r}_e) \psi_e(\vec{r}_e; \vec{r}_n) \quad (5.107)$$

The electronic Hamiltonian (eq. ??) is still dependent on the electronic co-ordinates. As there are three co-ordinates per electron, there are 3 dimensions when solving for a hydrogen atom. For an Iron atom, with 26 electrons, there are 78 dimensions, and for a 4x4x4 FCC supercell of Iron there would be 256 atoms, 26 electrons per atom and 3 dimensions per electron, giving a total of 19,968 dimensions. Even for small numbers of electrons, solving this equation is impractical.

5.6.5 Crystals, Reciprocal Space and Bloch Theorem

A Bravais lattice is a construct used to describe a periodic crystal lattice. It has the following properties given in eq. ??.

$$\vec{R} = n_1 \vec{a}_1 + n_2 \vec{a}_2 + n_3 \vec{a}_3$$

$$n_1, n_2, n_3 \in Z$$

$$\vec{a}_1, \vec{a}_2, \vec{a}_3 \text{ are independent}$$
(5.108)

There are 14 Bravais lattices and 7 families of these lattices, and these lattices may be grouped by vector length and angle relationships (table. ??). This work is primarily concerned with cubic and tetragonal crystals, although distortions are applied to these crystals throughout.

Class	Lengths	Angles
Cubic	$a = b = c$	$\alpha = \beta = \gamma = 90$
Hexagonal	$a = b, c$	$\alpha = \beta, \gamma = 120$
Rhombohedral	$a = b = c$	$\alpha = \beta = \gamma \neq 90$
Tetragonal	$a = b, c$	$\alpha = \beta = \gamma = 90$
Orthorhombic	a, b, c	$\alpha = \beta = \gamma = 90$
Monoclinic	a, b, c	$\alpha = \beta = 90, \gamma \neq 90$
Triclinic	a, b, c	$\alpha, \beta, \gamma,$

Table 5.4: Bravais lattice vector length and angle relationships

Bloch Theorem

Metals are made up from grains which in turn are crystal lattices of atoms. Despite the majority of metals being composed of a large collection of microscopic crystals, rather than being a single perfect crystal, most of their properties may be calculated as if the metal were a single crystal.

The grain size of water quenched SS304 is approximately 30 micrometers across[grainsizestee]. If the crystal were a cube, it would contain 2.0×10^{15} atoms and it would have sides over 100,000 atoms in length.

In solid state physics, in order to solve the TISE for such a crystal, it is useful to consider an infinite sized crystal. It may be helpful to visualise this as a "ring" of atoms in one dimension (fig. ??) or as a super-cell with periodic boundary conditions in three dimensions.

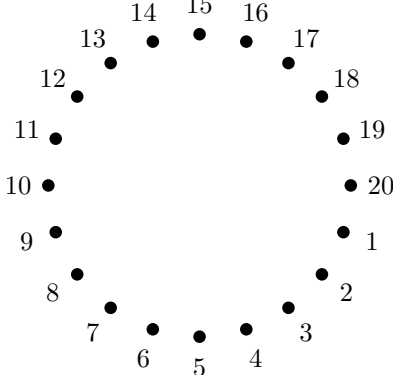


Figure 5.11: A useful, albeit incorrect, way of visualising an "infinite" chain of atoms in 1D

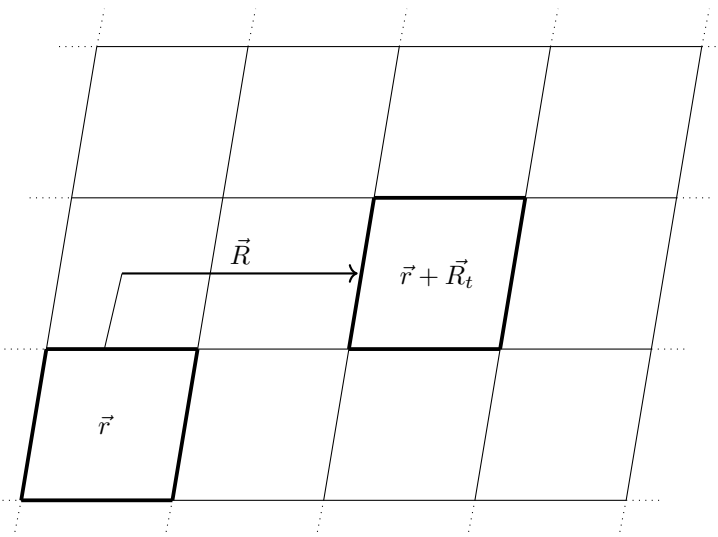


Figure 5.12: A 2D example of a translation by an integer multiple of the unit cell from the origin unit cell

As the structure is a repeating lattice, any point within a unit cell is equivalent to any other point translated by an integer multiple of the lattice vector (fig. ??).

$$\psi(\vec{r}) = \psi(\vec{r} + \vec{R}_t) \quad (5.109)$$

where $\vec{R}_t = n_1 \vec{R}_1 + n_2 \vec{R}_2 + n_3 \vec{R}_3$

where \vec{R} is the real lattice vector

Reciprocal space, also known as k-space or momentum space, is a mathematical construct. It is an imaginary space where the lengths, and volumes, are the inverse of real space and planes of atoms are represented as points.

Starting with a lattice of points in real space \vec{R} , points in reciprocal space \vec{G} only are valid points if $\exp(i\vec{G} \cdot \vec{R}) = 1$ [solidstatebasics]. A real space vector \vec{R} is transformed to it's reciprocal in the following way, where Ω is the volume of the primitive cell in real space.

$$\begin{aligned} \vec{g}_1 &= \frac{2\pi}{\Omega} \vec{r}_2 \times \vec{r}_3 \\ \vec{g}_2 &= \frac{2\pi}{\Omega} \vec{r}_3 \times \vec{r}_1 \\ \vec{g}_3 &= \frac{2\pi}{\Omega} \vec{r}_1 \times \vec{r}_2 \\ \Omega &= \vec{r}_1 \cdot (\vec{r}_2 \times \vec{r}_3) \end{aligned} \quad (5.110)$$

If the crystal structure is modelled as an infinitely repeating lattice, the potential also has the same periodicity (eq. ??).

$$V(\vec{r}) = V(\vec{r} + \vec{R}_t) \quad (5.111)$$

As the potential is a periodic function, it may be written as a fourier series in reciprocal space (eq. ??).

$$V(\vec{r}) = \sum_{\vec{G}} V_{\vec{G}} \exp(i\vec{G} \cdot \vec{r}) \quad (5.112)$$

The wave function for an electron in the lattice is also periodic and may be written as the product of a plane wave.

$$\psi_{n\vec{k}}(\vec{r}) = u_{n\vec{k}}(\vec{r}) \exp(i\vec{k} \cdot \vec{r}) \quad (5.113)$$

$$\begin{aligned} u_{n\vec{k}}(\vec{r}) &= u_{n\vec{k}}(\vec{r} + \vec{R}_t) \\ \psi_{n\vec{k}}(\vec{r}) &= \psi_{n\vec{k}}(\vec{r}) \exp(i\vec{k} \cdot \vec{R}_t) \end{aligned} \quad (5.114)$$

The Born-von Karman boundary conditions apply to the wave function such that:

$$\psi_{n\vec{k}}(\vec{r} + \vec{R}_t) = \psi_{n\vec{k}}(\vec{r}) \text{ where } \vec{R}_t = \sum_i N_i \vec{a}_i \text{ and } N_i \in \mathbb{Z} \quad (5.115)$$

With these boundary conditions and use of plane waves, Bloch theorem replaces an enormous number of electrons with an infinite number electrons in a periodic lattice where only those in the unit cell need to be considered.

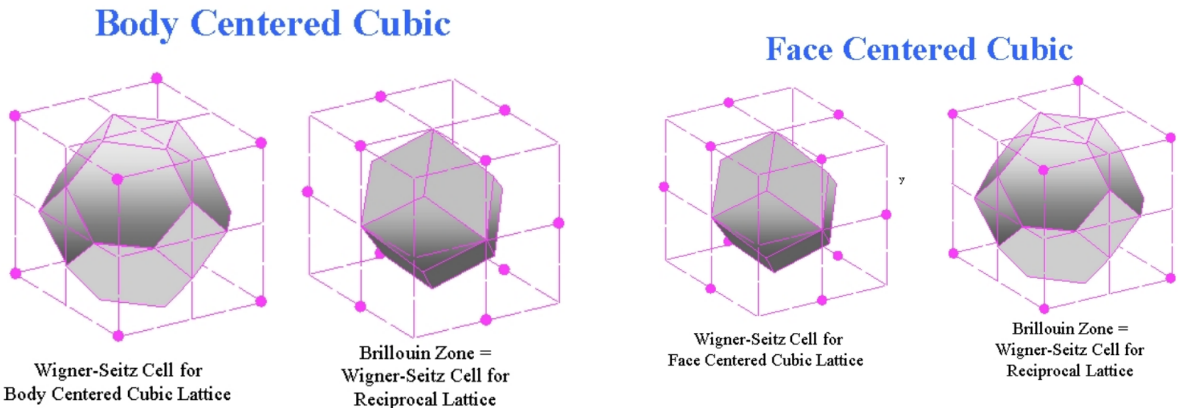


Figure 5.13: BCC Wigner Seitz Cell and BZ [fccbccreciprocal]

Figure 5.14: FCC Wigner Seitz Cell and BZ [fccbccreciprocal]

The (first) Brillouin Zone is a volume in (3D) reciprocal space and it is analogous to the Wigner-Seitz cell in real space. It is the primitive lattice cell in reciprocal space. The reciprocal of a BCC lattice is a FCC lattice (fig. ??) and vice versa (fig. ??). In real space a point anywhere in the lattice is a integer multiple of the lattice vector away from the same point in the origin Wigner-Seitz cell. There are an infinite number of wave vectors \vec{k} in reciprocal space, but by virtue of the periodicity of the lattice, they are also all found within the Brillouin Zone. If the crystal has symmetries, the BZ may be reduced further to the irreducible Brillouin zone.

Within the BZ there are energy surfaces. Picking a straight line through reciprocal space allows one to plot the energy bands along that one dimensional space. A particularly important energy surface is the Fermi surface and, in the one electron model, this marks the boundary between the occupied and unoccupied states at 0K [hjonesfermi]. The Fermi energy is the energy of the highest occupied state at 0K.

5.6.6 Hohenberg-Kohn Theorem

In the 1960s, Hohenberg and Kohn[hohenbergkohn] simplified the problem of solving the many electron TISE in an exact way by proving:

- in an external potential $v(\vec{r})$, the potential is uniquely determined by the density of the ground state $n_0(\vec{r})$ assuming that the particles are non-degenerate
- a uniquely defined functional $E[\rho(\vec{r})]$ exists and the ground state energy, $\min(E[\rho(\vec{r})])$, is found by varying the density

The proof starts by picturing a box of electrons that interact with each other through coulomb repulsion within an external potential $v(r)$, for example the potential of “fixed” nuclei following the Born Oppenheimer approximation.

$$\begin{aligned}\hat{H} &= \hat{T} + \hat{V} = \frac{1}{2} \nabla^2 + V(\vec{r}) \\ \left[-\frac{1}{2} \nabla^2 \right] \Psi(\vec{r})_0 &= E_0 \Psi(\vec{r})\end{aligned}\tag{5.116}$$

$$\hat{H} = \hat{T} + \hat{V} + \hat{U}\tag{5.117}$$

where

$$T = \frac{1}{2} \int \nabla \psi^*(\vec{r}) \nabla \psi(\vec{r}) d\vec{r}\tag{5.118}$$

$$V = \int v(\vec{r}) \psi^*(\vec{r}) \psi(\vec{r}) d\vec{r}\tag{5.119}$$

$$U = \frac{1}{|\vec{r} - \vec{r}'|} \psi^*(\vec{r}) \psi^*(\vec{r}') \psi(\vec{r}) \psi(\vec{r}') d\vec{r} d\vec{r}'\tag{5.120}$$

In the eqs. ?? ?? ?? ?? the hamiltonian operator \hat{H} is a sum of the kinetic energy \hat{T} , the mutual coulomb repulsion \hat{U} and the operator due to an external potential (due to the nuclei) \hat{V} . The non degenerate ground state electron density is $n(\vec{r}) = \langle \Phi | \phi^*(\vec{r}) \phi(\vec{r}) | \Phi \rangle$.

The HK theorem shows that the external potential $v(\vec{r})$ is a unique functional of the electron density $n(\vec{r})$. The proof is that by contradiction where by two different states are assumed to have the same ground state charge density.

State A

$$\begin{aligned}\Psi_A &\text{ with potential } V_A(\vec{r}) \\ \text{Hamiltonian } \hat{H} &= \hat{T} + \hat{V}_A + \hat{U} \\ \text{TISE } \hat{H}_A \Psi_A &= E_A \Psi_A\end{aligned}$$

Assumption - this state has the charge density $n(\vec{r})$

State B

$$\begin{aligned}\Psi_B &\text{ with potential } V_B(\vec{r}) \\ \text{Hamiltonian } \hat{H} &= \hat{T} + \hat{V}_B + \hat{U} \\ \text{TISE } \hat{H}_B \Psi_B &= E_B \Psi_B\end{aligned}$$

The minimal property of the ground state gives the following [hohenbergkohn][hohenbergkohnleeuwen]:

$$\begin{aligned} E_A &= \langle \Phi_A | \hat{H}_A | \Phi_A \rangle \\ E_A &= \langle \Phi_A | \hat{H}_B + \hat{V}_A - \hat{V}_B | \Phi_A \rangle \\ E_A &= \langle \Phi_A | \hat{H}_B | \Phi_A \rangle + \int d^3 \vec{r} n(\vec{r}) (v_A(\vec{r}) - v_B(\vec{r})) \end{aligned} \quad (5.121)$$

$$E_A > E_B + \int d^3 \vec{r} n(\vec{r}) (v_A(\vec{r}) - v_B(\vec{r})) \quad (5.122)$$

The indices A and B are interchanged to give a second equation:

$$\begin{aligned} E_B &> E_A + \int d^3 \vec{r} n(\vec{r}) (v_B(\vec{r}) - v_A(\vec{r})) \\ E_B &> E_A - \int d^3 \vec{r} n(\vec{r}) (v_A(\vec{r}) + v_B(\vec{r})) \end{aligned} \quad (5.123)$$

By adding eq. ?? and eq. ?? together the integrals will cancel out.

$$E_A + E_B > E_A + E_B \quad (5.124)$$

This (eq. ??) is a contradiction and proves the first part of the HK theorem: $v(\vec{r})$ is uniquely determined by $n(\vec{r})$. If the charge density (fig. ?? and ??) is known, a single external potential exists for it.

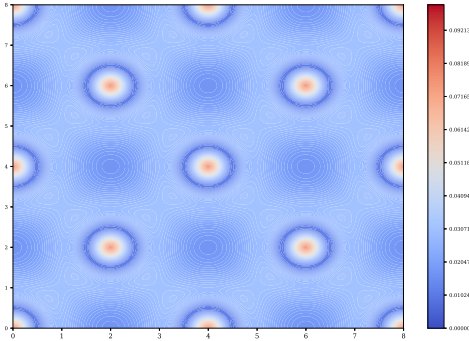


Figure 5.15: Charge density FCC aluminium xy plane at $z = 0.0a_0$

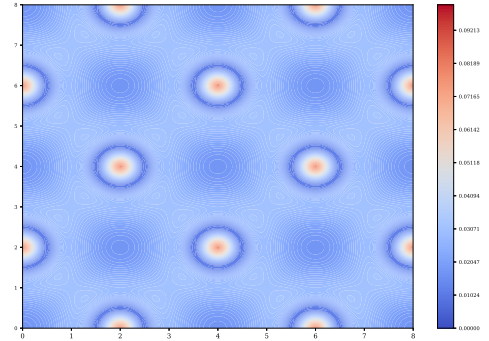


Figure 5.16: Charge density FCC aluminium xy plane at $z = 0.5a_0$

The next part of the theorem is to show that the energy functional $E[n(\vec{r})]$ exists and the minimum can be found by varying the charge density function. The kinetic and interaction functional \hat{T} and \hat{U} define a functional $F[n(\vec{r})]$.

$$F[n(\vec{r})] \equiv \langle \Phi | \hat{T} + \hat{U} | \Phi \rangle \quad (5.125)$$

This is a universal functional [**hohenbergkohn**] and it makes up a part of the energy functional. The energy functional is comprised of the HK functional $F[n(\vec{r})]$ and the external potential as shown in eq. ??.

$$E[n(\vec{r})] \equiv \int v(\vec{r})n(\vec{r})d\vec{r} + F[n] \quad (5.126)$$

For the ground state electron density $n(\vec{r})$ the energy will be equal to the ground state energy $E_0 = E_v[n]$. Where N is the number of particles in the system, the integral of the density over all space will sum to N (eq. ??).

$$N[n] = \int n(\vec{r})d\vec{r} \quad (5.127)$$

If the system has N particles the energy level for a none ground state energy, k, is given in eq. ??.

$$\epsilon_{v,k}[\Psi_k] \equiv \langle \Phi_k | \hat{V} | \Phi_k \rangle - \langle \Phi_k | \hat{T} - \hat{U} | \Phi_k \rangle \quad (5.128)$$

This has a minimum where $\Psi_k = \Psi_0$, the ground state.

$$\begin{aligned} \epsilon_{v,k}[\Psi_k] &= \int v(\vec{r})n_k(\vec{r})d\vec{r} + F[n_k] \\ \epsilon_{v,0}[\Psi_k] &= \int v(\vec{r})n_0(\vec{r})d\vec{r} + F[n_0] \\ \epsilon_{v,k} &> \epsilon_{v,0} \end{aligned} \quad (5.129)$$

5.6.7 Kohn-Sham Equations

The year following the Hohenberg-Kohn theorem, a set of self-consistent equations were derived by Kohn and Sham. The ground state energy of interacting jellium in the potential of fixed nuclei, an external potential, can be written as follows [**kohnsham**]:

$$E = T_s + U + V_{n-e} + E_{xc} \quad (5.130)$$

$$E = T_s[\rho(\vec{r})] + \int d\vec{r} v(\vec{r})\rho(\vec{r}) + \frac{1}{2} \int \int d\vec{r} d\vec{r}' \frac{\rho(\vec{r})\rho(\vec{r}')}{|\vec{r} - \vec{r}'|} + E_{xc}[\rho(\vec{r})] \quad (5.131)$$

The kinetic energy, T_s , is that of a system of non interacting and E_{xc} is the exchange and correlation of an interacting system. The exchange and correlation energy functional exists, but is unknown.

The Kohn-Sham equations are used to calculate the energy of a system. The Schrödinger equation is not for all the atoms in the system; it's a one electron equation

$$\hat{H}_{KS}\psi_i = E_i\psi_i \quad (5.132)$$

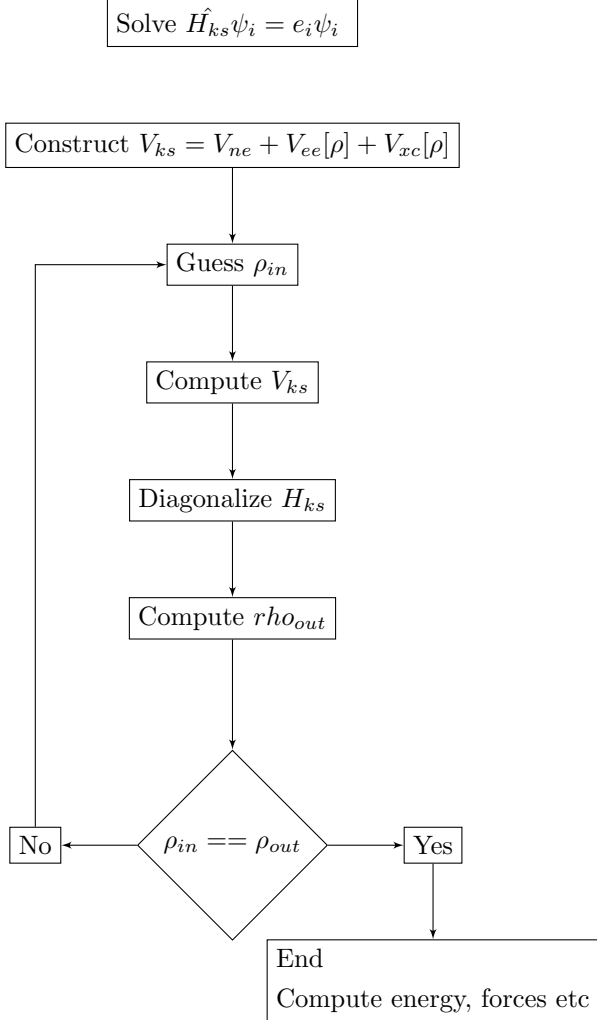
$$\left(-\frac{1}{2}\nabla^2 + \hat{v}_{KS}\right)\psi_i = E_i\psi_i \quad (5.133)$$

$$\hat{v}_{KS}(\vec{r}_e, \vec{r}_n) = v_{n-e}(\vec{r}_e, \vec{r}_n) + \int d^3\vec{r}' \frac{\rho(\vec{r}'_e)}{|\vec{r}_e - \vec{r}'|} + v_{xc}[\rho](\vec{r}_e) \quad (5.134)$$

It is important to note that even though this is a one electron equation it is an exact solution.

5.6.8 Self-Consistent Solution

The Kohn-Sham equations cannot be solved in the usual way. They require a value for the density, but the density is obtained by solving the equations, so there is a dilemma. It can however be solved self consistently: an initial density is guessed, and this is repeatedly updated until the density in and out values are the same (or within a set convergence threshold). The basic algorithm used by PWscf from the Quantum Espresso suite is shown below[abcdftsisssa].



5.6.9 Exchange-Correlation Energy

The Kohn-Sham equations have an exchange-correlation energy and this functional is used to collect together the electron energy not captured in the non-interacting energy functionals.

The Pauli exclusion principle states that two fermions, half integer spin particles, cannot occupy the same quantum state. This is why electrons occupy a unique orbital within an atom defined by the quantum numbers n, l, m_l and m_s . Consider two particles at points \vec{r}_a and \vec{r}_b ; the probability amplitude of the wavefunction of these particles equals 1.

$$|\Psi(\vec{r}_a, \vec{r}_b)|^2 = 1 \quad (5.135)$$

Exchanging the particles must also give the same result; they still must exists somewhere with probability 1.

$$|\Psi(\vec{r}_b, \vec{r}_a)|^2 = 1 \quad (5.136)$$

Bosons, integer spin particles, are symmetric when exchanged:

$$\Psi(\vec{r}_a, \vec{r}_b) = \Psi(\vec{r}_b, \vec{r}_a) \quad (5.137)$$

Fermions, on the other hand, are antisymmetric:

$$\Psi(\vec{r}_a, \vec{r}_b) = -\Psi(\vec{r}_b, \vec{r}_a) \quad (5.138)$$

By setting up a wavefunction for two Fermions, and exchanging them, it can be seen why they cannot exist in the same state.

$$\Psi_{ab} = \psi_1(\vec{r}_a, \vec{r}_b) - \psi_2(\vec{r}_b, \vec{r}_a) \quad (5.139)$$

$$\Psi_{ab} = \psi_1(\vec{r}_a, \vec{r}_b) - \psi_2(\vec{r}_a, \vec{r}_b) = 0 \quad (5.140)$$

The XC term combines the difference between the real system and the fictitious non-interacting system set out in the Kohn-Sham equations. It also includes the difference between the quantum mechanical electron-electron repulsion and classical electron-electron repulsion. Unfortunately, whilst we know a functional exists, we do not know the exact form of it [**ldaggaperdew**].

5.6.10 Pseudopotentials

Plane wave basis sets are used to help solve the TISE. The DFT code used in this work is Quantum Espresso, and the binary that carries out the calculations is named PWscf: plane wave self consistent field.

Where \vec{G} is the reciprocal lattice vector, a summation of plane waves may be used to construct each electronic wave function (eq. ??)[**paynedftreview**].

$$\Psi_{\vec{k},n} = \sum_{\vec{G}}^{|\vec{G}| < G_{max}} c_{\vec{k}+\vec{G},n} \exp(i(\vec{k} + \vec{G}) \cdot \vec{r}) \quad (5.141)$$

Unfortunately, the plane-wave basis sets required are too large to be used in practice, as they would need to represent the tight, rapidly oscillating inner orbitals as well as the valence electrons.

Bonding and material properties are primarily determined by valence electrons, not core electrons. Iron, for example, has two valence electrons in the 4s shell; however, it is a transition metal and the partially empty 3d shell is also important to consider. The core electrons do not contribute as much to the bond and the model may be simplified using pseudopotentials.

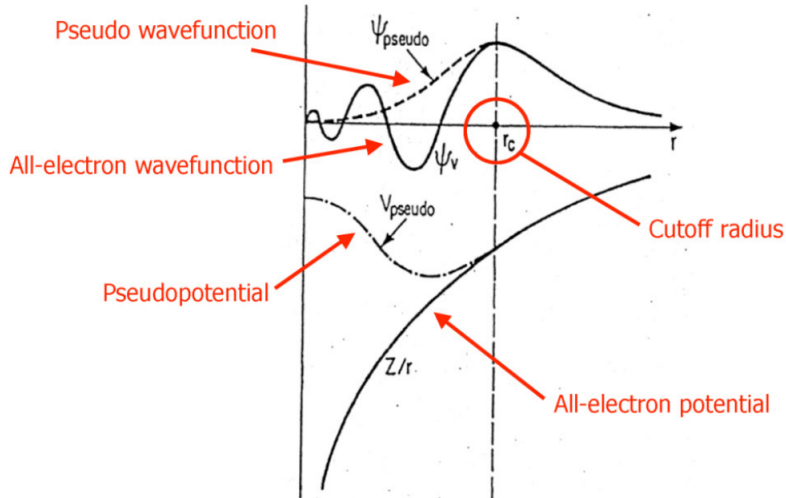


Figure 5.17: Replacing the complex potentials with a pseudopotential[ppselloni]

The eigen-energies of core electrons are also much larger than properties we see in materials, such as the cohesive energies and this also raises a concern that including the core electrons may introduce errors that are on a similar scale to the energies we are calculating.

The rapidly oscillating function in the core is replaced by a smoother pseudopotential. The same material properties are calculated as the valence electron functions are preferred, but a much smaller basis set is required to do so. There are a wide range of pseudopotentials available to use in DFT calculations, and one major distinguishing feature is how they treat the XC potential $v_{xc}([n]; \vec{r})$.

$$\left(\frac{1}{2} + V_{ext}(\vec{r}) + V_H(\vec{r}) + V_{xc}(\vec{r}) \right) \psi_{k,\sigma}(\vec{r}) = \epsilon_{k,\sigma} \psi_{k,\sigma}(\vec{r}) \quad (5.142)$$

The KS equation consists of several potentials including the exchange-correlation energy. This term represents the many-electron effects.

LDA

The local density approximation replaces the electron density with jellium, a homogeneous electron gas. Kohn and Sham, in their original 1965 work, introduced jellium as the density model and, despite its simplicity in comparison to the real electron density distribution, it has worked well for simple metals.

$$E_{xc}^{LDA}[\rho] = \int d^3\vec{r} \rho(\vec{r}) [e_x(\rho(\vec{r})) + e_c(\rho(\vec{r}))] \quad (5.143)$$

Several different LDA functionals have been developed over the years, including that of Perdew and Zunger. This functional takes the form given in eq. ??[dftgupta1].

$$\epsilon_C[n(\vec{r})] = \begin{cases} \frac{-0.14231}{1+1.9529r_s^{0.5})+0.334r_s} & r_s \geq 1 \\ -0.0480 + 0.0311lr(r_s) - 0.0116r_s + 0.0020r_sln(r_s) & r_s < 1 \end{cases} \quad (5.144)$$

LSDA

Electrons are fermions and have half integer spin. When trapped in a potential, such as an atom or a crystal lattice, electrons must take difference quantum states and one of the parameters is the spin of the electron. The LDA does not treat spin at all, but the LSDA splits the density into up and down spin (eq. ??[ldaggaperdew]).

$$\begin{aligned} \rho_{\uparrow}(\vec{r}) &= \sum_k^{\text{occ}} |\phi_{k,\uparrow}(\vec{r})|^2 \\ \rho_{\downarrow}(\vec{r}) &= \sum_k^{\text{occ}} |\phi_{k,\downarrow}(\vec{r})|^2 \\ \rho(\vec{r}) &= \rho_{\uparrow}(\vec{r}) + \rho_{\downarrow}(\vec{r}) \end{aligned} \quad (5.145)$$

The XC energy is now dependent on the spin up and spin down density as well as the position (eq. ??[ldaggaperdew]).

$$\begin{aligned} E_{xc}^{LSDA}[\rho_{\uparrow}, \rho_{\downarrow}] &= \int d^3\vec{r} \rho(\vec{r}) [e_x(\rho(\vec{r})) f(\zeta(\vec{r})) + e_c(\rho(\vec{r}), \zeta(\vec{r}))] \\ \zeta &= \frac{\rho_{\uparrow} - \rho_{\downarrow}}{\rho_{\uparrow} + \rho_{\downarrow}} \\ f(\zeta) &= \frac{1}{2} \left((1 + \zeta)^{4/3} + (1 - \zeta)^{4/3} \right) \end{aligned} \quad (5.146)$$

The energy of the system now being solved is also dependent upon the charge density and spin polarization (eq. ??).

$$E = T[\rho, \zeta] + E_{ext}[\rho] + \frac{1}{2} E_{ee}[\rho] + E_{xc}[\rho, \zeta] \quad (5.147)$$

GGA

In the LDA and LSDA approximations, the electron density is that of an homogeneous electron gas that does not represent the real electron density. The density of this gas may change in space, but locally it is a constant density with no gradient.

$$E_{xc}^{GGA}[\rho_{\uparrow}, \rho_{\downarrow}] = \int d^3r f(\rho_{\uparrow}, \rho_{\downarrow}, \nabla \rho_{\uparrow}, \nabla \rho_{\downarrow}) \quad (5.148)$$

The GGA functional (eq. ?? [ldaggaperdew]) takes the spin up spin down electron densities as well as their gradients.

The PBE functional was developed to address some of the short falls of the Perdew-Wang PW91 LSDA functional. These include an over complication in the formulation of PW91 and that it was designed to satisfy many exact conditions. The PBE development focused more on energetically significant conditions[perdewggamadesimple].

Successes of GGA

- atomization energy of molecules better
- binding energy curves more realistic
- Fe is bcc ferromagnet with GGA (fcc non-magnet with LSDA)
- Gives the anti invar effect in gamma-Fe and fc Fe-Mn
- Improvement on 4% accuracy for LSDA of alkali metal lattice constants
- Better lattice constants and bulk moduli of transition metals
- Isostructural transformation from open to close packed improved
- Successful calculation of a monovacancy in silicon
- Oxidation of the Si(001) surface using spin polarized GGA

Failures

- exchange-correlation holes can be unrealistic under some circumstances
- works better for exchange correlation together than either alone
- interaction of electrons in different shells poorly described

Figure 5.18: Successes and failures of the GGA functional[[Idaggaperdew](#)]

$$E_c^{PBE}[\rho_{\uparrow}, \rho_{\downarrow}] = \int d^3r \rho [e_c(r_s, \zeta) + H(r_s, \zeta, t)] \quad (5.149)$$

$$E_x^{PBE}[\rho] = \int d^3r \rho e_x(\rho) F_x(s) \quad (5.150)$$

The functional is split into a correlation energy (eq. ??) and exchange energy (eq. ??). ζ is the relative spin polarization $\zeta = (\rho_{\uparrow} - \rho_{\downarrow})/(\rho_{\uparrow} + \rho_{\downarrow})$ and r_s is the local Seitz radius where $\rho = 3/4\pi r_s^3$. The functions $e_x(\rho)$ and $e_c(\rho)$ are the exchange and correlation energy per electron of unpolarised uniform electron gas[[Idaggaperdew](#)]. A full description of the functional is in the appendix ??.

LSDA vs GGA Potentials

Typically, GGA is an improvement over LSDA, with improvements in the total energies and structural energy differences[[perdewggamadesimple](#)]. Another short coming of LSDA is that it predicts FCC to be the optimal structure for pure iron at 0K, which is incorrect[[perdewggabackwardforward](#)]. A list of success stories and failures were discussed shortly after the publication of the PBE functional and these are summarised in table ??[[Idaggaperdew](#)].

In the case of the compound Titanium Disilicide, $TiSi_2$, GGA is in better agreement, overall, with experiment than LDA, although several values are better predicted by the latter. As shown in table ??, the data shows that LDA is within 1.26% of the experimental lattice parameters, 6.16% of the experimental bulk modulus and 18.3% the value of the experimental elastic constants; several of these were particularly poor, with an almost 45% disagreement. On the other hand, GGA is within 0.66% of the experimental lattice parameters, 3.62% of the experimental bulk modulus and 14.97% the value of the experimental elastic constants[[DftTiSiRavindran](#)].

Parameter	Experimental	LDA	GGA
a/angs	8.27	8.08	8.21
b/angs	4.80	4.74	4.81
c/angs	8.55	8.53	8.64
B_0 (Reuss)/GPa	146.8	156.9	141.9
B_0 (Voigt)/GPa	150.9	159.1	145.0
C_{11} /GPa	317.5	377.2	326.0
C_{22} /GPa	320.4	341.1	298.4
C_{33} /GPa	413.2	425.3	371.9
C_{44} /GPa	112.5	136.5	123.5
C_{55} /GPa	75.8	93.7	85.3
C_{66} /GPa	117.5	154.6	135.9
C_{12} /GPa	29.3	27.8	22.4
C_{13} /GPa	38.4	21.3	26.5
C_{23} /GPa	86.0	95.1	105.5

Table 5.5: Experimental vs LSDA vs GGA for *TiSi₂*[**DftTiSiRavindran**]

Lanthanum aluminate ($LaAlO_3$) has also been studied using DFT, but this material is better modelled (to reproduce lattice parameters and bulk modulus) with either LDA or a specific form of GGA, the Perdew-Burke-Ernzerhof functional revised for solids (PBESOL) potential. The PBESOL is a revised PBE functional designed to better reproduce lattice parameters for solids, as shown in table ??.

Parameter	Experimental	LDA	GGA	GGA (PBESOL)
a/angs	3.78	3.74	3.82	3.77
B_0 /GPa	215	224.00	190.35	206.41

Table 5.6: Experimental vs LSDA vs GGA vs GGA PBESOL for *LaAlO₃*[**laalo3gga**]

A complete library of pseudo-potentials is available through the Quantum Espresso website. Several of these have been tested with the PWscf code to calculate the lattice parameter and bulk modulus of simple metals including Aluminium and Sodium.

As can be seen from table ??, the PBE and PBESOL GGA type potentials are in general better at reproducing the lattice parameters. However, for Aluminium, the PZ LSDA type potential is in better agreement when calculating the bulk modulus. Overall, the GGA type potentials with the total self-consistent potential pseudized (these are the pseudopotential files that contain -n- in the name, rather than -nl-) perform best for these simple metals.

Whilst DFT is an exact method for solving the TISE, there are a number of approximations that still need to be made in addition to there being gaps in our knowledge (i.e. a lack of an exact functional for the XC).

5.6.11 Ecut, K-Point Integration and Smearing

As discussed in section ?? the wavefunction can be expressed as a periodic function with the same period as the crystal lattice (eq. ??). The periodic function may then be written as a sum of plane waves (eq. ??).

$$\psi_{n\vec{k}}(\vec{r}) = u_{n\vec{k}}(\vec{r}) \exp(i\vec{k} \cdot \vec{r}) \quad (5.151)$$

Pseudo-potential	Element	a/angs	B_0/GPa
Experimental	Na	4.29[periodictable na]	6.3[periodictable na]
Na.pz-spn-kjpaw_psl.1.0.0	Na	4.06	8.72
Na.pbe-spn-kjpaw_psl.1.0.0	Na	4.20	7.67
Na.pbesol-spn-kjpaw_psl.1.0.0	Na	4.17	7.50
Experimental	Al	4.05[periodictable al]	76[periodictable al]
Al.pz-nl-kjpaw_psl.1.0.0	Al	3.98	78.6
Al.pz-n-kjpaw_psl.1.0.0	Al	3.98	78.6
Al.pbe-nl-kjpaw_psl.1.0.0	Al	4.04	91.3
Al.pbe-n-kjpaw_psl.1.0.0	Al	4.04	75.0
Al.pbesol-nl-kjpaw_psl.1.0.0	Al	4.01	87.7
Al.pbesol-n-kjpaw_psl.1.0.0	Al	4.01	79.0

Table 5.7: Experimental vs LSDA vs GGA - the DFT values were computed with a PWscf[**quantumespresso**] using a 2x2x2 cell, 7x7x7 kpoints and ecutwfc=50

$$u_{n\vec{k}}(\vec{r}) = \sum_{\vec{G}} V_{\vec{G}} \exp(i\vec{G} \cdot \vec{r}) \quad (5.152)$$

Solving the Kohn-Sham equations requires the matrix diagonalization of a size NxN where N is the number of planewaves for each k-point in the Brillouin Zone[**energycutoff**]. The number of planewaves can be reduced to satisfy eq. ???. In practice this will mean reducing E_{cut} whilst ensuring the desired accuracy is still met.

$$\frac{\hbar^2 G^2}{2m} \leq E_{cut} \quad (5.153)$$

In order to compute the energy using HK, the charge density in the BZ is calculated. It is impossible to diagonalise the matrix at an infinite number of k-points. The integral is replaced with a summation over selected points which in turn are weighted (eq. ??)[**bzsampling**].

$$\rho(\vec{r}) = \frac{1}{\Omega_{bz}} \sum_i \int f(\vec{k}, i) \psi_{i,\vec{k}}^*(\vec{r}) \psi_{i,\vec{k}}(\vec{r}) d\vec{k} \frac{1}{\Omega_{bz}} \int_{BZ} d\vec{k} \rightarrow \sum_{\vec{k}} \omega_{\vec{k}} \quad (5.154)$$

Due to Bloch theorem and the Born-Von-Karman boundary conditions, only the first BZ needs to be sampled. As discussed earlier, if there are further symmetries in the unit cell, only the IBZ need to be sampled.

The integral over k-space is replaced by a set of points in k-space that are sampled. The higher the number of points, the higher resolution the space is sampled in, but the longer the calculation will take. The Gamma point Γ is a high symmetry point in reciprocal space and is located at (0,0,0). It may be used as the only sampling point in some DFT calculations.

The Monkhorst-Pack grid is a special set of k-points. They are distributed evenly in reciprocal space and may be aligned such that either one point coincides with Γ or such that 8 points closest points surround Γ at an equal distance. By offsetting the grid from Γ and the coordinate axis of reciprocal space, the sampling better avoids points of high symmetry.

Where the system is spin degenerate, each state is occupied by 2 electrons for the lower $\frac{N_e}{2}$ states ($f(\vec{k}, i) = 2$), and zero otherwise ($f(\vec{k}, i) = 0$)[**marzarithesis1**]. This drop, from states occupied by two electrons to empty

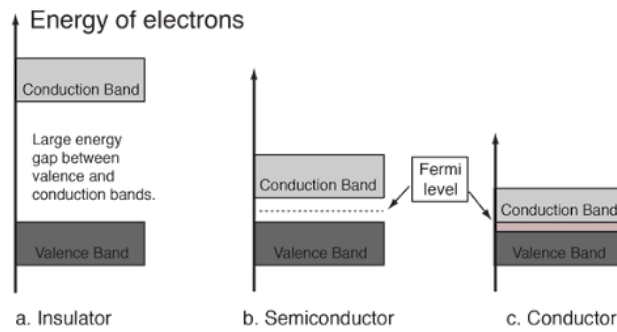


Figure 5.19: Energy gap between valence and conduction bands[[bandgapshyperphysics](#)]

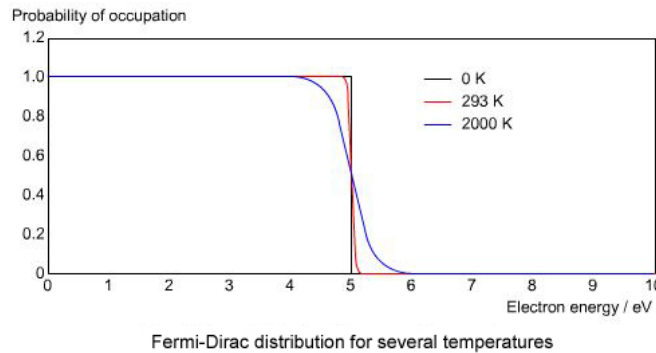


Figure 5.20: Probability $F(E)$ of finding a fermion with energy E at several temperatures[[fermidiracdist](#)]

states occurs at the Fermi surface and it results in a discontinuity in the functions being integrated over in eq. ???. This is the case for an electron gas at absolute zero, but if the gas is heated then there is sufficient energy for electrons to occupy states above the Fermi energy.

Fermi-Dirac statistics determine the probability of a Fermion having an energy E (eq. ??). As the temperature increases the probability of finding a fermion above the Fermi energy increases (fig. ??). This also smooths the discontinuity at the Fermi surface between the occupied and unoccupied states (at 0K).

$$F(E) = \frac{1}{\exp(\frac{E-E_F}{kT}) + 1} \quad (5.155)$$

To avoid having to integrate the BZ with a very fine mesh, a smearing function is introduced to remove the discontinuity at the Fermi surface, making the integral over the BZ differentiable at every point. The relationship between the delta and Heaviside step is used to replace the step function when integrated (eq. ??).

$$\int_{-\infty}^{\infty} \delta(k) dk = \Theta(x) \quad (5.156)$$

$$I = \int_{-\infty}^{\infty} S(\epsilon - E_F) \int_{BZ} f(\vec{k}) \delta(\epsilon - E(\vec{k})) d\vec{k} d\epsilon \quad (5.157)$$

The step function at the Fermi surface (eq. ??), that causes the discontinuity, may be replaced with a smearing function[[methfesslpaxton](#)]. Four of these functions are available to use in the PWscf DFT code.

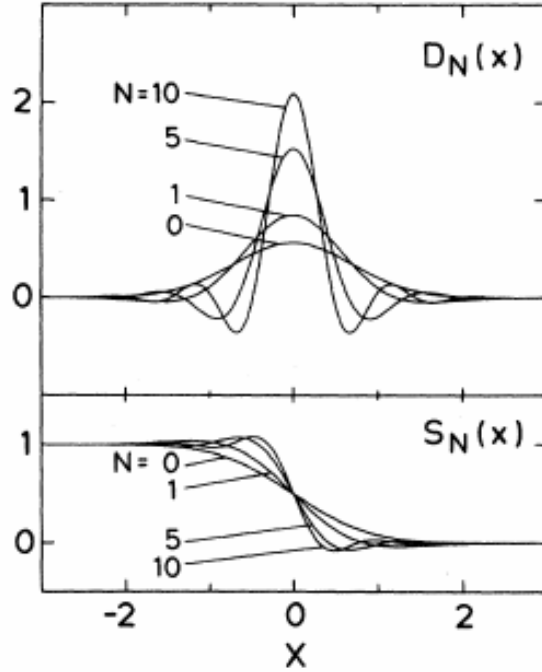


Figure 5.21: Delta function replaced by successive Hermite polynomials [**methfesslpaxton**]

The Fermi-Dirac function, as mentioned above, is used to heat the system. It removes the discontinuity but the SCF will converge to the wrong energy (eq. ??).

$$S_{FD}(\epsilon) = \frac{1}{\exp(\frac{\epsilon - E_F}{kT}) + 1} \quad (5.158)$$

A Gaussian smear is also used to replace the step function although, unlike the Fermi-Dirac function, it has no physical meaning (eq. ??).

$$S_G(\epsilon) = \frac{1}{2} \left[1 - \text{erf} \left(\frac{\epsilon - \mu}{\sigma} \right) \right] \quad (5.159)$$

The Methfessel-Paxton method attempts to correct the errors introduced by the previous smearing functions where the delta function is replaced with Hermite polynomials (fig. ?? and eq. ??). A drawback of this method is that it allows for negative occupancy of electron states [**marzarithesis1**].

$$x = \epsilon - E_F \quad S_{MP,N}(x) = \frac{1}{2} [1 - \text{erf}(x)] + \sum_{n=1}^N A_n H_{2n+1}(x) \exp(-x^2) \quad A_n = \frac{(-1)^n}{n! 4^n \sqrt{\pi}} \quad (5.160)$$

The Mazari-Vanderbilt function was developed to address the short falling of the Methfessel-Paxton function. The occupancy where this function is used is always positive (fig. ??).

$$x = \frac{\mu - \epsilon}{\sigma} \delta(x) = \frac{1}{\sqrt{\pi}} \exp(-(x - (\frac{1}{\sqrt{2}}))^2)(2 - \sqrt{2}x) \quad (5.161)$$

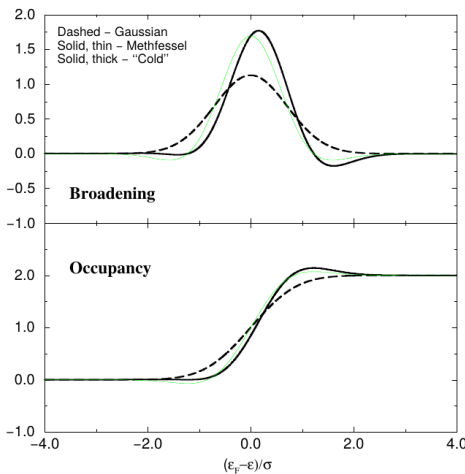


Figure 5.22: The occupancy for the Marzari-Vanderbilt smearing function is always positive, unlike the Methfessl-Paxton function[[marzarithesis2](#)]

5.7 Classical Molecular Dynamics

5.7.1 Introduction

Ab initio (DFT) calculations approximately solve the Schrödinger equation to calculate the energy, forces and stress of a given simulation. They take a relatively long time to calculate, have relatively small numbers of atoms (hundreds to thousands) and are fixed at one moment in time, although there are now programs that will run DFT MD. In comparison, Molecular Dynamics model a collection of atoms over a specified period of time. Much larger collections of atoms are possible (thousands to millions) and the interaction between atoms are predefined by interatomic potentials.

Molecular dynamics has been used to investigate the effects of radiation on materials. The damage event on the atomic scale is rapid in time, in the femtosecond to picosecond range, and affects a small volume of the material whereas the effects of the damage to the material on a mesoscopic and macroscopic scale may range from days to decades. In reactor pressure vessels, for instance, the damage and defect production will cover a large range of time and size scales[[damagebcciron](#)]:

- $10^{-10}m$ to $10^{-3}m$ (10^{18} to 10^{25} atoms)
- $10^{-17}s$ to 10^9s (tens of attoseconds to 30 years)

As a major element of steel, iron has often been the subject of MD simulations. Damage cascades have been studied in iron at a range of temperatures and PKA energies.

5.7.2 Molecular Dynamics Codes

Many MD codes are available for researchers to download freely and use from the Internet (although, terms may apply to the use). These include DL POLY (Fortran), Large-scale Atomic/Molecular Massively Parallel Simulator (C++) and MOLDY (C). Most are able to run using message passing interface to run the simulation in parallel across many compute nodes, with others being modified to take advantage of graphical processing units.

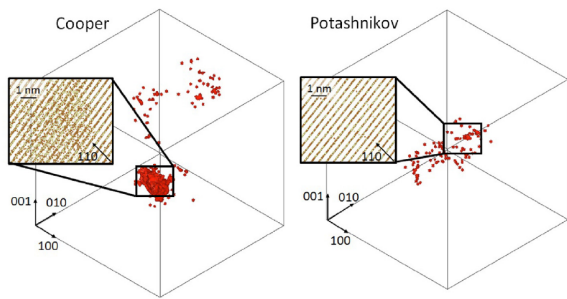


Figure 5.23: Damage in MOX
(LAMMPS)[**moxlammisdamage**]



Figure 5.24: Sputtering of plutonium oxide
(LAMMPS)[**pusputtering**]

Damage cascades in mixed oxides have been modelled recently using the LAMMPS code. A $70 \times 70 \times 70$ box with sides approximately 40nm in length and containing 4,116,000 atoms was used with PKAs having energies ranging from 5 to 75keV[**moxlammisdamage**]. The sputtering of material from the surface of plutonium oxide (IV) has also been modelled with LAMMPS using a box of 393,216 atoms with a PKA of 87.7keV. The timescale of the sputtering simulation was 7.8 picoseconds (7.8×10^{-12}) and the entire event was split into 1.0×10^5 time steps of 7.8×10^{-17} s.

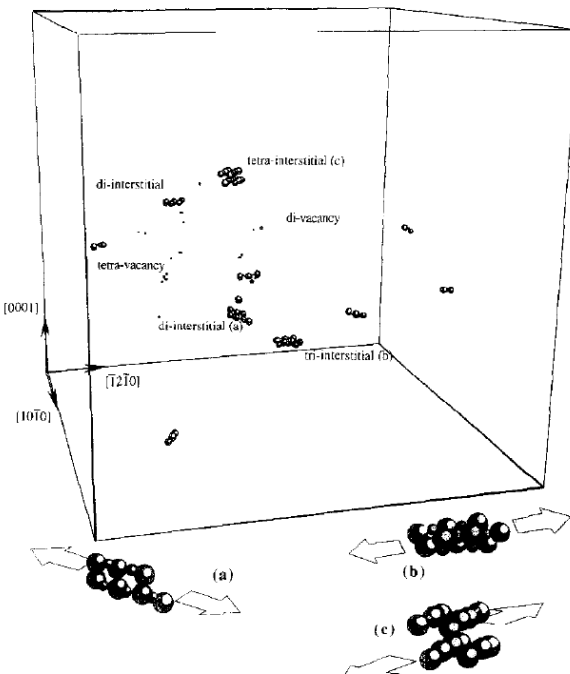


Figure 5.25: 5keV cascade (MOLDY)[**pkamoldy**]

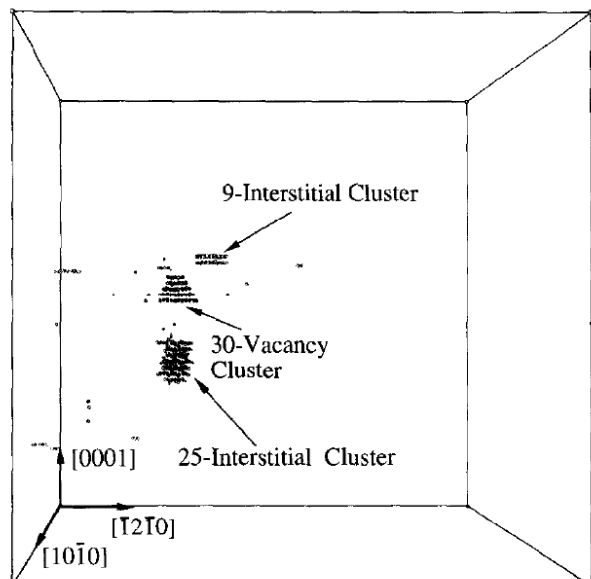


Figure 5.26: 20keV cascade (MOLDY)[**pkamoldy**]

MOLDY has previously been used to model primary knock on atoms in metals, at energies of 5kev, 10keV and 20keV which would be slightly lower than the typical iron PKAs close to U235 fuel in the reactor (fig. ??). This simulation however was in alpha-zirconium and the higher mass of zirconium, relative to iron, would lead to lower energy PKAs. The damage cascades were modelled in a 104,832 atom block for the 5keV PKA (figure ??) and a 445,536 atom block for the 20keV PKA (figure ??).



Figure 5.27: 100keV cascade after 50ps in TiO₂
(DL_POLY)[[dlpolyradiationdamage](#)]

DL_POLY has also been used to model damage cascades in various oxides (titanium, aluminium, silicon)[[dlpolyradiationdamage](#)]. The PKA energies are higher than those performed in MOLDY 15 years earlier, but still under 1MeV. The authors expect 1MeV simulation boxes to require at least 1 billion atoms, but the 100-200keV PKAs they modelled were within 10 million atom simulation boxes. Slightly larger boxes and damage cascades required longer simulation times, and with a box size of 43nm per side, a 50ps simulation time was used (fig. ??).

5.7.3 Neighbour List

The simple neighbour list creation has already been discussed earlier in this chapter (section ??), but many modern MD codes are designed to run on computers with many thousands of processor cores.

In the case of DL_POLY a link-cell domain decomposition is used. The supercell is divided up into subcells, and these must be at least the size of the cut-off radius. Each processor will work on a geometric domain and these will only interact with their immediate neighbours. The halo data for each subcell is only passed between processors before and after the calculation of the equations of motion of the atoms within each subcell.

5.7.4 Velocity Verlet Algorithm

Verlet integration is used by MD codes such as DL_POLY, LAMMPS, Democritus as well as MD DFT codes, as in the case of CASTEP.

First, the forces at time step n are calculated \vec{f}_n . Now, using these forces and the velocity at time step n, the half step velocity is computed (eq. ??).

$$\vec{v}_{n+\frac{1}{2}} = \vec{v}_n + \frac{\vec{f}_n \delta t}{2m} \quad (5.162)$$

The position of the next step, n + 1, is calculated using the position at n, the time step dt and the half step velocity (eq. ??).

$$\vec{r}_{n+1} = \vec{r}_n + \vec{v}_{n+\frac{1}{2}} \times \delta t \quad (5.163)$$

The forces are recalculated at the new position \vec{r}_{n+1} to give \vec{f}_{n+1} and this, along with the half step velocity, is used to compute the velocity at step n+1, \vec{v}_{n+1} (eq. ??).

$$\vec{v}_{n+1} = \vec{v}_{n+\text{half}} + \frac{\vec{f}_{n+1}\delta t}{2m} \quad (5.164)$$

This process is repeated for each time step δt from the start of the simulation to the end.

5.7.5 Selecting a Time Scale

Take, for example, a 50x50x50 BCC Iron supercell with a lattice parameter of 2.87 angstrom. The supercell measures almost 15nm on each side. Simulating a thermal neutron, travelling at 2,200 m/s, would require an overall time period of at least 7 picosecond to capture the neutron passing through the supercell. Higher energy particles would require smaller overall time periods, divided up into as many time steps as the user requires.

If PKA damage is being modelled, there may be a point where the depth of the damage cascade becomes larger than the supercell itself. Damage cascades of 500KeV iron atoms into an iron target travel to a depth of up to 300nm, which would require a simulation supercell at least 1,000 BCC cells deep. Kinetic Monte Carlo would be better suited at simulating higher energy damage cascades.

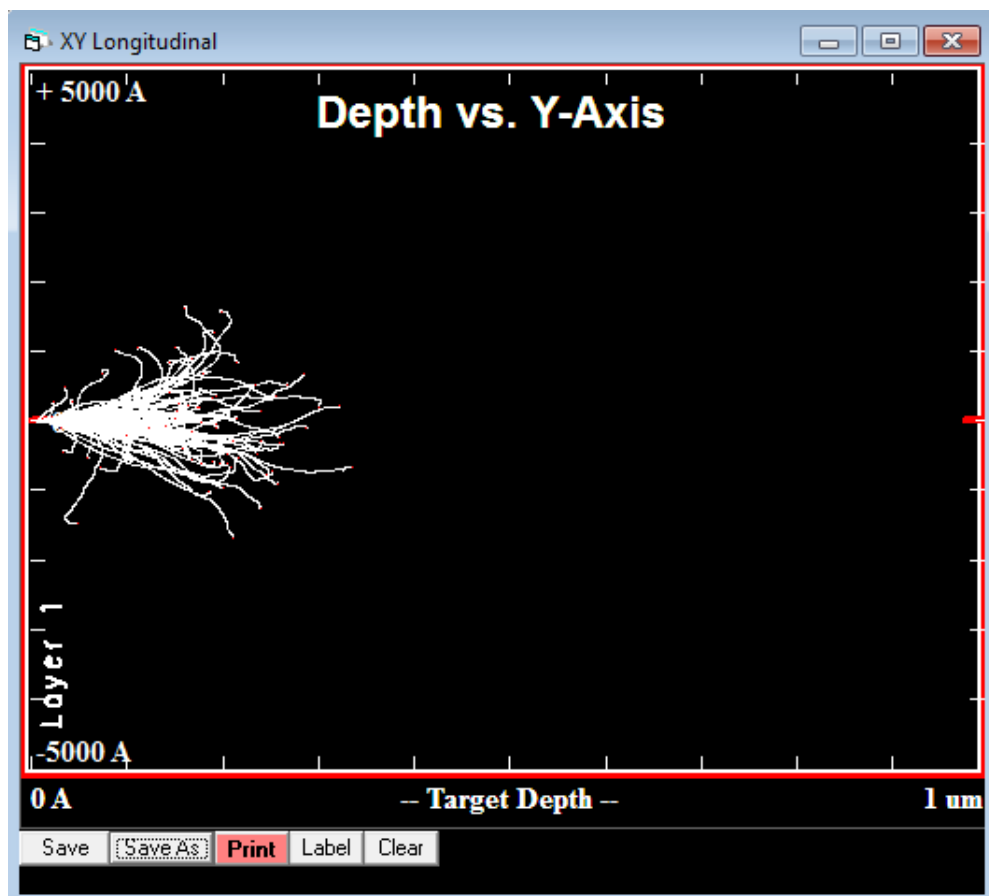


Figure 5.28: Damage cascade: 500kev iron projectiles into an iron target calculated with SRIM

To capture the required details the time steps would also need to be very fine, on the order of attoseconds or tens of attoseconds. This has been shown in the literature with time steps of 7.8×10^{-17} s [moxlammpsdamage].

5.8 Optimization

5.8.1 Introduction

Optimization is the process of finding the best solution for a problem that may also need to satisfy a number of imposed constraints. In terms of this work, there are several tasks where optimization plays a key role. The DFT code used, PWscf, employs the Broyden Fletcher Goldfarb Shanno algorithm to relax structures to give the optimum volume and optimal structure of an arrangement of atoms. During the fitting of the variety options of equation of state to the energy-volume points, the Levenberg-Marquardt Algorithm is used. Finally, a genetic algorithm and simulated annealing algorithm are coupled with LMA to locate the global optimal parameters for interatomic potential functions.

5.8.2 Continuous and Discrete Optimization

Problems that may be solved using discrete optimisation have, as the name suggests, discrete solutions. An example would be the travelling salesman problem, where the aim is to minimise the distance travelled by the salesman between cities. An example of the solution may be city E to A to B to C to D. There's a set of possible solutions to the problem. If the problem was changed such that any point within a 1 mile radius of the centre of each city is a valid solution, and the aim is to find the optimal points to travel between within the area of each city, it would become a continuous problem.

Fitting interatomic potentials to data is an example of continuous optimisation. The Morse potential takes three parameters plus the separation r between the two atoms. If the parameters are being optimised such that Morse potential matches the experimental forces (assuming they could be measured experimentally) between two atoms for a set of separation values, the choice of parameters isn't discrete; they are taken from a continuous range of real numbers.

5.8.3 Constrained and Unconstrained Optimization

There are constraints that may need to be considered, and constraints that apply to the fitting of interatomic potentials are as follows:

- continuous well behaved function
- continuous first-derivative, smooth change in force wrt r
- positive electron density
- smooth cutoff at some $r = r_{cut}$
- repulsion (ZBL/exponential) as r approaches 0
- continuous second-derivative
- enough parameters coupled with a good choice of functions so the potential is flexible enough to replicate all the experimental data well
- a small enough range of parameters to keep the parameter space small enough to search in a reasonable amount of time
- maintain physical elegance
- ignore physical elegance

Certain constraints listed will battle one-another, while others may be dropped, such as restricting to positive electron-densities if the choice to ignore physical elegance is selected.

5.8.4 Global and Local Optimization

An example to discuss the difference between local and global optimization will be given in a very literal sense. I am located near Birmingham, and I wish to find the highest point local to me. Using a modern smartphone and map I could quickly find the nearest hill to my current position; this would be the local maxima. I would, however, need to go up and down many peaks and troughs, scouring the entire surface of the Earth, until I found the global maxima, somewhere amongst the many peaks and troughs in the Himalayas.

When optimising the parameters of a function, it is relatively easy to find a local extreme that would give me the optimum parameters locally. It is a much harder task to find the global optimum, especially if very little, or nothing at all, is known about the function for which the parameters are being optimised.

5.8.5 Global Optimization Algorithms

Simulated Annealing

A large amount of computing power is required today to solve many problems in Physics. The optimum arrangement of Iron atoms, at various concentrations and temperatures is one such example, but nature knows the correct structure it should take because it has access to the rule book. It makes perfect sense to look to nature when designing optimisation algorithms.

Simulated annealing mimics the way a solid cools, with its atoms settling into the optimum relaxed positions as time passes. Initially, the solid is hot and the atoms are able to take non-optimal positions, but as the solid cools the atoms take their optimal places. The heating allows the atoms to move from non-optimal positions in the initial configuration.

Listing 5.3: Pseudocode for the simulated annealing algorithm

```
1 # Calculate the starting rss
2 rss = get_rss(p)
3
4 # Loop (n times, until a threshold is met, time runs out etc)
5 while(loop)
6 {
7     p_new = vary(p)          # Make a new set of parameters
8     rss_new = get_rss(p_new) # Get rss for these parameters
9
10    # Always accept BETTER
11    # Sometimes accept WORSE (depends on temperature and how bad it is)
12    if(rss_new < rss or rand(0.0,1.0) < exp((rss-rss_new) / temp))
13    {
14        p = p_new
15        rss = rss_new
16    }
17 }
```

The simulated annealing algorithm takes in a starting set of parameters. These are varied and, if the new parameters give a better solution to the problem, the parameters are updated. However, there is a chance that a worse set of parameters are used, and this depends on how bad they are and the current value of the temperature in the algorithm (listing ??). By allowing a worse set of parameters to be used, it gives the solution the chance to jump out of a local minimum and explore other solutions that it would otherwise be oblivious to.

The algorithm used in this work is available in the appendix (section ??).

Genetic Algorithm

It is unclear whether life started on this planet, or was brought to this planet, and this idea only removes the problem of how life as we are able to understand it was conceived to a different time and place. However it started, there is evidence of life on this planet approximately 3.5 billion years ago. Prokaryotes were the simple single cell organisms that inhabited our planet for billions of these. Their cell does not have a nucleus and the genetic information is contained in RNA and DNA within the cell.

Approximately 1.5 billion years ago, life made a leap forward in complexity and evolved into the first Eukaryotic cells. These are larger and more complex than Prokaryotes, and the genetic material is stored within a nucleus. Through processes of inheritance, variation, natural selection and the vast expanse of time, more complex organisms developed.

A set of solutions are bred with one another, and where there is an improvement the new variation is reinserted into the gene pool. There is a danger that the population can become a set of clones, so a large pool of sets of parameters is required, fresh parameters proposed every so often as well as a mechanism to prevent clones appearing.

As simulated annealing takes inspiration from cooling solids, genetic algorithms take inspiration from evolution. The algorithm used in this work is available in the appendix (section ??).

5.8.6 Local Optimization Algorithms

Gradient Descent

The gradient descent method is a reliable way of searching for a local minimum. It requires only the first derivative coupled with a line search to move closer to the minimum point. Close to the minimum, it is slower than the Newton-Gauss and LMA, but these require the computation of the Jacobian to estimate the Hessian matrix, so these are more computationally intensive. A pseudocode for the algorithm is available in the appendix (section ??).

Newton-Gauss

The Newton-Gauss method is an algorithm that finds the local minimum of a function by approximating the Hessian matrix with the Jacobian and its transpose (eq. ??). By estimating the Hessian, the algorithm only requires the computation of the first order derivatives with respect to each parameter, at each point pair x , y . It is possible to use the function and the analytical derivative, but as this work requires the calculation of functions that have no simple analytical form, the first derivative will be approximated within the algorithm.

$$\begin{aligned}\vec{J}^T \vec{J} \vec{p} &= \vec{J}^T \vec{r} \\ \vec{r} &= \vec{y} - f(\vec{x}, \vec{p})\end{aligned}\tag{5.165}$$

Close to a minima, the NG method quickly moves to the optimum point. Depending on the starting point, it may converge only to a local minimum, and not the global, and it may also be unstable, not converging at all.

Levenberg Marquardt

The LMA is a NG type algorithm that includes the addition of a dampening term that helps to increase the robustness of the algorithm. The particular algorithm here uses a number of other schemes to improve the

overall effectiveness of the algorithm. The equation at the center of the algorithm is similar to that of NG (eq. ??).

$$\begin{aligned} \left(\vec{J}^T \vec{W} \vec{J} + \lambda \text{diag}(\vec{J}^T \vec{W} \vec{J}) \right) \vec{p} &= \left(\vec{J}^T \vec{W} \vec{r} \right) \\ \vec{r} &= \vec{y} - f(\vec{x}, \vec{p}) \end{aligned} \quad (5.166)$$

The starting value for lambda is calculated as a function of the estimate of the Hessian and a cutoff for lambda is introduced to remove dampening altogether. A delayed gratification scheme has also been introduced to increase lambda by 50 percent if the trial solution is worse, and to decrease lambda by a factor of 5 if the trial solution is better. Finally, a diagonal weighting matrix has been included to allow certain parameters to be preferential during their optimisation.

Chapter 6

Methodology: Proton Activation and Radioactive Decay

A computer program was developed to calculate the radioactivity of an ion irradiated target. The choice of projectile was limited to protons, but there is the option to increase this to other light ions. The decay equations were derived to be able to calculate the activity of isotopes within the target at time t. The simulation is split into two sections: the first with the beam on, where there will be source terms for isotopes, and the second with the beam off and no source terms.

SRIM, an ion transport code, was used to calculate ion trajectory data. Iron was irradiated experimentally by 36MeV protons with the University of Birmingham cyclotron, and its activity was measured and calculated using the activity code. Two versions of the code were created.

The equations and code were then used to predict the activity of an iron sample irradiated to 100DPA for a range of proton energies. This is a reasonable damage dose that is expected in Gen IV reactors.

6.1 Introduction

High flux neutron reactors are expensive to use, whereas proton accelerators capable of producing beams of adequate fluence and energy are more readily available, cheaper to buy and cheaper to run. Ion beams, due to the Coulomb interaction, are more controllable in terms of energy, direction and fluence. They may be concentrated on a desired target at a set fluence and energy.

Depending on the energy of the ion beam, the target material will become radioactive. The stable nuclei are transmuted and when the resulting isotope is unstable it will decay. An equation was derived to predict the activity of isotopes for any decay chain with source terms and branching factors included. Two versions of a computer code were developed to compute the reaction rates and activity of the irradiated targets.

6.2 Activation by Ion Irradiation

The Bateman equation was derived using Laplace transforms, and this same method has been used to develop a modified equation that incorporates branching factors and production rates for each isotope in the decay chain, as illustrated by fig. ??.

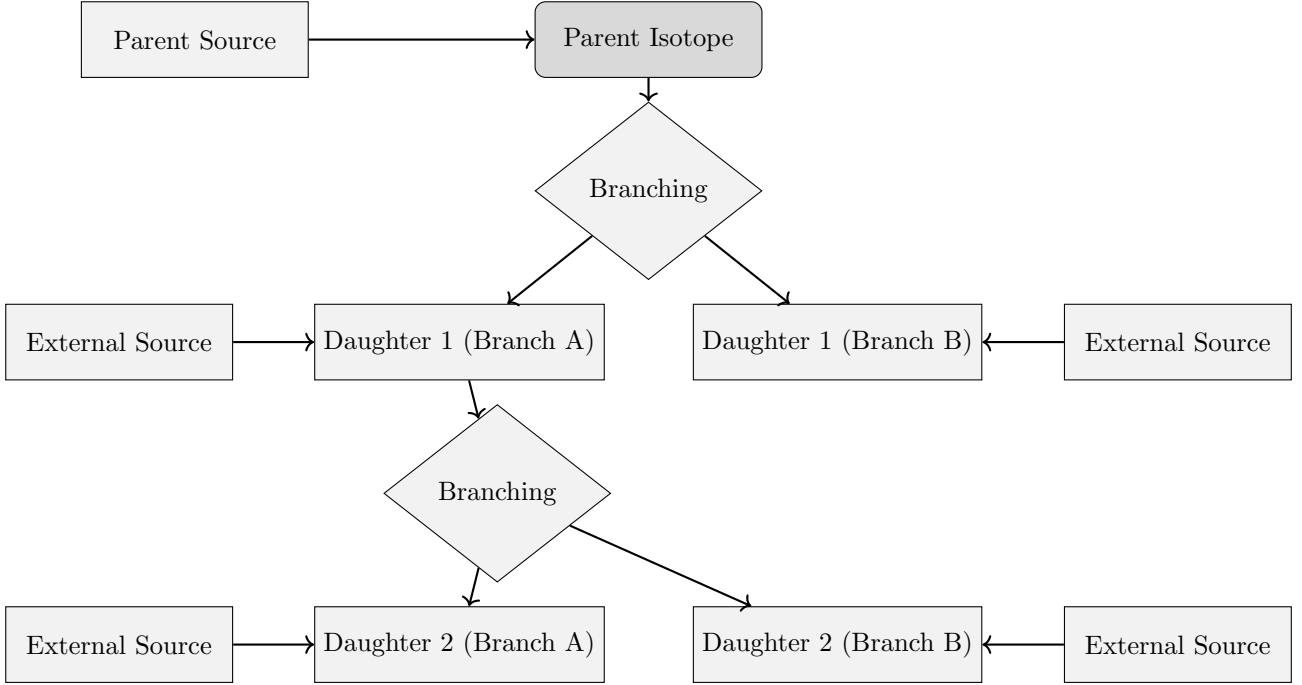


Figure 6.1: An example of several decay chains including branching factors and possible external source terms for each isotope on each chain.

6.2.1 Laplace Transform

Laplace Transforms (eq. ??) are a useful mathematical tool, and allow ordinary differential equations to be solved by simple algebraic manipulation in the s domain. Bateman took advantage of Laplace Transforms in deriving his equation, and this is the method that has been taken here as well.

$$F(s) = \int_0^{\infty} f(t) \exp(-st) dt \quad (6.1)$$

6.2.2 Constructing the Differential Equations

The first step is to set up differential equations for the parent isotope, unstable daughter isotopes and stable daughter isotope. The parent isotope has a source term, due to production, and a loss term, due to decay. The unstable daughter isotopes have two source terms, from the production by irradiation induced transmutation and the decay of preceding isotopes in the decay chain, and a loss term, due to decay. Finally, the stable daughter that finalizes the decay chain has two source terms (the same as the unstable daughters) but no loss term.

The variables (and vectors) used in these equations are defined as follows:

- $\vec{\lambda}$ vector containing isotope decay constants λ_i
- \vec{b} vector containing isotope to isotope branching factors b_i
- \vec{w} vector containing isotope production rates w_i
- t time at which activity/amount of isotope is measured
- $N_i(0)$ starting amount of the i^{th} isotope
- $N_i(t)$ amount of the i^{th} isotope at time t

- $N'_i(t)$ change in amount of the i^{th} isotope, with respect to time, at time t

The differential equations for the parent isotope (first isotope), unstable daughter isotopes (i^{th} isotopes) and stable, final, daughter isotope (z^{th} isotope) in the time domain are as follows:

$$N'_1(t) = \omega_1 - \lambda_1 N_1(t) \quad (6.2)$$

$$N'_i(t) = \omega_i + b_{i-1} \lambda_{i-1} N_{i-1}(t) - \lambda_i N_i(t) \quad (6.3)$$

$$N'_z(t) = \omega_z + b_{z-1} \lambda_{z-1} N_{z-1}(t) \quad (6.4)$$

Applying the Laplace Transform to these three differential equations allows them to be manipulated and solved algebraically in the s-domain.

$$N_1(s) = \frac{1}{s + \lambda_1} N_1(0) + \frac{1}{s(s + \lambda_1)} \omega_1 \quad (6.5)$$

$$N_i(s) = \frac{1}{s(s + \lambda_i)} (\omega_i) + \frac{1}{s + \lambda_i} (b_{i-1} \lambda_{i-1} N_{i-1}(s)) + \frac{1}{s + \lambda_i} N_i(0) \quad (6.6)$$

$$N_z(s) = \frac{1}{s^2} \omega_z + \frac{1}{s} b_{z-1} \lambda_{z-1} N_{z-1}(s) + \frac{1}{s} N_z(0) \quad (6.7)$$

6.2.3 Numerical Inversion of the Laplace Transform

The Gaver-Stehfest[[stehfest](#)] algorithm was developed in the 1960s and 1970s and is a method of calculating the inverse of a Laplace Transform in the real number domain. It is an easy to implement and reasonably accurate method, although it is an approximation to the real value. A comparison between an analytic and numeric inversion for the unstable isotope Po-218 is discussed at the end of this section (figure ??).

$$f(t) \approx f_n(t) = \frac{\ln(2)}{t} \sum_{k=1}^{2n} a_k(n) F(s) \text{ where } n \geq 1, t > 0 \quad (6.8)$$

$$s = \frac{k \ln(2)}{t} \quad (6.9)$$

$$a_k(n) = \frac{(-1)^{(n+k)}}{n!} \sum_{j=\text{Floor}(\frac{k+1}{2})} j^{n+1} \binom{n}{j} \binom{2j}{j} \binom{j}{k-j} \quad (6.10)$$

The equation for the i^{th} isotope may be calculated by recursively calculating the equations by numeric inversion, starting from the first (parent isotope) and inserting the result into each subsequent recursion until the i^{th} isotope is reached (changing the equations appropriately for the parent, unstable daughter and stable daughter isotopes).

6.2.4 Analytic Solution by Partial Fraction Expansion

The equation for the i^{th} isotope in the s domain can be written in full by substituting the preceding equation until the parent isotope is reached, and this full equation may be rearranged with the production amount of

each isotope and starting amount of each isotope in individual terms. Each of these terms is multiplied by a fraction that can be expanded, using partial fractions, and inverted analytically.

This is illustrated with an example unstable isotope, fourth in the decay chain (including the parent isotope) (eq. ??).

$$\begin{aligned}
N_4(s) = & \frac{1}{(s + \lambda_1)(s + \lambda_2)(s + \lambda_3)(s + \lambda_4)} b_2 b_3 b_4 \lambda_1 \lambda_2 \lambda_3 N_1(0) \\
& + \frac{1}{(s + \lambda_2)(s + \lambda_3)(s + \lambda_4)} b_3 b_4 \lambda_2 \lambda_3 N_2(0) \\
& + \frac{1}{(s + \lambda_3)(s + \lambda_4)} b_4 \lambda_3 N_3(0) \\
& + \frac{1}{(s + \lambda_4)} N_4(0) \\
& + \frac{1}{s(s + \lambda_1)(s + \lambda_2)(s + \lambda_3)(s + \lambda_4)} b_2 b_3 b_4 \lambda_1 \lambda_2 \lambda_3 \omega_1 \\
& + \frac{1}{s(s + \lambda_2)(s + \lambda_3)(s + \lambda_4)} b_3 b_4 \lambda_2 \lambda_3 \omega_2 \\
& + \frac{1}{s(s + \lambda_3)(s + \lambda_4)} b_4 \lambda_3 \omega_3 \\
& + \frac{1}{s(s + \lambda_4)} \omega_4
\end{aligned} \tag{6.11}$$

An example stable isotope, fourth (last) in the decay chain (including the parent isotope) (eq. ??).

$$\begin{aligned}
N_4(s) = & \frac{1}{s(s + \lambda_1)(s + \lambda_2)(s + \lambda_3)} b_2 b_3 b_4 \lambda_1 \lambda_2 \lambda_3 N_1(0) \\
& + \frac{1}{s(s + \lambda_2)(s + \lambda_3)} b_3 b_4 \lambda_2 \lambda_3 N_2(0) \\
& + \frac{1}{s(s + \lambda_3)} b_4 \lambda_3 N_3(0) \\
& + N_4(0) \\
& + \frac{1}{s^2(s + \lambda_1)(s + \lambda_2)(s + \lambda_3)} b_2 b_3 b_4 \lambda_1 \lambda_2 \lambda_3 \omega_1 \\
& + \frac{1}{s^2(s + \lambda_2)(s + \lambda_3)} b_3 b_4 \lambda_2 \lambda_3 \omega_2 \\
& + \frac{1}{s^2(s + \lambda_3)} b_4 \lambda_3 \omega_3 \\
& + \frac{1}{s^2} \omega_4
\end{aligned} \tag{6.12}$$

By using partial fraction expansion and standard Laplace Transforms, the set of equations (eqs. ??, ??, ??, ??) is used to calculate the amount of the m^{th} isotope in the decay chain, providing the m^{th} isotope is unstable.

$$N_m(t; \vec{\lambda}, \vec{b}, \vec{w}) = \sum_{k=1,m} r(k; \vec{\lambda}, \vec{b}) [f(t; k, m, \vec{\lambda}) N_k(0) + g(t; k, m, \vec{\lambda}) w_k] \tag{6.13}$$

$$r(k, m, \vec{\lambda}) = \begin{cases} \prod_{i=k, m-1} (b_{i+1} \lambda_i), & \text{if } k < m \\ 1, & \text{if } k = m \end{cases} \tag{6.14}$$

$$f(t; k, m, \vec{\lambda}) = (-1)^{m-k} \sum_{i=k,m} \left[\exp(-\lambda_i t) \prod_{j=k,m;j \neq i} \left(\frac{1}{\lambda_i - \lambda_j} \right) \right] \quad (6.15)$$

$$g(t; k, m, \vec{\lambda}) = \frac{1}{\prod_{i=k,m} \lambda_i} + (-1)^{m-k+1} \sum_{i=k,m} \left[\frac{1}{\lambda_i} \exp(-\lambda_i t) \prod_{j=k,m;j \neq i} \left(\frac{1}{\lambda_i - \lambda_j} \right) \right] \quad (6.16)$$

The set of equations (eqs. ??, ??, ??, ??) is used to calculate the amount of the m^{th} isotope in the decay chain, where the m^{th} isotope is stable.

$$N_m(t; \vec{\lambda}, \vec{b}, \vec{w}) = N_m + w_m t + \sum_{k=1,m-1} r(k; \vec{\lambda}, \vec{b}) \left[f(t; k, m-1, \vec{\lambda}) N_k(0) + g(t; k, m, \vec{\lambda}) w_k \right] \quad (6.17)$$

$$r(k, m, \vec{\lambda}) = \begin{cases} \prod_{i=k,m-1} (b_{i+1} \lambda_i), & \text{if } k < m \\ 1, & \text{if } k = m \end{cases} \quad (6.18)$$

$$f(t; k, m, \vec{\lambda}) = \frac{1}{\prod_{i=k,m} \lambda_i} + (-1)^{m-k+1} \sum_{i=k,m} \left[\frac{1}{\lambda_i} \exp(-\lambda_i t) \prod_{j=k,m;j \neq i} \left(\frac{1}{\lambda_i - \lambda_j} \right) \right] \quad (6.19)$$

$$g(t; k, m, \vec{\lambda}) = \frac{1}{\prod_{i=k,m} \lambda_i} t - \frac{\sum_{i=k,m} \left[\prod_{j=k,m;j \neq i} \lambda_j \right]}{\prod_{i=k,m} \lambda_i^2} + (-1)^{m-k} \sum_{i=k,m} \left[\frac{\exp(-\lambda_i t)}{\prod_{j=k,m;j \neq i} (\lambda_i - \lambda_j)} \right] \quad (6.20)$$

6.2.5 Preference: Analytic over Numeric

The numeric solution only requires the equation to be solved in the s-domain; the Gaver-Stehfest algorithm performs the inversion. It is worth the extra effort to derive and implement an analytic solution, as the numeric is only an approximation. Examples of the pitfalls of the numeric solution are that it can give negative amounts of an isotope and the difference between the numeric and analytic calculated amounts can become quite large when the isotope decays away to a very small value. Fig. ?? shows the predicted decay of a sample of Po-218 irradiated for 1,000s, and sampled until 10,000s. In the region between 4,000s and 9,000s the amount from the numeric calculation drops below zero, whereas the analytic calculation remains above zero, as would be expected.

6.3 Computational Methods

6.3.1 Activity V1

The Activity V1 program has been developed in Fortran and takes advantage of MPI (Message Parsing Interface) to speed up calculation times by allowing the use of multiple processes in parallel. It has a self contained maths

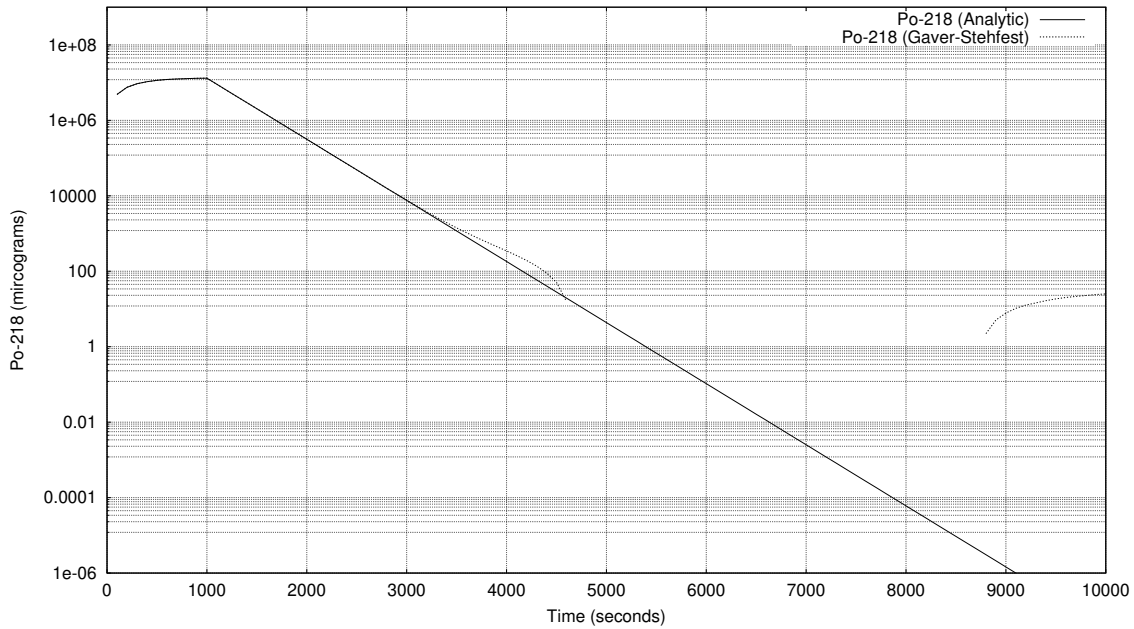


Figure 6.2: Decay of Po-218: Analytic and Gaver-Stehfest Calculations [jeff311]

library, although this could be improved in the future by using optimised maths libraries for certain functions (e.g. linear algebra).

The code was developed on a Debian based distribution of Linux, but it should be supported on other variants of Linux and Unix, and does not require any specialist hardware.

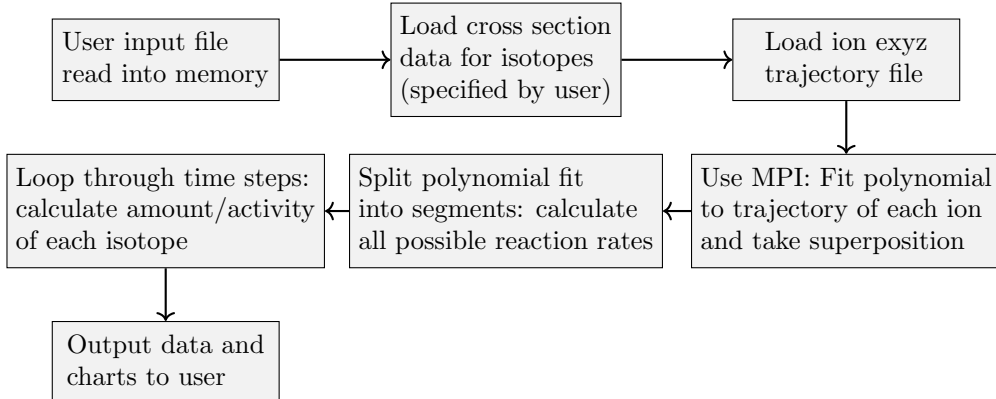


Figure 6.3: Flow chart of major processes in the Activity code

The user is required to prepare an input file that contains the instructions required to perform a calculation. In addition to the input file, the user must provide an EXYZ ion trajectory file output by SRIM. Activity will read in the user input file, and the SRIM and data files listed within, before performing the calculation. Fig. ?? shows a flowchart of the major steps the code performs.

There are various settings in the user input file, but the main ones relating to the simulated experiment are:

- Element composition of target (percentage by mass).
- Beam flux (current), energy, duration and area on target.
- Activity measurement time (end of the “experiment”).
- Material density.

- Target thickness.

A brief manual that accompanies the program is in the appendix section ?? and the published paper that accompanies the code is in section ??.

6.4 Ion Trajectory Data

The SRIM code is used to generate ion trajectory data. This uses a quantum mechanical treatment of ion-atom collisions and statistical algorithms to speed up the process[[srimwebsite](#)].

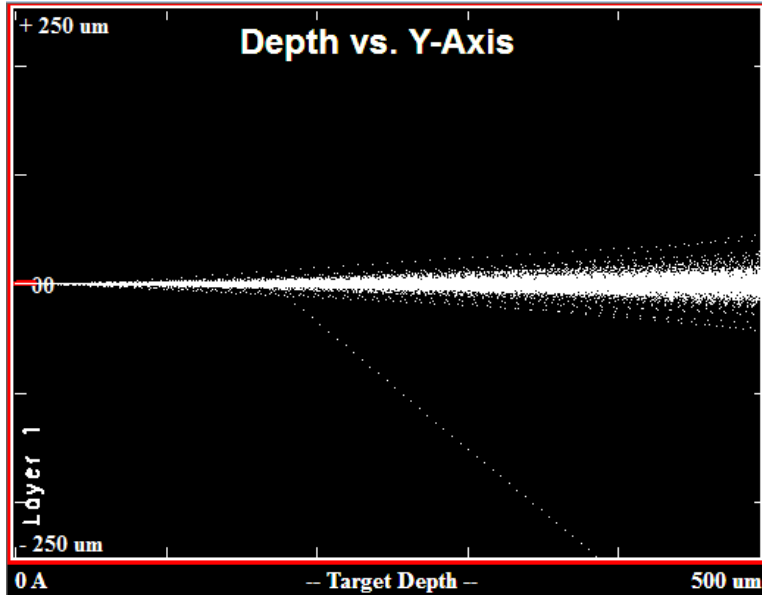


Figure 6.4: 36MeV Ion Track

The trajectory data files used by both versions of the Activity code will be created using SRIM for the required beam energy and target combinations.

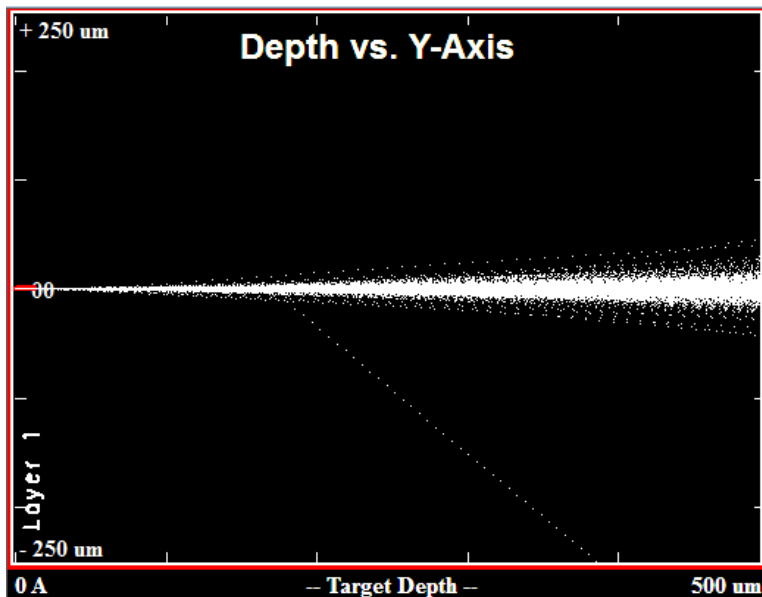


Figure 6.5: 36MeV Ion Track

The target is set as pure Iron, and due to the way SRIM functions, the structure type is inconsequential. At just 0.5mm in thickness, the 36MeV ions pass through the targets and exit with an energy above 30MeV, and the exyz.txt data file covers this range of ion energies.

6.4.1 Activity V2

A second program was developed to use Python rather than Fortran. One problem that motivated this was occasionally a particular isotope would cause the code to crash, and a second issue was the complication of compiling the code for new users. The Python version runs with relatively few interventions by the user and it handles errors in the data (or lack of) more gracefully. The procedure it follows is similar to the Activity V1 code and the manual is included in appendix section ??.

6.5 Activation by Neutron Irradiation

A short program was created to estimate neutron activity based on the existing code developed to calculate ion activation. It is a simple non-transport neutron activation code, used to estimate the activity and subsequent cooling of materials irradiated by neutrons. A single energy neutron flux or Maxwell-Boltzmann distribution may be selected by the user and the TENDL-2019 data file is used to provide cross sections for calculating reaction rates. Finally, the previously derived extended Bateman equations are used to calculate isotopes at time t after irradiation begins.

6.6 Cyclotron Irradiated Iron

6.6.1 Cyclotron Beam Line

The Scanditronix MC40 cyclotron at the University of Birmingham has several beamlines and is capable of accelerating protons, deuterons, Helium 3 and Helium 4 with fluxes and energy ranges detailed in table ???. After running a simulation with SRIM, the 36MeV protons were expected to create an average of 15.8 vacancies each.

Particle	Energy (MeV)	Max Current (micro A)	Flux (ions per second)
p	8-40	60	3.75×10^{14}
d	8-40	30	1.87×10^{14}
$^4He^{2+}$	8-53	30	9.36×10^{13}
$^3He^{2+}$	4-20	60	1.87×10^{14}

Table 6.1: Beam Characteristics of the Scanditronix MC-40

The cyclotron is located in one room, and several beam lines run from the cyclotron to other rooms in the cyclotron building. The operation room is separate from the cyclotron and beam line rooms (fig. ??).

The iron sample was held perpendicular to the beam line, with the ions passing through the 0.5mm thickness of the sheet. The beam area was approximately $6.4 \times 10^{-5} m^2$, irradiating a volume of approximately $3.2 \times 10^{-8} m^3$. The target was irradiated for 300 seconds at 0.5 micro amps and it was expected to cause over 1.4×10^{16} displacements within the volume of iron targetted by the beam. With a number density of approximately 8×10^{28} atoms per cubic meter, giving a relatively low damage dose, when compared to that expected over the lifetime of a component within the reactor, of 5^{-6} DPA.

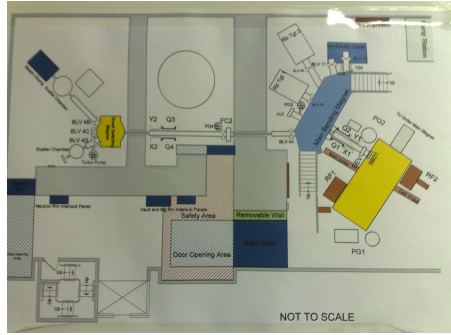


Figure 6.6: Cyclotron layout - main hall and beam lines



Figure 6.7: Gamma warning alarm during 0.5 microamp 36MeV proton irradiation of iron

During irradiation, the amount of Gamma radiation released was enough to trip the alarm for the room (fig. ??). The proton fluence was less than 1% of the maximum fluence capable of being produced by the cyclotron, so this was definitely a concern. To increase the damage dose, and keep to a shorter period of time, the current would most probably be increased to a much higher percentage, also increasing the rate of Gammas produced during irradiation.

6.6.2 Measurement of Sample Activity

The sample was too radioactive to safely handle immediately after irradiation, so it was left to cool for several days before taking measurements. After it had cooled, a high purity germanium detector (fig. ??) was used to measure the activity of the irradiated sample.

The detector and preamplifier are both cooled by liquid nitrogen to 77K, as the band-gap of germanium is 0.7eV and the thermal motion of electrons and nuclei at higher temperatures would induce currents causing noise and interference in the detector. As a gamma ray enters the detector it creates an electron-hole pair in the medium of the detector. The holes and electrons are attracted to the center and to the outer cylinder of the detector, or vice versa.

6.6.3 Prediction of Activity

Following the measurement of the foil target, in the first instance the predicted activity will be estimated using the average ion energy, the cross section of this energy and the two reactions that result in Co-55 ($^{54}_{26}Fe(p,\gamma)^{55}_{27}Co$ and $^{56}_{26}Fe(p,2n)^{55}_{27}Co$). The activity code (version 1 and version 2) are then used to predict the activity of the sample as well as the expected gamma spectra.



Figure 6.8: High Purity Germanium Detector

Chapter 7

Results: Activity Code

The aim of the first part of this work was to derive an equation capable of calculating the radioactivity of an isotope and all the subsequent isotopes in the decay chain, taking into account branching factors and source terms. This was achieved and a computer code was developed in Fortran to predict the radioactivity of a target irradiated by an ion beam.

The equation has been written into several Python 3 functions and a second code was developed to estimate the radioactivity of a thin foil irradiated by neutrons passing through perpendicular to the plane of the foil.

7.1 Extended Bateman Equations

The Bateman equations were derived from scratch to include a source term for each isotope and branching factors from parent isotope to daughter isotope(s). This process along with the numerical and analytic solutions are outlined in section ??.

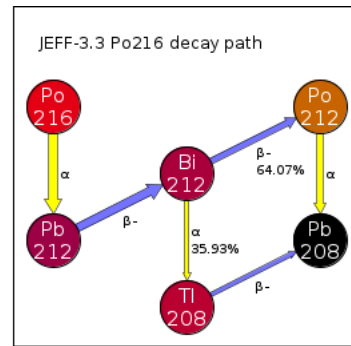


Figure 7.1: Decay path of Polonium-216

The decay equations were programmed as class in python (section section:decayclass) that used decay data accessible through a second class, isotopes, that loaded data from the JEFF 3.1.1 data file. The static function for computing activity in this class was tested against numerically computed values.

Due to the large range in magnitude of the half life for various isotopes, a decay chain was selected where the time step for the numeric calculation would be applicable to the half life of the isotopes in the decay chain, whilst keeping the number of steps low enough to compute the activities in a reasonable amount of time with a simple algorithm.

Isotope	Half Life (s)
Po-216	1.45×10^{-1}
Pb-212	3.83×10^4
Bi-212	3.63×10^3
Po-212	2.99×10^{-7}
Tl-212	3.1×10^1
Pb-208	Stable

Table 7.1: Half life of isotopes in the Po-216 decay chain

The range of half life in the Polonium decay chain was from 3.83×10^4 s for Pb-212 down to 2.99×10^{-7} s for Po-212 and the maximum number of steps used in the numeric calculation is 10^{10} .

Isotope	Source Rate	N_0
Po-216	2.0×10^{-1}	1.0×10^2
Pb-212	0.0×10^0	5.0×10^0
Bi-212	7.0×10^{-2}	1.5×10^1
Po-212	5.0×10^{-3}	0.0×10^0
Tl-212	0.0×10^0	0.0×10^0
Pb-208	1.0×10^{-2}	3.0×10^2

Table 7.2: Parameters used for the decay equation vs numeric calculation comparison

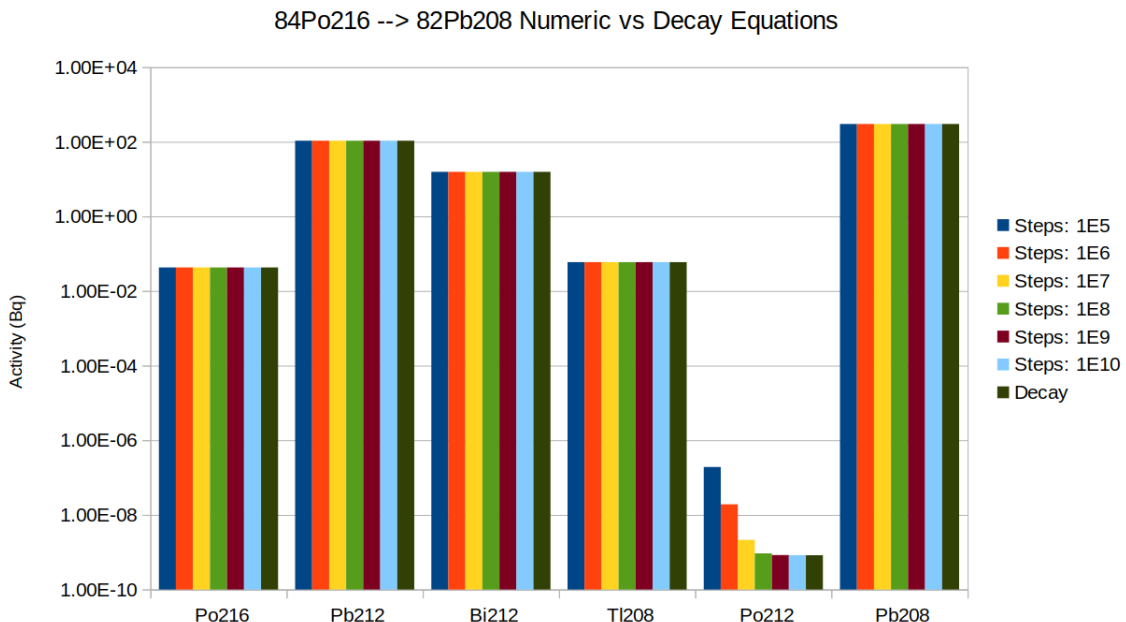


Figure 7.2: Decay path of Polonium-216

The numeric code is detailed in the appendix (section ??). For all but the short half life isotope Po-212, the numeric calculations are in good agreement with the decay equations. As the number of steps increases, and hence the time step decreases, the numerically computed activity for Po-212 also converges to that calculated with the decay equations.

7.2 Activity V1 Computer Package

A large proportion of the results for this part of the work was the development of a computer program to implement the decay equations and calculate reaction rates of isotopes, protons and production rates of resultant isotopes.

The source code and instructions on how to use the program are available to download from GitHub.

Program	Repository
Activity	https://github.com/BenPalmer1983/activity

Table 7.3: Activity V1 Code on GitHub

Activity V1 uses the TENDL-2009 cross section database, as well as several other data files that contain element, isotope and decay data. The user provides an ion trajectory file and an input file that specifies beam parameters and target composition.

7.3 Activity V2 Computer Package

There were a number of issues with version 1 of the computer code. It was written in Fortran, but over time this has been a stumbling block for new users, especially those new to Linux and unfamiliar with Fortran.

In the first version of the code, the trajectory data was replaced with a series of polynomials, but this method was not a reliable solution and it was preferred to use the data directly to calculate the reaction rates. Finally, a language such as Python3 is more widely used and contains very useful features such as dictionaries and a plotting module (matplotlib).

The source code and instructions on how to use the program are available to download from GitHub.

Program	Repository
Activity	https://github.com/BenPalmer1983/activity_v2

Table 7.4: Activity V2 Code on GitHub

Activity V2 uses the TENDL-2019 cross section database for cross section reaction data and the JEFF3.1.1 datafile for decay data. As with version 1, the user provides an ion trajectory file and an input file that specifies beam parameters and target composition.

7.4 Neutron Activation

A small side-project was the development of a simple neutron activation code that uses the TENDL-2019 neutron cross section data file to estimate the activity of a neutron irradiated target. The reason for this was to be able to estimate the activity of components irradiated in a high flux neutron reactor and compare these to the radioactivity of proton irradiated components.

The source code and instructions on how to use the program are available to download from GitHub.

Program	Repository
Neutron Activation	https://github.com/BenPalmer1983/neutron_activation

Table 7.5: Neutron Activation Code on GitHub

7.5 Proton Irradiated Iron

In this work, Iron has been irradiated with a proton beam. Using the TENDL cross section libraries, the Co-55 activity has been estimated and this, along with other expected gammas, have been predicted using the Activity code.

7.5.1 Cobalt-55

Co-55 is a relatively short lived isotope, with a half life of 17.5 hours, that is a concern to health during and shortly after irradiation. Co-55 decays into another radioactive isotope, Fe-55, which then decays into Mn-55 (fig. ??). The second step in the decay chain is 2.73 years, so the first step with a much shorter half life will be responsible for the majority of the radiation shortly after being irradiated by protons.

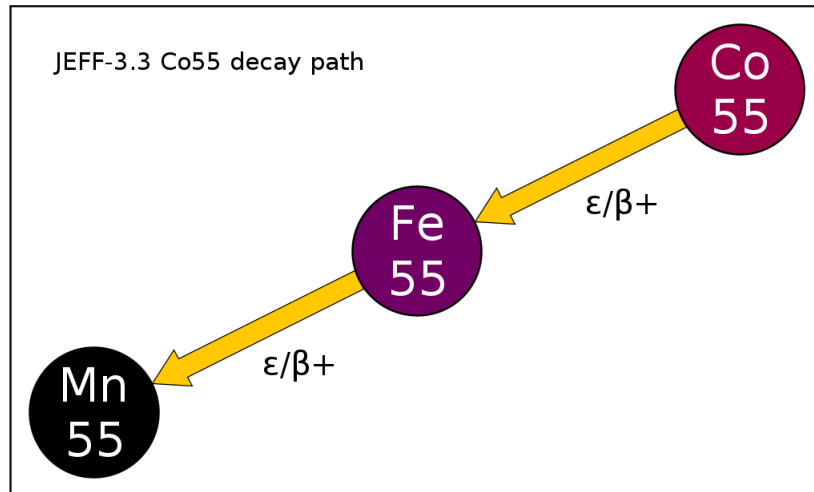


Figure 7.3: Decay path of Cobalt-55

The decay of Co-55 will produce a range of gammas (fig. ??), but one in particular to focus on when measuring the radioactivity is the 931KeV gamma with an intensity of 75%.

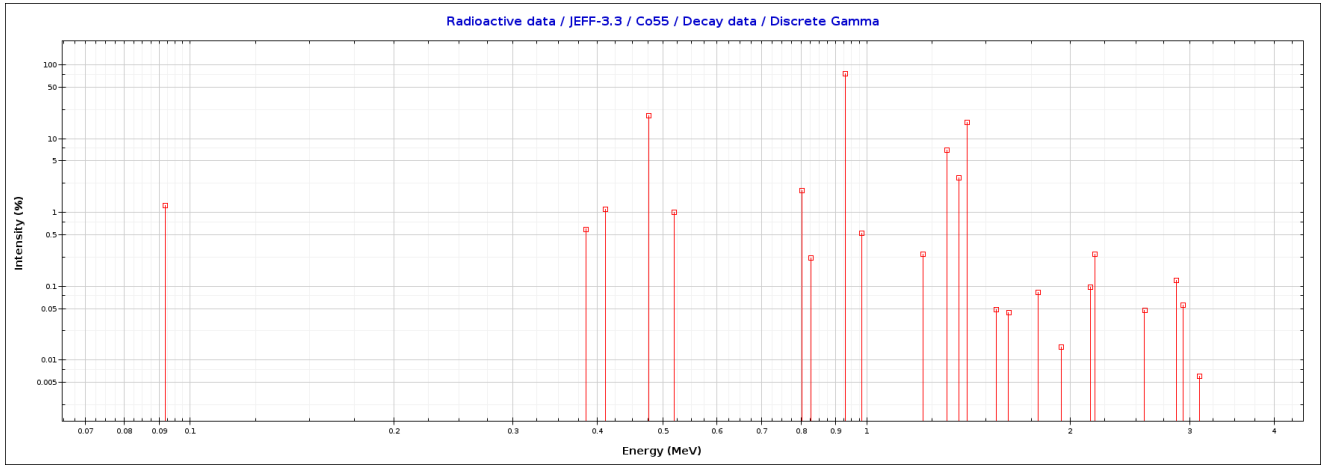


Figure 7.4: Cobalt-55 Gamma Intensity Plot

The stable isotope Iron-54 makes up almost 6% of natural iron, and one reaction possibility with a proton results in Co-55 and a gamma, $^{54}_{26}Fe(p, \gamma)^{55}_{27}Co$. The most abundant isotope in natural Iron also has a route to transmute to Co-55 through the capture of a proton and the loss of two neutrons, $^{56}_{26}Fe(p, 2n)^{55}_{27}Co$.

Due to the short half-life and intensity of the 931KeV gamma, this peak was measured in particular after irradiating the iron target. It was also estimated manually using the TENDL-2009 and TENDL-2019 cross section databases.

7.6 Cyclotron Beam Line - Proton Irradiated Iron

A 0.5mm thick pure iron target was irradiated for five minutes at a current of 0.5 microamps with 36MeV protons. The proton beam formed a $64mm^2$ square that was taken from the cyclotron through one of the beam lines, with the target perpendicular to the beam.

The target was left to cool for several days before being safe enough to handle. The radioactivity was measured using a high purity germanium detector which was calibrated to detect approximately 4 out of every 100 gammas emitted.

-
- 1 RANGE: 617 = 911.51keV to 649 = 958.79keV
 - 2 AREA : Gross = 2127168 Net = 1342565 +/- 2207
 - 3 CENTROID: 631.74 = 933.29keV
 - 4 SHAPE: FWHM = 6.82 FW(1/5)M = 10.06
 - 5 ID: Bi-214 at 934.05keV
 - 6 Corrected Rate = 35349.26 +/- 58.11 cA
-

Listing 7.1: Maestro 931KeV Peak Measurement

The gamma counts were recorded over a range of 0MeV to 3MeV (fig. ??). Correcting the measured count for the 931KeV peak, to account for the geometry and detector, the count rate for 931KeV gamma rays from Co-55 was measured at $4.43 \times 10^4 + / - 1.05 \times 10^3$ counts per second.

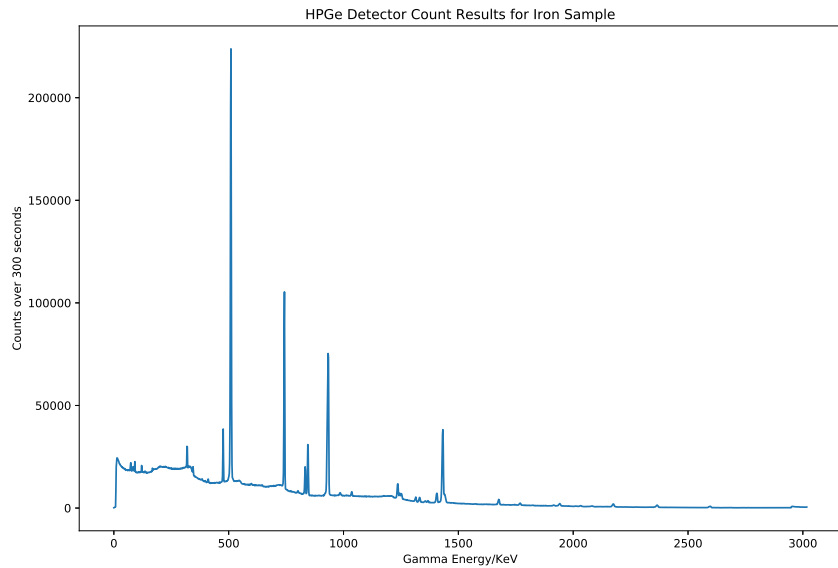


Figure 7.5: Gamma counts from the irradiated iron target over 300 seconds

7.7 SRIM Proton Irradiated Iron

The trajectory data used by the activity code(s), and also to estimate the Co-55 activity, was provided by SRIM. An input configuration was set with Iron as the target material and protons as the projectile ion. The sample depth was set to at least the target thickness, 0.5mm. The activity code truncates the data to fit the target thickness, so a much larger depth, say 1m, could be set in SRIM to ensure all the ions stop within the simulated target, and this data file may be reused for targets of varying thicknesses.

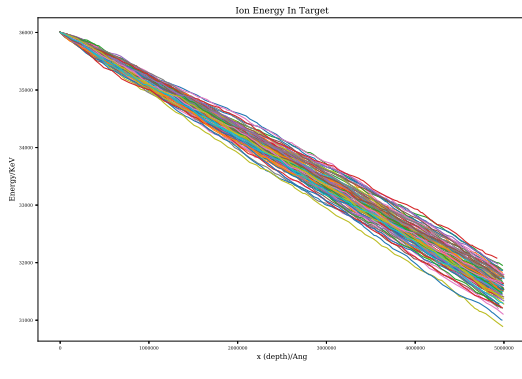


Figure 7.6: Energy vs target depth - protons through a 0.5mm thick iron target

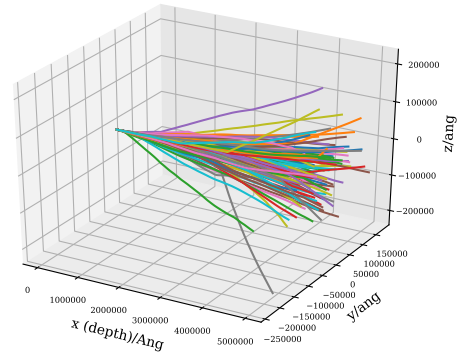


Figure 7.7: Ion trajectory - 0.5mm thick iron target

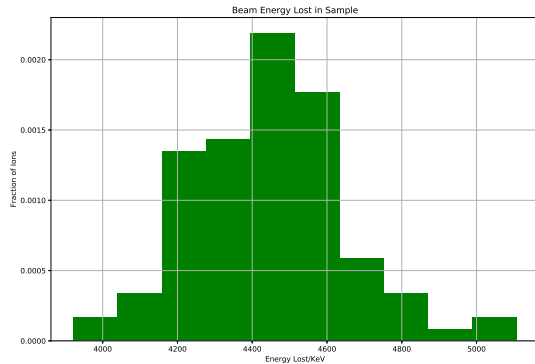


Figure 7.8: Ion energy lost in 0.5mm thick target

The ions travelling through the thin 0.5mm target lose between 4MeV and 5MeV (fig. ??) as they pass, and they do so quite smoothly (fig. ??). The majority of the energy is lost smoothly through electronic stopping. As the thickness of the iron is increased, all the energy is lost to the iron target, and occurs within a shorter range in the remaining quarter of a millimetre depth of the iron target (fig. ??).

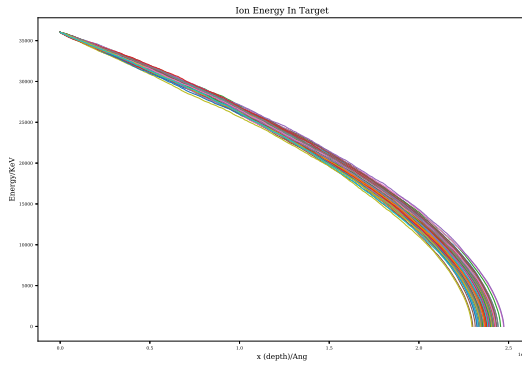


Figure 7.9: Energy vs target depth - protons in iron target (1m thick)

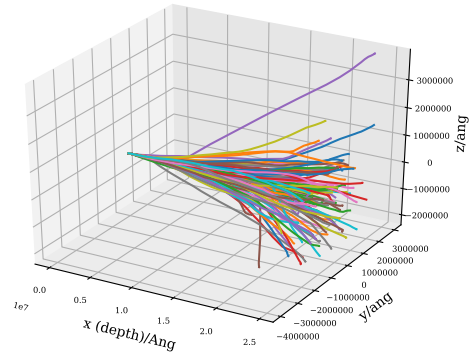


Figure 7.10: Ion trajectory - iron target (1m thick)

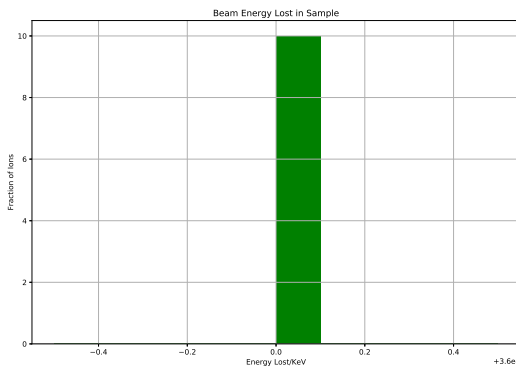


Figure 7.11: Ion energy lost in target (1m thick)

7.8 Estimate of Activity Using TENDL Data

There are over ten TENDL libraries available, and the available data and the range of data points is inconsistent across the different versions. The earlier 2009 library, that was used in the first version of the Activity code, covers a range up to 200MeV for Iron cross sections but the more recent 2019 version, that was used in the second version of the activity code, only covers up to 30MeV for Iron.

The 2019 data file ranges up to 30MeV for the $^{54}_{26}Fe(p, \gamma)^{55}_{27}Co$ and $^{56}_{26}Fe(p, 2n)^{55}_{27}Co$ reactions. As the data cuts off at 30MeV, the cross section data for a 28-30MeV proton is used in the estimation.

Parameter	$^{54}_{26}Fe(p, \gamma)^{55}_{27}Co$	$^{56}_{26}Fe(p, 2n)^{55}_{27}Co$
ND/atoms	4.6×10^{27}	7.4×10^{28}
J/amps	0.5×10^{-7}	0.5×10^{-7}
Q/C	1.60×10^{-19}	1.60×10^{-19}
d/m	5.0×10^{-4}	5.0×10^{-4}
sigma/barns	2.0×10^{-4}	2.0×10^{-2}
irradiation time/s	3.0×10^2	3.0×10^2
Co55 t-half/s	6.3×10^4	6.3×10^4
Co55 λ	1.1×10^{-5}	1.1×10^{-5}
931KeV Gamma Intensity	0.75	0.75
Reaction Rate/atoms per second	1.4×10^5	2.3×10^8
N(Co55 at 300s)	4.3×10^7	6.9×10^{10}
Activity(Co55 at 300s)	4.8×10^2	7.5×10^5
N(Co55 at 3 days)	2.5×10^6	4.0×10^9
Activity(Co55 at 3 days)	2.8×10^1	4.4×10^4
931KeV Gamma	2.1×10^1	3.3×10^4

Table 7.6: Estimation using 28-30MeV protons and the TENDL-2019 database

The 2009 data file ranges from a fraction of an eV to 200MeV for the $^{54}_{26}Fe(p, \gamma)^{55}_{27}Co$ and $^{56}_{26}Fe(p, 2n)^{55}_{27}Co$ reactions, and the average cross section is taken for each reaction based on a 36MeV proton that loses up to 5MeV travelling through the 0.5mm thick Iron target.

Parameter	$^{54}_{26}Fe(p, \gamma)^{55}_{27}Co$	$^{56}_{26}Fe(p, 2n)^{55}_{27}Co$
ND/atoms	4.6×10^{27}	7.4×10^{28}
J/amps	0.5×10^{-7}	0.5×10^{-7}
Q/C	1.60×10^{-19}	1.60×10^{-19}
d/m	5.0×10^{-4}	5.0×10^{-4}
sigma/barns	1.5×10^{-4}	3.0×10^{-2}
irradiation time/s	3.0×10^2	3.0×10^2
Co55 t-half/s	6.3×10^4	6.3×10^4
Co55 λ	1.1×10^{-5}	1.1×10^{-5}
931KeV Gamma Intensity	0.75	0.75
Reaction Rate/atoms per second	1.1×10^5	3.4×10^8
N(Co55 at 300s)	3.3×10^7	1.0×10^{11}
Activity(Co55 at 300s)	3.6×10^2	1.1×10^6
N(Co55 at 3 days)	1.9×10^6	6.0×10^9
Activity(Co55 at 3 days)	2.1×10^1	6.6×10^4
931KeV Gamma	1.6×10^1	4.9×10^4

Table 7.7: Estimation using 36MeV protons and the TENDL-2009 database

The largest contribution to the 931KeV gamma is due to the $^{56}_{26}Fe(p, 2n)^{55}_{27}Co$ reaction, and the overall activity is predicted to be 33,000Bq using 28-30MeV protons with the TENDL-2019 data file (table ??), and 49,000Bq using 36MeV protons with the the TENDL-2009 data file (table ??).

7.9 Activity V1 - Simulated Proton Irradiated Iron

The activity code with the derived activity equations was used to calculate the predicted radioactivity (fig. ??) and predicted gamma lines (fig. ??).

Listing 7.2: Activity V1 Results 36MeV Protons and Iron

1 Fe36MeV.in

2 User Input Sim Details:

```

3     Beam Duration/s:          0.3000000000D+03
4     Beam Current/uA:          0.5000000000D+00
5     Beam Energy/MeV:          0.3600000000D+02
6     Beam Area/mm2:          0.1000000000D+03
7     Target Thickness/Angstrom: 0.5000000000D+07
8     Target Density/kgm-3:      0.8000000000D+04
9     Activity Measurement Time/s: 0.2600000000D+06
10
11    Most Active Isotopes      1.0907
12    Symbol   Z     A     M     Activity/Bq
13    CO       27    55    0     0.5942036078E+05
14    MN       25    52    0     0.4510767081E+05
15    CR       24    51    0     0.1444370965E+05
16    FE       26    55    0     0.1280863433E+05
17    MN       25    54    0     0.9738993802E+04
18    Total Activity/Bq:      0.1514219906E+06      1.1291
19    Run time: 1.1292
20
21    Total Activity/Bq:      0.1514219906E+06
22    Total Gamma Power/eV/s: 0.2559334931E+12
23    Total Gamma Power/Watts: 0.4100506435E-07
24    Absorbed Dose*/Grays/s: 0.4078849177E-10
25    Absorbed Dose*/Grays/hr: 0.1468385704E-06
26    Fraction of annual dosage if exposed for 1 hr: 0.1468385634E-03
27
28    Absorbed dose, assumes all energy absorbed, 80kg human, 1m from point-target, 1m surface area exposed to
         irradiation.
29
30    Dose Limits:
31    employees 18+ 20 millisieverts/year
32    trainees 18+ 6 millisieverts/year
33    public and under 18s 1 millisieverts/year
34    public and under 18s millisieverts averaged per hour: 0.1140771128E-03
35    Dose averaged over area of skin not exceeding 1cm2
36    Source: http://www.hse.gov.uk/radiation/ionising/doses/

```

The summary of the calculation is given in listing ?? and the full output file and details of all isotopes and their activities are in Appendix ??.

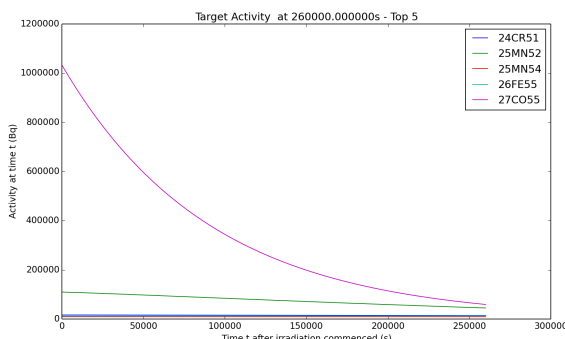


Figure 7.12: Isotopes with the top 5 radioactivity plotted over approximately 3 days

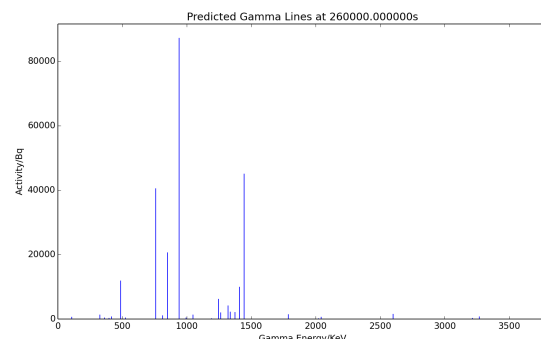


Figure 7.13: Predicted gamma lines approximately 3 days after irradiation

The code predicts a final 931KeV gamma activity of over 59,000 Bq and highlights several other isotopes of interest, including Mn-52, Cr-51, Fe-55 and Mn-54, all of which have an activity of approximately 10,000 Bq or above. After 3 days of cooling, the target is predicted to dose an 80KG human, 1 meter away from the target, with 4.0×10^{-11} Gy/s (absorbed dose) which is less than the limit for a member of the public (6.34×10^{-10} Si/s, effective dose).